論文 / 著書情報
Article / Book Information

題目(和文)	
Title(English)	Atmospheres of low-mass star planets: A tale of evolution
著者(和文)	KRISHNAMURTHYVigneshwaran
Author(English)	Vigneshwaran Krishnamurthy
出典(和文)	学位:博士(理学), 学位授与機関:東京工業大学, 報告番号:甲第12057号, 授与年月日:2021年9月24日, 学位の種別:課程博士, 審査員:佐藤 文衛,中本 泰史,井田 茂,奥住 聡,上野 雄一郎
Citation(English)	Degree:Doctor (Science), Conferring organization: Tokyo Institute of Technology, Report number:甲第12057号, Conferred date:2021/9/24, Degree Type:Course doctor, Examiner:,,,,
学位種別(和文)	博士論文
Type(English)	Doctoral Thesis

Atmospheres of low-mass star planets: A tale of evolution

A dissertation presented

by

Vigneshwaran Krishnamurthy

to

The Department of Earth and Planetary Sciences

in partial fulfillment of the requirements

for the degree of

Doctor of Philosophy

Tokyo Institute of Technology

Tokyo, Japan

June 2021

Advisors: Dr.Bun'ei Sato & Dr.Teruyuki Hirano Vigneshwaran Krishnamurthy

Atmospheres of low-mass star planets: A tale of evolution

Abstract

The origin of "*radius gap*" in close-in planets around lower-mass stars are not understood well. The paucity of planets between the radii 1.5 - 2 $R_\oplus$ in the radius-period diagram is termed as radius gap (Fulton et al. 2017). The primary candidate for explaining the origin of radius gap is the evaporation theory (Owen & Wu 2013, 2017), which predicts that the smaller planets are born with a core of 1 $R_\oplus$, surrounded by a 1% (by mass) voluminous envelope of H/He. In the first few hundred million years after forming, the high-energy radiation from the star induces the evaporation of this Hydrogen and Helium dominant atmosphere, thereby reducing the radius of the planet. That is the planet shifts from larger radius (higher peak around $2\,R_\oplus$ of the bimodal distribution; Fulton et al. 2017) to a lower radius (around $1\,R_\oplus$) due to photoevaporation. This prediction has been studied for smaller planets around solar-type stars (Fulton et al. 2017), however not for cooler K- and M-type stars. In this study, we present our observations of planets in and around the radius gap orbiting cooler K- and M-dwarfs. We find the lack of evaporative atmospheres in all our K- and M-dwarf targets (AU Mic b, GJ 9827b, GJ 9827d, TRAPPIST-1b, TRAPPIST-1e, TRAPPIST-1f and TOI-1235b) indicate that the evolution of smaller close-in planets around low-mass stars are different from those around solar-type stars. Our observational results cannot remove the gas-poor formation scenario in the low-mass star planets, accreting very less or no primordial atmosphere. We also present the detection of an evaporative atmosphere in a very young 17 Myr hot Jupiter,

HIP 67522b around a G-Dwarf. This detection is an important result for the atmospheric characterization as it is the farthest planet around a G-dwarf for which the evaporative atmosphere is characterized. We also detect atomic Vanadium evaporating from this hot Jupiter making it the first exoplanet to have atomic Vanadium detected. We detect an excess absorption of 7.1 $\pm$ 0.7% (altitude of 7.9644 R_p) in the He I region and an excess absorption of atomic Vanadium at 1.4 $\pm$ 0.8 % (altitude of 1.5705 R_p).

In this study, we also focus on the detectability of NIR molecular O_2 features from the lower atmospheres of TRAPPIST-1b, e and f planets. We do not detect any molecular O_2 features from TRAPPIST-1b and TRAPPIST-1e from our cross-correlation analysis of the observation from Subaru/IRD. However, in TRAPPIST-1f, we see a small feature of SNR $\sim$ 2 at -4 km/s in planet rest frame.

We also estimate the detectability of this feature from a future 30m class telescope with a spectrograph of resolution 100,000. We simulate the observations for a variety of atmospheres with different pressure levels. The simulations indicate that the desiccated O_2 atmospheres can be determined within 10 transits for TRAPPIST-1b, e and f. However, the Earth-like atmospheres can be detected only with 50-200 transits.

Our study provokes the question of the role of photoevaporation in low-mass stars' planets. Also our simulations provide the basic necessary information on planning the observations in a future 30m class telescopes.

Contents

Acknowledgments

I would like to thank Dr. Bun'ei Sato, Tokyo Institute of Technology, Japan and Dr. Teruyuki Hirano, NAOJ, Japan for their constant motivation and support throughout my PhD journey. From the time I landed in Japan, Dr. Sato has always been there to guide me, test my capabilities and make me learn in the process. Dr. Hirano has been the backbone of my work. His constant support and motivation helped me understand the intricacies of observation astronomy.

I would also like to thank Dr. Ravi Kopparapu, NASA GSFC, USA who introduced me to the HPF team: Dr. Suvrath Mahadevan, Penn State, USA; Dr. Gudmundur Stefansson, Penn State, USA and Dr. Joe Ninan, Penn State, USA which had come to fruition into an eventful collaboration. I would love to express my thanks to Dr. Eric Gaidos, University of Hawaii, USA for his constant support throughout the Subaru IRD observations. In collaborating with these gentlemen, I learned a lot.

I would like to thank the Subaru telescope's support astronomers, instrument PIs and staffs from the summit and in NAOJ, Mitaka for the continuous support throughout the observations. I would also like to thank Dr. Michael Gillon, University of Liege, Belgium for his support in getting the TTV data of TRAPPIST-1 planets. I would like to express my gratitude to all the members of Sato Laboratory in Tokyo Institute of Technology for their support. They made my life in Tokyo Tech easy.

I would like to express my utmost gratitude to my parents Mr. Krishnamurthy PR and Mrs. Sudha Krishnamurthy and my brother Mr. Prasanth Kowsik for their love and support throughout my PhD. I would also like to thank Ms. Disha for proof reading my thesis. Many thanks to Ms. Disha, Mr. Afraz Khan, Mr. Ramesh, Mr. Alam, Mr. Kireeti, Ms. Nivetha, Ms. Mitali, Mr. Shreesh, Mr. Amey, Mr. Ayushman, Mr. Harsha, Mrs. Sindhu, Mrs. Anubha and Mr. Aman for making my life in Japan more enjoyable and memorable. I would add my thanks to Ms. Suriya, Mr. Ram, Ms. Vertika, Ms. Nandita, Mr. Venkateswaran, Mr. Nishanth, Mr. Sajin, Mr. Bharath, Mr. Sreenesh, Ms. Nivetha, Mr. Ashwin, Ms. Lakshmi and Mr. Rajagopal for relieving my stress during the tough times.

Finally, I would like to express my thanks to the one and only Carl Sagan for motivating me to choose astronomy over engineering.

To them, who taught me to look inside and to Carl Sagan who taught me to look beyond!

Chapter 1

Introduction

"This space we declare to be infinite... In it are an infinity of worlds of the same kind as our own." - Giordano Bruno, 1584

1.1 The hunt for exoplanets

Ever since humans looked up towards the sky, the question of *'Are we alone?'* have pondered their mind. Great philosophers and mathematicians like Epicurus in third century BCE, Giordano Bruno in sixteenth century and Isaac Newton in eighteenth century have speculated the presence of planets around other stars with descriptive details on how the life on such planets could exist. These thoughts, however modern sounding, remained speculative.

The scientific search for exoplanets began with astrometry in the mid-nineteenth century, when a dark companion was suspected to orbit the binary star system 70 Ophiuchi observed from the Madras Observatory (Jacob 1855). This 70 Ophiuchi "planet" was soon discredited (Moulton 1899), but it likely represents the first published claim of a planet beyond the solar system.

The modern search for such planets began about a century later (Campbell et al. 1988). In less than a decade, the first planetary system was discovered around a millisecond pulsar PSR 1257 + 12 (Wolszczan & Frail 1992). It was around this time, the term *'Exoplanets'* was coined by astronomers for those planets orbiting stars other than our Sun. On the main-sequence front, long-term survey for Jupiter-mass companions for 21 Sun-like stars showed no reflex motion, indicating the absence of 1-3 M_{Jup} (Jupiter mass) planets with orbital periods less than 15 years (Walker et al. 1995). Later in the same year, Mayor and Queloz announced their discovery of 51 Pegasi b (in short as 51 Peg b), the first exoplanet to be discovered orbiting a main-sequence star (Mayor & Queloz 1995). This sub-Jupiter mass planet (0.5 M_{Jup}) orbits the star every 4.2 days, opening the doors for exotic planets that are entirely different from the planets in our Solar System.

Ever since 51 Peg b was discovered, hundreds of Jovian-mass planets were found in orbits closer than that of Mercury around Sun. These planets are called *hot Jupiters*, for their physical similarity with Jupiter, but orbit their star in short orbital periods ($P<10$ days). 51 Peg b was discovered by a method called *'Radial Velocity'* (RV for short). This method measures the stellar wobble caused by the planet to deduce the minimum mass ($m_p \sin i$; where i is the inclination angle), orbital period (P) and eccentricity (e) of the orbiting object. More recent and long-term RV surveys (eg., Hojjatpanah et al. 2019) are bringing out the full capability of RV surveys by discovering not just hot Jupiters, but also warm and cold Jupiters, Neptune-sized planets and super Earths. The planets discovered by RV method are shown as red points in Figure 1.1.

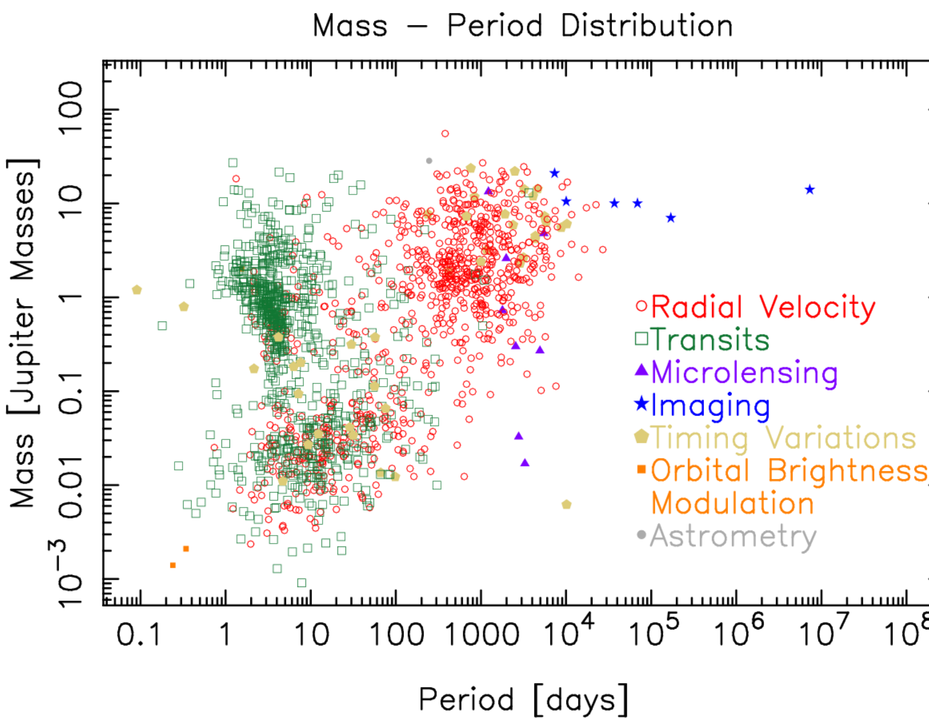

Figure 1.1: Mass vs orbital period for known exoplanets as of April 2021. Different techniques are used to successfully detect the exoplanets. Data source: NASA Exoplanet Archive, April 2021.

The recent survey from space-based telescope like *Kepler* (Borucki et al. 2010) have detected many hot Jupiters along with a huge bunch of Earth-sized planets. Kepler uses a technique called *'Transit'* to detect the planet. This method detects the minute reduction in line-of-sight flux when the planet *transits* the star when being observed. Using this technique, one can get a plethora of information like the planet's radius (R_p), orbital period (P), eccentricity (e) and orbital inclination (i). Due to the detectability limits of these methods, the most commonly discovered type of planets are massive and closer-in planets. However, if we unconstrain these limits and look at the absolute occurrence rate of planets (eg., Dressing & Charbonneau 2013; Kite et al. 2019), we find the most common type of planets are smaller (<3 $R_\oplus$) and low-mass planets (<20 $M_\oplus$). The planets discovered by various methods are shown in Figure 1.1.

1.2 Formation and evolution of low-mass planets: Importance of atmospheric evolution

Circumstellar disks of gas and dust represent the cradles of planet formation. Planets in general form within the first few tens of millions of years of their star forming. Classical core-accretion models (Weidenschilling 1977a,b; Weidenschilling & Cuzzi 1993) explain the formation mechanism of meter-sized core by collision and agglomeration of gas and dust grains. However, to cross this meter-sized core, additional changes to the core-accretion model like collision coagulation (Okuzumi et al. 2012) and turbulence clumping (Cuzzi et al. 2001) were made. With these processes, planetesimals of kilometer-size can be formed with accretion of gas. As the growing planetesimals interact gravitationally with the protoplanetary disk, they tend to migrate radially inward and collide with other planetesimals forming planets. This migration is stronger in massive planets (Lin & Papaloizou 1986). After the discovery of several hot Jupiters, the migration speed of the models have to be modified (Ida & Lin 2004a,b; Alibert et al. 2005) to reproduce the observed distribution of planets.

The *Kepler Space Telescope* finds that the most common type of exoplanets have a radius of about 1-4 $R_\oplus$ with masses ranging from 1 $M_\oplus$ to few tens of $M_\oplus$ (Howard et al. (2012); Batalha et al. (2013); Burke et al. (2014); Morton et al. (2016); Thompson et al. (2018) and many more). The mass estimates through RV measurements (Marcy et al.

2014; Weiss & Marcy 2014) and Transit Timing Variations (TTVs) (Wu & Lithwick 2013; Hadden & Lithwick 2014, 2017) show that these planets have composition and densities that are different from the terrestrial planets in our solar system. Rather than being pure rocky planets, these planets have a dense solid core surrounded by a voluminous volatile-rich atmosphere (Owen & Wu 2013, 2017).

Due to low number of samples and degeneracy present in the low-mass regime ($<50\,M_{\oplus}$; Rogers & Seager 2010), quantifying the composition of the atmospheres became difficult. However, the local stellar environment determines the state of atmospheric evolution of these planets, thereby overcoming such degeneracy. Studies such as Wu & Lithwick (2013) and Ciardi et al. (2013) show that the closer-in planets tend to be denser and smaller, suggesting that these planets might have hosted Hydrogen and Helium-rich (H/He-rich) volatile atmosphere in their initial years.

The planets found by *Kepler* through transit method tend to lie close to their parent star, thereby receiving high-energy irradiation from the star. This high-energy irradiation from the parent star is dominant in the first ∼100 million years of the planet's lifetime (Jackson et al. 2012). And planets with such H/He-rich envelopes, could be evaporated by this irradiation (Owen & Jackson 2012; Erkaev et al. 2016). The recent observational detection of such H/He-rich atmospheres evaporating in low-mass planets like GJ 436b (Kulow et al. 2014; Ehrenreich et al. 2015; Lavie et al. 2017a; dos Santos et al. 2019) and GJ 3470b (Bourrier et al. 2018; Ninan et al. 2020), support this hypothesis. Evaporation naturally results in planets that are smaller and denser than those at large separations (Lopez et al. 2012; Lopez & Fortney 2013; Owen & Wu 2017; Owen & Lai 2018). For a planet in close orbit (<0.1 AU) with low-mass ($<20\,M_{\oplus}$), its initial low-mass H/He envelope can even be entirely stripped, leaving behind a naked solid core. This explains the dearth of planets ($\sim$1 $M_\oplus$) with voluminous H/He envelopes in short orbits (<10 days) as seen in Figure 1.2 (see red shaded region).

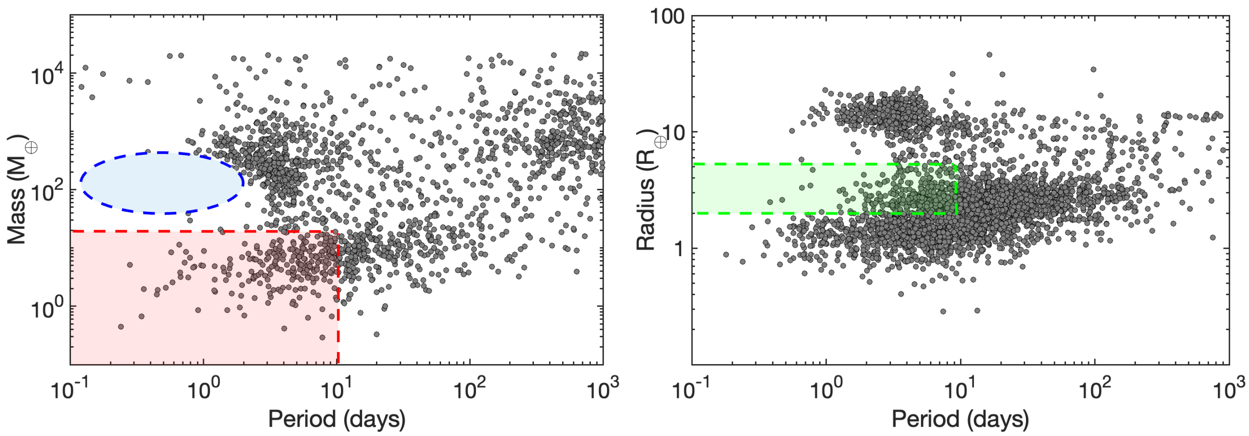

Figure 1.2: : Mass-period diagram [**Left**] and Radius-period diagram [**Right**] for known exoplanets as of April, 2021. Data source: NASA Exoplanet Archive, April 2021.

The planet's initial core mass and density play a primary role in controlling a planet's evolution by fixing the escape velocity (Lopez & Fortney 2013). This *evaporation theory* naturally explains the observed nature of Kepler planets, i.e., why these planets are large, less dense and further out, and also predicts the existence of an "Evaporation Valley", a low occupancy region ($2\,R_\oplus < R < 5\,R_\oplus$ with P<10 days) on the radius-orbital period plot (see green shaded region in Figure 1.2). This evaporation valley, separates the planets that have been completely stripped and those that are able to retain an envelope with roughly $\sim$1% in mass (Owen & Wu 2013; Lopez & Fortney 2013; Owen & Wu 2017). This prediction was replicated by statistical models shown in Jin et al. (2014), Chen & Rogers (2016) and Jin & Mordasini (2018) with different evaporation models and for different groups of planets. This makes the evaporation valley a robust prediction for radiation-driven evaporation (i.e. photoevaporation) of atmospheres of close-in H/He-rich planets.

For massive planets ($>50\,M_\oplus$), photoevaporation alone cannot explain the absence of planets in the sub-Jovian desert (see blue shaded region in Figure 1.2), as planets with mass $\geq$ 0.5 M_{Jup} can resist photoevaporation even at extremely short orbital periods (Kurokawa & Nakamoto 2014). For massive planets with mass $>$ 0.2 M_{Jup}, the mass-period distribution is consistent with high-eccentricity migration with more massive planets surviving very close to their host star (Matsakos & Königl 2016). For even more massive planets with mass $>$ 1 M_{Jup}, tidal decay allows the planet to circularize their orbit and reach shorter orbital periods. Therefore *in-situ* formation is not preferred for giant planets (Owen & Lai 2018).

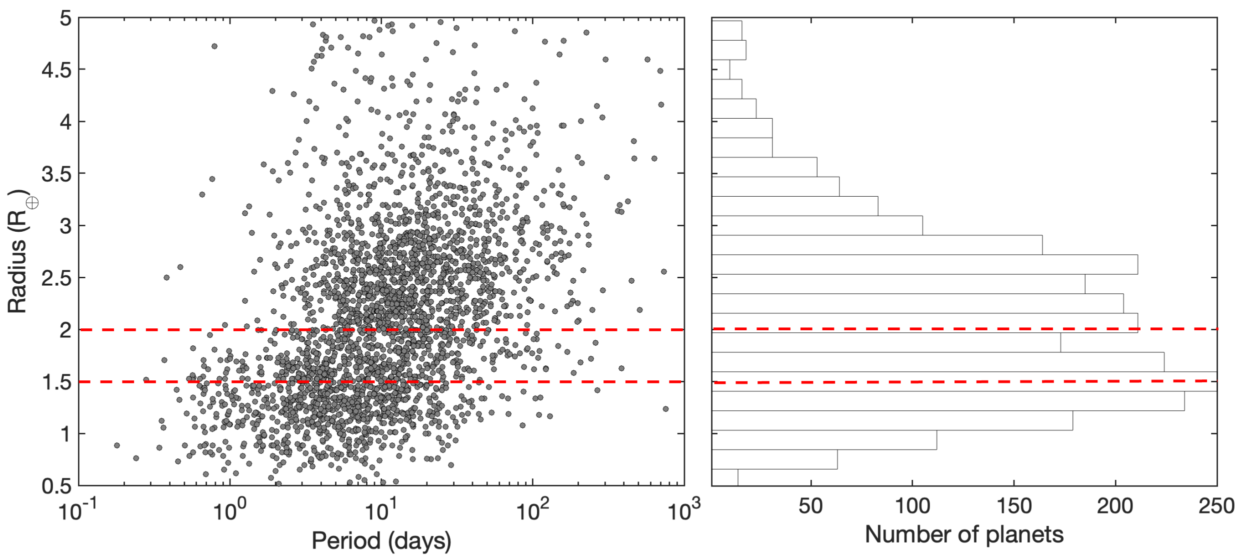

Figure 1.3: **Left**: Radius-period diagram for known exoplanets with radius smaller than 5 $R_\oplus$ as of April, 2021. **Right**: Histogram for planets shown on the left. Red dashed lines mark the Radius gap. Data source: NASA Exoplanet Archive, April 2021.

The evolution of close-in Neptune-sized planets ($2\,R_\oplus < R < 5\,R_\oplus$; P<10 days) could be different from the close-in small planets ($<2\,R_\oplus$; P<10 days). If the formation process for close-in low-mass planets produced a continuum of envelope mass fractions, then we should find the planets with intermediate masses at short periods (i.e., 100 $M_\oplus$ planets in 1-day orbits; see left plot in Figure 1.2). The smaller planets are expected to be born with small but varying amounts of low-density gas like H/He (Owen & Wu 2017) around a core of radius ∼0.8-1.5 $R_\oplus$ (Fulton et al. 2017). These gases can either be photoevaporated and become barren rocky Earth-sized or super-Earths, or could sustain the photoevaporation and retain the H/He envelope and become gaseous sub-Neptunes. This forms a bimodal distribution of planets with a "radius gap" at 1.5 - 2 $R_\oplus$ in the radius distribution plot as shown in Figure 7 of Fulton et al. (2017). This plot has been reciprocated with the additional new planets and shown in Figure 1.3 of this work.

Other mechanisms have been proposed to explain the origin of radius gap like core-powered mass loss (Ginzburg et al. 2016, 2018; Gupta & Schlichting 2019, 2020), where the luminosity of the cooling rocky core completely erode light envelopes while preserving heavy ones, produces a deficit of intermediate sized planets replicating the radius-gap. However, these class of models lack the dependence on stellar mass. The California-Kepler Survey (CKS) showed the strong dependence of stellar mass on sculpting the radius distribution of their *Kepler* samples, supporting the scenario of photoevaporation (Fulton & Petigura 2018).

In a nutshell, the planets that have dense core of $< 1.5\,R_\oplus$ and accrete $\sim 1\%$ by mass of H/He envelope, would be stripped completely of any atmosphere, if they are in a very short orbit around their parent star. Irrespective of the parent star spectra type, these form the barren rocky Earth-sized/super-Earth planets in short orbits. The planets larger than 1.5 $R_\oplus$ but smaller than the giants, with $> 1\%$ by mass of H/He envelope would either loose their atmosphere completely and become a barren planet or would survive the initial photoevaporation and be a less dense 'fluffy' planet. And finally planets with mass > 0.2-1 M_{Jup} experience high-eccentricity migration along with photoevaporation and tidal decay, but would survive being a gas giant.

However, the story does not end here. The evaporation of primordial atmospheres is just the beginning of the planet's atmosphere evolution, paving way for the formation and retention of secondary heavier, lower atmospheres. The heavier species like water are also populated in the atmosphere from the gases in protoplanetary disk and through the interaction with asteroids and comets (Kral et al. 2020). The processes mentioned above are efficient in removing the primordial nebular-derived Hydrogen and Helium atmospheres, but not the heavier species (eg., H_2O, CH_4). This is because the higher-molecular-weight volatiles such as H_2O are more easily shielded within the silicate interior, if any, and are also more resistant to escape (Kite & Barnett 2020). The classical habitable zone (HZ) is defined as the region around the star where optimum conditions exist for water to stay as liquid on the surface. A planet in the HZ does not ensure the planet is habitable, but just provides one of the necessary conditions for habitability. Another important requirement for habitability is the stable atmosphere with heavier species like H_2O, CO_2, O_2 etc (Meadows et al. 2018a).

The upcoming results from the NASA's *Transiting Exoplanet Survey Satellite-TESS* mission (Ricker et al. 2014) would provide tons of planets for atmospheric characterization. With a typical *TESS* star receiving about 27 days of continuous observation, *TESS* prefers short orbit planets (Sullivan et al. 2015). *TESS* is expected to find 1000s of planets with radii 2-4 $R_\oplus$ and >4 $R_\oplus$. Although *TESS* predominantly prefers planets around bright FGK stars, it is also expected to find about 500 planets around M-dwarfs (Barclay et al. 2018). This would definitely shed some light on this formation mechanism giving more insight on the evolution of planetary atmospheres around cool stars.

1.3 Transmission Spectroscopy

Knowledge of planet's atmosphere is critical in understanding the evolution of planets. With the current observation strategies, there are two main methods of detecting the atmosphere from an exoplanet. First method is by measuring the direct emission or reflectance spectra from a planet atmosphere. This may be detected by differencing the star plus planet light obtained during most of the planet's orbit with the light of just the star during secondary eclipse, i.e. when the exoplanet is behind its star. This method is mainly used to identify thermal inversion in the atmosphere (Sing et al. 2016). Unless the planet is very hot, big and orbiting a bright star, emission spectra and reflectance spectra will not be useful to make significant detection in the atmosphere. The next method is transmission spectroscopy. This method detects the light that passes through the planet's atmosphere as it transits in front of its star. Although the fraction of the light that passes through the atmosphere is very less, by careful reduction techniques and processes, we can identify different species in the atmosphere for a spectrally resolved transmission spectra.

Transmission spectra can be obtained from either ground-based or space-based telescopes. They can also be differentiated into low-dispersion spectroscopy with resolution, R = 100 - 500 and high-dispersion spectroscopy with resolution, R = 30,000 - 100,000. The space-based low resolution spectrographs have significantly advanced our understanding of exoplanet atmospheres, especially the *Hubble Space Telescope-HST*'s Wide Field Camera 3 (WFC3) has produced robust and repeatable observations, resulting in physically sensible atmospheric composition interpretations (Brogi et al. 2017). Its band around 1.4 μm has a strong diagnostic power since it targets major sources of opacity for exoplanet atmospheres (primarily H_2O, but also CH_4, HCN, and NH_3). However, ambiguity arises in molecular identification when spectra of multiple species overlap.

The high-dispersion spectrographs on ground-based telescopes have the capability of distinctly determining the presence of specific molecular species, despite overlap. For emission spectra, absorption and emission are intrinsically discriminated, allowing the direct detection of thermal inversion layers. Due to large opacity differences in the core and wings of the spectral line, these high-dispersion spectrographs can probe a broad range of atmospheric temperatures and pressures. The resolved planetary lines are disentangled from the telluric and stellar lines due to the planetary orbital motion allowing us to unambiguously detect atomic/molecular signatures in the atmosphere of exoplanets (Snellen et al. 2010). However, retrieving atmospheric properties for smaller planets, especially absolute molecular abundances are extremely challenging. This is due to the smaller velocity changes induced by the orbiting planet.

The first detection of an absorbing species was the sodium resonance doublet at 589 nm in the hot Jupiter HD 209458b (Charbonneau et al. 2002). Since then, Sodium, Potassium and many more optical and near-infrared (NIR) atomic/molecular opacity sources like H_2O, CO, etc. have been detected in a number of hot Jupiters (Snellen et al. 2010; Lockwood et al. 2014; Nikolov et al. 2014; Yan et al. 2019, 2021) from both space-based and ground-based facilities.

The atmospheric escape through photoevaporation, as a consequence of atmospheric evolution have been detected from transit observations of hydrogen absorption in the Lyα line for two hot Jupiters, HD 209458b (Vidal-Madjar et al. 2003) and HD 189733b (Lecavelier Des Etangs et al. 2010; Bourrier et al. 2013) and two hot Neptunes, GJ 436b (Kulow et al. 2014; Ehrenreich et al. 2015) and GJ 3470b (Bourrier et al. 2018). However, interstellar absorption limits these observations to nearby planets with gas escaping at high velocities. Also these Lyα observations have to be done from space - above Earth's atmosphere - rendering them hard and expensive for observing large number of systems.

1.3.1 Helium I triplet

The helium I triplet at 1083 nm in NIR has been identified as an interesting marker for probing an evaporating atmosphere (Seager & Sasselov 2000). This line can provide a new wavelength window over the UV lines as it is not significantly absorbed by the interstellar medium and can be observed with ground-based telescopes hosting high-resolution spectrographs (Oklopčić & Hirata 2018).

The helium atoms can exist in two configurations depending on their relative orientation of electrons' spin, i.e. singlet and triplet states. The 2^3S can be populated by recombination and collision excitation from the ground state (see Figure 1.4). The 2^3S triplet helium can radiatively decay to the singlet ground state with an exceptionally long-time of 2.2 hours (Drake 1971), making it a metastable state. It is from this metastable state, the resonance scattering to 2^3P produces an absorption line at 1083 nm. This 2^3S - 2^3P transition consists of three lines, two of which - at 1083.034 nm and 1083.025 nm are practically indistinguishable, and the third is at 1082.909 nm

This He I has been used to probe the dynamics of stellar winds, active galactic nuclei outflows, as well as the structure of the solar chromosphere and transition regime (Andretta & Jones 1997; Mauas et al. 2005). Oklopčić & Hirata (2018) developed a simple 1D model of escaping planetary atmospheres to estimate the density profile of helium in 2^3S metastable excited state and the expected in-transit absorption of this triplet line.

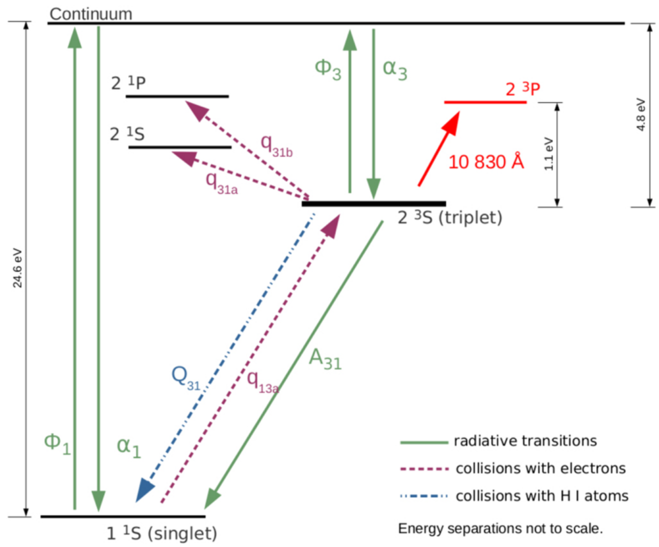

Figure 1.4: Atomic structure of the helium atom, indicating the radiative and collisional transitions. The transition shown in red depicts the 10830 Å absorption line. This figure is Figure 1 in Oklopčić & Hirata (2018)

The population of helium atoms in this excited state is governed by the spectral shape and intensity of the incident stellar radiation field (Oklopčić 2019). Higher the EUV and X-ray flux ($\lambda < 1000$ Å i.e., XUV flux), higher the population level of metastable triplet helium. This can be seen in highly active stars. Also minimizing the mid-UV flux ($\lambda >$ 1000 Å), maximizes the helium atoms in the triplet state. This can be seen in low temperature stars. Hence the ideal host star for the formation of He I absorption line in planetary atmospheres are K-type and cooler stars. These stars maximize the XUV flux and minimize the mid-UV flux, creating a 'hard' spectra. This is verified with the detection of helium absorption at 1083 nm in four K-type host star planets. Mention must be made for spectra 'softer' than K1 star, such as G- or earlier type star as they could also induce the production of triplet helium atoms if they maximize the XUV flux.

The orbital separation also plays a key role in determining the population of excited 2^3S helium atoms. At close orbital separation (a < 0.05AU) from a K-type star, significant population of 2^3S helium atoms are maintained in the atmosphere of planets (Oklopčić 2019). Although M-dwarfs have the 'hardest' spectra in regards with the He I line formation, their EUV flux is at least a order of magnitude lower than that of K-type stars. Hence planets around M-type stars need to be in much more closer orbits in order for the atmospheres to reach high fractions of triplet helium as seen around K-dwarfs (Oklopčić 2019). Mention must be made here on the possibility of existence of extended atmospheres, but not detected through this Helium I feature. This strongly depends on the atmospheric composition and the marker of interest. For example, the atmosphere can be dominant with just Hydrogen atoms which can be detected by Lyman-α measurements, but not by He I at 1083 nm. Observational results and possibilities from other wavelengths bands are briefly discussed in Section 4.9.

1.3.2 NIR molecular oxygen

Exoplanetary science is driven by the quest to find a planet that is habitable and can sustain life, thereby attempting to answer the most fundamental question, '*Are we alone?*' The search for life across the space-time pushes the boundaries of observational astronomy and requires careful consideration of the signs of life that we will be able to detect. These signs are known as "biosignatures" - life's global impact on the atmosphere and/or the planetary surface (Meadows et al. 2018a).

Molecular oxygen (O_2) has been identified as one such biosignature. As a planet-wide photosynthetic source and being the second most abundant gas in our atmosphere, O_2 screams to be considered as a biosignature. Molecular nitrogen (N_2), the most abundant gas in our atmosphere may also be biologically produced (Catling & Kasting 2007). But it is considered as a poor biosignature as N_2 exhibit strong absorption signature in extreme-UV (100 Å $< \lambda <$ 1210 Å), where it can be contaminated with other absorbing molecules like H_2O, CO, CO_2, CH_4 and other hydrocarbons. Also the spectral intensity of FGKM main-sequence stars in UV is low when compared to visbile/NIR regime, reducing the UV reflection or transmission signal from the planetary atmosphere.

On terrestrial planet, the transmission spectroscopy may not reach the near-surface environment, but can probe the stratosphere and upper troposphere (Kawahara et al. 2012; Bétrémieux & Kaltenegger 2014; Misra et al. 2014; Meadows et al. 2018b). This gives an advantage for O_2 over other complex molecules and hydrocarbons, which are susceptible to photolysis by UV radiation and so are confined largely to the lower troposphere (Meadows et al. 2018a). However, although O_2 is clearly a strong biosignature, recent research has indicated that its availability in a planetary atmosphere and its unique interpretation as a biological product may not be as straightforward as originally thought (Kawahara et al. 2012; Meadows et al. 2018a).

O_2 absorbs strongly in visible and NIR wavelengths with features in γ band at 0.628 μm, B-band at 0.688 μm, A-band at 0.762 μm and in NIR at 1.269 μm (Rothman et al. 2013; Gordon et al. 2017). O_2 can also be inferred by detecting its photochemical byproduct, ozone (O_3) which has strong bands in UV, visible and midinfrared (MIR). O_2 in high abundance can be identified by collisionally induced absorption (CIA) as O_2 molecules collide with each other, forming O_4 complex. This CIA has strong features in visible - 0.34 - 0.7 μm (Hermans et al. 1999; Thalman & Volkamer 2013) and in NIR at 1.06 μm (Greenblatt et al. 1990) and at 1.27 μm (Maté et al. 2000).

The O_2 monomer and the CIA O_4 dimer features in NIR provide an excellent wavelength window for probing the lower atmospheres of the exoplanet atmospheres. The medium-to-large class ground-based telescopes can detect the CIA features with low-to-medium resolution spectrographs and the monomer features using high resolution spectrographs (Kawahara et al. 2012). Of course these features can be probed by space-based telescopes without the telluric contamination (Lustig-Yaeger et al. 2019; Fauchez et al. 2020).

1.4 Previous observations and studies

Although its been two decades since Seager & Sasselov (2000) proposed the use of He I at 1083 nm as a marker for evaporative atmospheres, the first detection was not made until 2018. WASP-107b is the first planet to have this feature detected in its atmosphere (Spake et al. 2018). Spake et al. (2018) used the *HST*'s WFC3 instrument to detect helium in the transmission spectra of this super-Neptune orbiting a K-dwarf. This was verified by ground-based high-resolution spectrographs like CARMENES on the 3.5 m Calar-Alto observatory, Spain (Allart et al. 2019) and from the NIRSPEC on the 10 m Keck II telescope, Hawaii (Kirk et al. 2020).

Helium was also detected in the planet around other K-dwarfs like HD 189733b (Salz et al. 2018; Guilluy et al. 2020), WASP-69b (Nortmann et al. 2018; Vissapragada et al. 2020) and HAT-P-11b (Mansfield et al. 2018; Allart et al. 2018). GJ 3470b, a warm Neptune around a M-dwarf was also detected with helium in its atmosphere (Ninan et al. 2020; Palle et al. 2020). Although Moutou et al. (2003) reported a non-detection in the atmosphere of a G-dwarf hot Jupiter HD 209458b, it was detected in the successive search

Table 1.1:: Exoplanets with detected helium absorption and reported non-detection

Planet name	1083 nm transit depth	Host star spectral type	a (AU)
WASP-107b	7.26 ± 0.24 %	K6	0.055
HD 189733b	0.75 ± 0.03 %	K2	0.031
WASP-69b	3.59 ± 0.19 %	K5	0.045
HAT-P-11b	1.08 ± 0.05 %	K4	0.052
HD 209458b	0.91 ± 0.10 %	G0	0.047
GJ 3470b	1.5 ± 0.3 %	M2	0.031
HAT-P-18b	0.46 ± 0.12 %	K2	0.055
Planet name	limit on 1083 nm transit depth	Host star spectral type	a (AU)
GJ 436b	< 0.41 % (90% confidence)	M3.5	0.028
KELT-9b	< 0.33 % (90% confidence)	A0	0.035
WASP-12b	59 ± 143 ppm (over a 70 Å bin)	G0	0.023
GJ 1214b	3.8 ± 4.3 %	M4.5	0.014
K2-100b	EW < 5.7 mÅ	G0	0.029
K2-25b	EW < 17 mÅ	M4.5	0.028
WASP-127b	< 0.87 % (90% confidence)	G5	0.048
WASP-52b	< 0.47 % (95% confidence)	K2	0.0272

by Alonso-Floriano et al. (2019).

Non-detection upper-limits have been placed on several planets like GJ 436b & KELT-9b (Nortmann et al. 2018), WASP-12b (Kreidberg & Oklopčić 2018), GJ 1214b (Crossfield et al. 2019), K2-100b (Gaidos et al. 2020a), K2-25b (Gaidos et al. 2020b), τ Boo b (Zhang et al. 2020), WASP-52b (Vissapragada et al. 2020) and WASP-127b (dos Santos et al. 2020). Vissapragada et al. (2020) introduced a novel method of ultra-narrow band photometry to detect the evaporating helium during the transit. Using this method, Paragas et al. (2021) detected helium on the atmosphere of HAT-P-18b. The detected and upper-limit placed planets are shown in Table 1.1.

The detection of molecular (O_2) have not been achieved in any exoplanet as of date. However, the absorption features of O_2 have been proposed as a lower-atmosphere marker for terrestrial planets (Kawahara et al. 2012; Misra et al. 2014; Meadows et al. 2018b). The O_2 features in NIR (Greenblatt et al. 1990; Maté et al. 2000) have been used for detectability studies using space-based and ground-based telescopes. Belu et al. (2011) and Barstow & Irwin (2016) have demonstrated the plausibility of detecting terrestrial atmospheres with the *James-Webb Space Telescope*, *JWST*. Since the features are in NIR, detectability for planets around cooler and smaller stars like K-dwarfs and M-dwarfs will be enhanced. Batalha et al. (2018), Fauchez et al. (2020) and Lustig-Yaeger et al. (2019) have specifically focused on detecting the atmosphere of the infamous TRAPPIST-1 system planets (Gillon et al. 2016, 2017). Similar feasibility studies have been made for ground-based telescopes (Kawahara et al. 2012; Lopez-Morales et al. 2019) and specifically for planets in *Habitable Zone*, (HZ) (Kopparapu et al. 2013, 2014) of cooler M-dwarfs in Rodler & López-Morales (2014).

1.5 Aim of the current study

The motive for observing atmospheric escape is to understand the evolution process of planetary atmospheres. This consequently determines the demographics of exoplanetary systems. The atmospheric escape of primordial H/He atmosphere paves way for the formation and retention of secondary atmospheres of heavier atoms and molecules (Owen & Jackson 2012; Meadows et al. 2018a).

We plan to understand this atmospheric escape process on the planets around cooler stars like K-dwarfs and M-dwarfs. The atmospheric escape has been detected only for a small number of planets and in only one M-dwarf planet (see Table 1.1). We wanted to make use of the He I marker at 1083 nm and high-resolution NIR spectrographs on large ground-based telescopes to characterize the atmospheric escape. Also, the samples from California-Kepler Survey (CKS) are in a narrow range of stellar mass with $M_\star$ = 0.85 - 1.2 $M_\odot$ (Fulton et al. 2017; Fulton & Petigura 2018). Our target host stars, K-dwarfs and M-dwarfs, dwell in the lower stellar mass regime ($M_\star < 0.85$ $M_\odot$) where the planets tend to be smaller on average (Dressing & Charbonneau 2015). This would give us new insight on the radius gap for planets around cooler and smaller stars. The spectral dominance of relatively cooler stars like K-dwarfs and M-dwarfs are in NIR wavelengths supporting our choice of planets as they enhance the possibility of obtaining good signal-to-noise (SNR) in the observation.

The planets in the *Evaporation valley* or the *Radius gap* are ideal targets as they would be currently loosing their atmosphere. After the end of evaporation, the former group of planets (in the Neptunian valley) would become the gaseous sub-giants or rocky super Earths and the latter (in the radius gap) would become rocky planets with radius

< 1.5 $R_\oplus$ (Owen & Wu 2017; Fulton & Petigura 2018). Observing barren rocky planets would also give us insights as the absence of evaporative atmospheres would confirm the evaporation theory. The targets chosen for this study is shown in Table 1.2.

A subset of exoplanets we choose, would have to be optimistic targets for detecting terrestrial atmospheres. Kawahara et al. (2012) attempt to establish the detectability of the 1.27 μm O_2 feature from a future 30m class ground telescope in the HZ planets around late type stars. They assumed a highly optimistic throughput of 50%, which might not be feasible in the current technological development. Although direct detection with the current large telescopes are not possible Kawahara et al. (2012), we attempt to detect using the cross-correlation analysis. This method was not employed in the detection of O_2 in the planets around low-mass stars. Also the HZ is relatively closer to the host star when compared to hotter stars like F-type or G-type main sequence stars (Kopparapu et al. 2013, 2014, 2017). This means that if the planets in HZ transits, they create a larger transit depth and enhances the possibility of reaching lower altitudes in their atmospheres. We chose the 1.269 μm O_2 feature in the NIR as it can detect the lower abundance of O_2 as well as the high abundance due to the presence of the nearby CIA feature at 1.27 μm. Also an added advantage of choosing this feature is that we can get high SNR in our target low-mass late-type stars. The SNRs of these late-type stars are generally lower in optical wavelengths as they are relatively brighter in NIR. This study also aims to establish the detectability of NIR O_2 in M-dwarf and K-dwarf planets through a feasibility study for future 30m class telescopes (eg., TMT).

We chose the Infra-Red Doppler (IRD) instrument (Tamura et al. 2012; Kotani et al. 2014) on the 8.2 m Subaru Telescope located at Mauna Kea as our primary telescope for data source. In a nutshell, the main motives of this study are shown below:

- To understand the process of photoevaporation in planets around K-dwarf and M-dwarf stars.
- Detectability of NIR O_2 in the atmospheres of terrestrial planets through cross-correlation technique.
- Feasibility of NIR O_2 detection in the atmospheres of terrestrial planets through a future 30 m class telescope.

The targets for this study are shown in the Table 1.2 below and plotted in the radius-plot in Figure 1.5.

Table 1.2:: Targets for this study

Planet name	Radius ($R_\oplus$)	Mass ($M_\oplus$)	a (AU)	Spec. type
AU Mic b*	4.203 ± 0.02	< 57	$0.066^{+0.007}_{-0.006}$	pre-main
TRAPPIST-1b$^\#$	$1.116^{+0.014}_{-0.012}$	1.374 ± 0.069	0.01154 ± 0.0001	M8
TRAPPIST-1e$^\#$	$0.920^{+0.013}_{-0.012}$	0.692 ± 0.022	0.02925 ± 0.00025	M8
TRAPPIST-1f$^\#$	$1.045^{+0.013}_{-0.012}$	1.039 ± 0.031	0.03849 ± 0.00033	M8
TOI-1235b**	$1.738^{+0.087}_{-0.076}$	$6.91^{+0.75}_{-0.85}$	$0.03845^{+0.00037}_{-0.00040}$	M0.5
GJ 9827b$^+$	1.529 ± 0.058	4.87 ± 0.37	0.01866 ± 0.00019	K5
GJ 9827d$^+$	1.955 ± 0.075	3.29 ± 0.64	$0.0555^{+0.00055}_{-0.00057}$	K5
HIP 67522b^{++}	$10.07^{+0.47}_{-0.47}$	-	$0.07535^{+0.00154}_{-0.00179}$	G0

Note: * Plavchan et al. (2020); $^\#$ Agol et al. (2021) $^+$ Kosiarek et al. (2021) ** Cloutier et al. (2020) $^{++}$ Rizzuto et al. (2020)

The target AU Mic b is an interesting target as it a 22 Myr old young system with a debris disk (Grady et al. 2020; Plavchan et al. 2020). AU Mic is one of the youngest

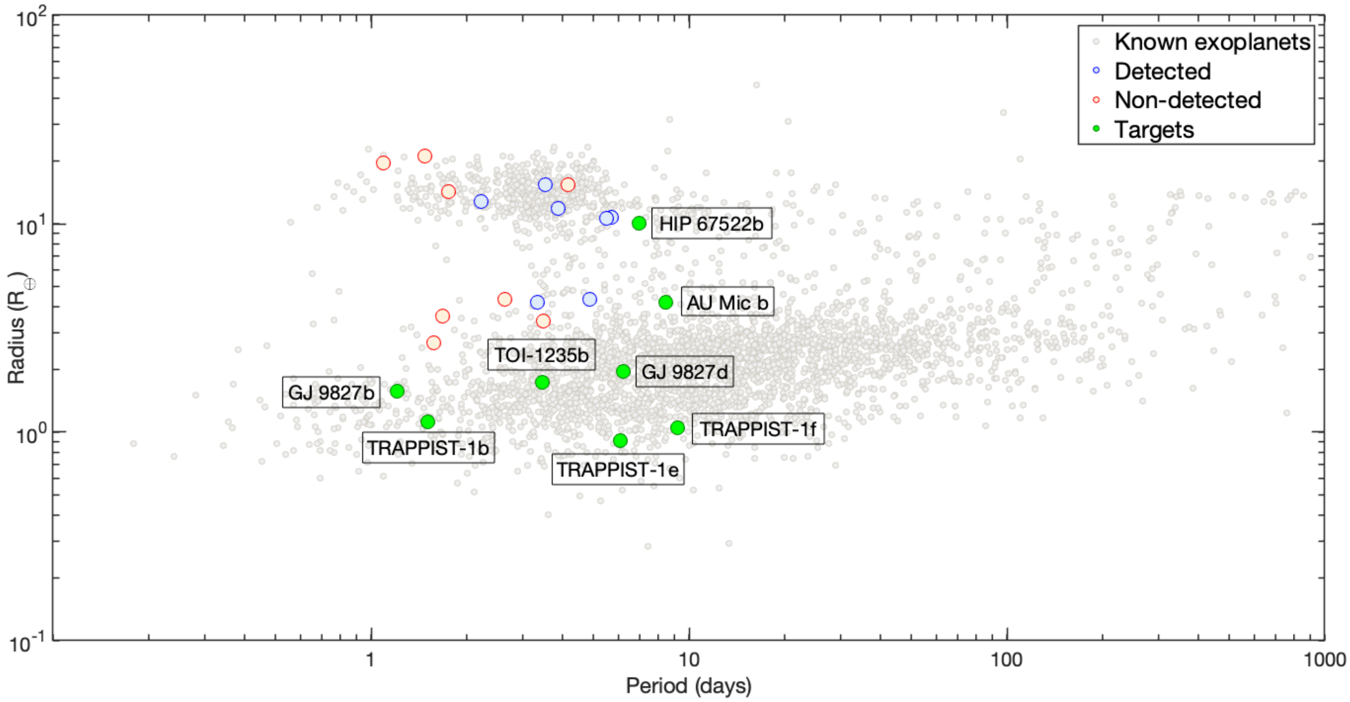

Figure 1.5: Targets for this study shown in the radius-period plot along with the known exoplanets. Data source: NASA Exoplanet Archive, April 2021.

systems known to host a transiting close-in planet, making our study an important benchmark to compare to models of the evolution of close-in planets (Hirano et al. 2020b). The infamous TRAPPIST-1 system's Earth-sized planets form the lower boundary on radius-period plot (see Figure 1.5) and the limit on detectability of any atmosphere as they orbit an ultra-cool star. These planets are excellent benchmark targets for probing the lower atmosphere with the current ground-based high resolution spectrographs and on future 30m class telescopes. Also since the system is very old, probing the lower atmospheres would give us some insights on the evolution of secondary atmosphere. The small size of this late M-dwarf combined with ultra-short period Earth-sized planets provides the excellent test-case for probing the habitability of the planets. The planets GJ 9827b and GJ 9827d, orbiting a K-dwarf form the upper and lower boundaries of the planet radius gap (Carleo et al. 2021), making them excellent targets to understand the significance of radius gap. TOI-1235b is a keystone super-Earth in the radius gap, providing us with an excellent opportunity to understand the emergence of radius-gap. The target HIP 67522b is an opportune young hot Jupiter that is transiting (Rizzuto et al. 2020). This planet is further away in orbit when compared to all the He I detected hot-Jupiters. Detecting helium in such a young planet would confirm the evaporation hypothesis in longer orbital planets.

Detailed information on observations, results and discussions are presented in the successive chapters.

Chapter 2

Observation and extraction of transmission spectra

"Somewhere something incredible is waiting to be known." - Carl Sagan, 1977

2.1 Observations

Observations were carried out on the 8.2m Subaru Telescope, the flagship telescope of National Astronomical Observatory of Japan (NAOJ), Japan. We used the IRD - InfraRed Doppler instrument (Tamura et al. 2012; Kotani et al. 2014), a high-resolution fiber-fed echelle spectrograph that covers the wavelength from 0.97 μm - 1.75 μm with a resolution of R$\sim$70,000 for our analysis. The wavelength is simultaneously calibrated with the laser frequency comb (LFC). The wavefront is corrected by the adaptive optics system, AO188 before it is injected into the fiber. All the instruments are sealed in a vacuum chamber and cooled down to $\sim$180 K for the optics and $\sim$80 K for the detector to ensure reduction in thermal-background and dark noise. The detector consists of two units of HAWAII 2 RG detectors (Loose et al. 2003) and the gain is maintained at 2.99 e^-/ADU in the Y-J-band detector and 2.78 e^-/ADU in the H-band detector. The observations were conducted from August 2018 to April 2021 and are described in the section below.

2.1.1 AU Mic b

AU Microscopii (AU Mic) is the second closest pre-main sequence star at a distance of just 9.79 parsecs and with an age of 22 million years (Mamajek & Bell 2014). It is known to host a spatially resolved edge-on debris disk extending from 35 AU to 210 AU from the central star (Strubbe & Chiang 2006). A 0.4 R_{Jup} planet within the debris disk was discovered in 2020 (Plavchan et al. 2020).

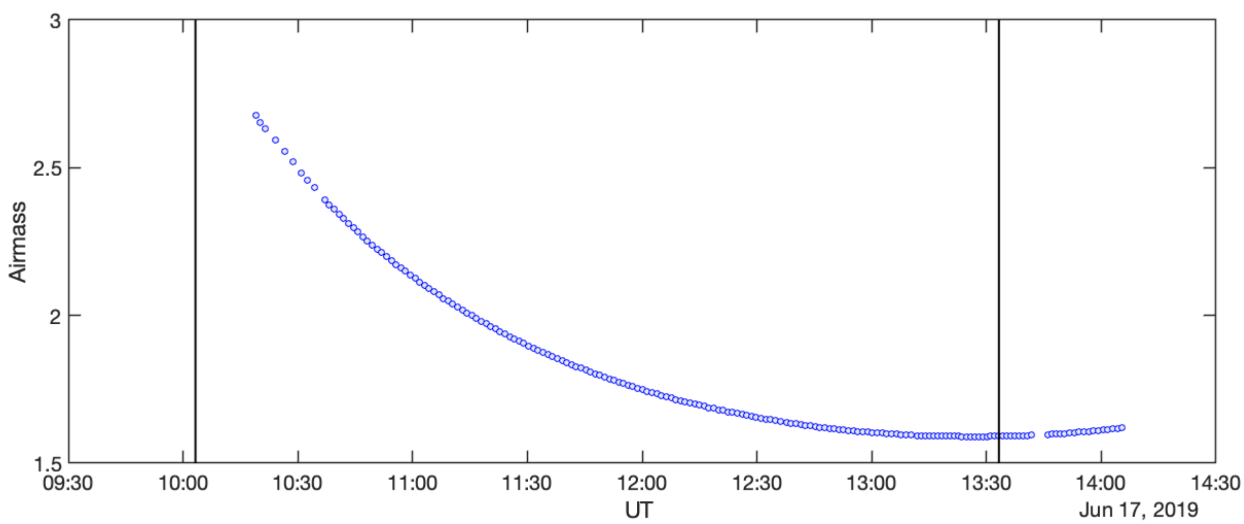

Figure 2.1: Airmass variation on the night of observation of AU Mic b's transit (UT June 17, 2019). The vertical lines correspond to the beginning and end of transit. The first fifteen minutes of the transit was lost due to low elevation.

This transit of this planet was observed from Subaru telescope with IRD on UT 2019

June 17. The ingress with first 15 minutes of transit was missed due to low elevation, but egress and 40 minutes after the transit was captured. We interrupted this observation to capture a rapid rotating A0 star, HIP 98926 for telluric correction. After obtaining the rapid rotator spectra, the observation was continued for the AU Mic throughout the night. The integration time was set to 60 seconds. A total of 179 frames were obtained that night. The airmass variation for the target is shown in Figure 2.1 on the night of observation. The planet's parameters are shown in the Table 2.1 below.

Table 2.1:: AU Mic system

Stellar radius ($R_\odot$)	$0.75 \pm 0.03^{(a)}$	Stellar mass ($M_\odot$)	$0.50 \pm 0.03^{(b)}$
Spectral type	pre-main	T_{eff} (K)	$3700 \pm 100^{(c)}$
Planet name	AU Mic b	Planet radius ($R_\oplus$)	4.203 ± 0.02
Planet mass ($M_\oplus$)	< 57	Impact parameter (b)	$0.16\ ^{+0.14}_{-0.11}$
Period (days)	8.46321 ± 0.00004	Transit duration (hours)	$3.50\ ^{+0.63}_{-0.59}$
T_c (BJD)	$2458330.39153^{+0.00070}_{-0.00068}$	Semi-major axis, a (AU)	$0.066\ ^{+0.007}_{-0.006}$

Note: $^{(a)}$ White et al. (2015); $^{(b)}$ + all planet parameters Plavchan et al. (2020); $^{(c)}$ Plavchan et al. (2009)

This study also used the simultaneous transit observation data from Keck II/NIRSPEC (McLean et al. 1998) and University of Hawaii 2.2 m telescope's SNIFF spectrograph's data. The results of this observation is presented in Hirano et al. (2020b).

2.1.2 GJ 9827 system

GJ 9827, a bright (V-mag = 10.39) late K-dwarf plays host to three super-Earths (Niraula et al. 2017; Rodriguez et al. 2018). The planets GJ 9827b and GJ 9827d form the lower and upper boundaries of the radius gap (see Figure 1.5), making them excellent targets for atmospheric studies. The transits of GJ 9827b and GJ 9827d were occurring on the same night on the night of UT 5 September 2020. We took this golden opportunity and secured one full-night of observation from Subaru Telescope to observe using the IRD. The observation was carried out under the program S20B-069 (PI: Krishnamurthy). On the night of observation, we spared 2 hours of observation time to observe another target. The airmass variation is shown in the Figure 2.2 below.

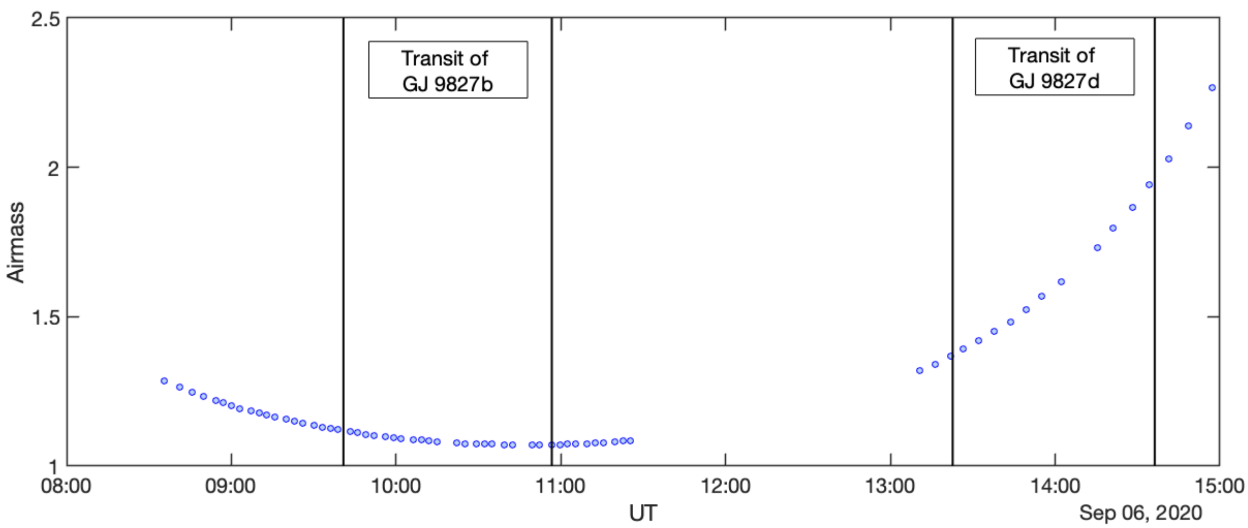

Figure 2.2: Airmass variation on the night of observation of GJ 9827b and GJ 9827d's transit (UT 06 September 2020). The vertical lines correspond to the beginning and end of transit for both the planets.

The airmass during the transit of GJ 9827d was high and increasing due to the low elevation of the star. Also the seeing became bad during the second half of the night.

Integration time was initially set at 180 seconds, to obtain an SNR-per-pixel of 110 at 1 micron. Due to the bad seeing and low elevation, the integration time was increased to 300 seconds and further to 360 seconds, by the end of the night to maintain the same SNR. We also lost 2 frames due to technical error. A total of 66 usable frames of GJ 9827 were obtained by the end of observation. The star and planet parameters used in the analysis are shown in the Table 2.2 below.

Table 2.2:: GJ 9827 system

Stellar radius ($R_\odot$)	0.579 ± 0.018	Stellar mass ($M_\odot$)	0.593 ± 0.018
Spectral type	K6	T_{eff} (K)	4294 ± 52
Planet name	GJ 9827b	Planet radius ($R_\oplus$)	1.529 ± 0.058
Planet mass ($M_\oplus$)	4.87 ± 0.37	Impact parameter (b)	$0.493\ ^{+0.080}_{-0.12}$ [b]
Period (days)	1.2089765 ± 2.3e-06	Transit dur. (hours)	$1.25976\ ^{+0.01776}_{-0.01704}$ [b]
T_c (BJD)	2457738.8258±0.0003[c]	a (AU)	0.01866±0.00019
Planet name	GJ 9827d	Planet radius ($R_\oplus$)	1.955 ± 0.075
Planet mass ($M_\oplus$)	3.29 ± 0.64	Impact parameter (b)	$0.896\ ^{+0.012}_{-0.016}$ [b]
Period (days)	6.20183 ± 1e-05	Transit dur. (hours)	$1.2264\ ^{+0.0264}_{-0.024}$ [b]
T_c (BJD)	2457740.9611±0.0004[b]	a (AU)	$0.0555\ ^{+0.00055}_{-0.00057}$

Note: All parameters unless specifed are from Kosiarek et al. (2021); [b] Rodriguez et al. (2018) [c] Rice et al. (2019)

The density derived from the above parameters, gives planet 'b' a density of 1.35 $\rho_\oplus$ and planet 'd' a density of 0.45 $\rho_\oplus$, making planet 'd' an excellent target for detecting the evaporating atmospheres. We also observed 6 frames A1 rapid rotating star, HIP 8296 for telluric corrections by the end of the night.

2.1.3 TRAPPIST-1 system

Since the discovery of the seven planets orbiting the ultra-cool dwarf TRAPPIST-1 (Gillon et al. 2016, 2017), the system has caught the attention of the exoplanet community. The planets of this old system (7.6 $\pm$ 2.2 Gyr; Burgasser & Mamajek 2017) are in a complex chain of resonant orbits with three planets in the star's habitable zone (Luger et al. 2017). Its low mass (0.09 $M_\odot$; Van Grootel et al. 2018) and high multiplicity of seven Earth-sized transiting planets (Grimm et al. 2018) made it the primary target for several observational programs. Several transits of TRAPPIST-1 planets have been observed with the *Spitzer Space Telescope* (Delrez et al. 2018; Ducrot et al. 2020; Agol et al. 2021), *HST* (de Wit et al. 2016; Bourrier et al. 2017; de Wit et al. 2018; Wakeford et al. 2019), *K2*-mission (Luger et al. 2017) and ground-based observatories (Gillon 2018; Hirano et al. 2020a). From HST/WFC3 observations, de Wit et al. (2016) and de Wit et al. (2018) claim that the planets TRAPPIST-1b, c, d, e and f lack cloud-free hydrogen-dominated atmospheres. Bourrier et al. (2017) detected a marginal flux decrease during their Ly-α measurements of TRAPPIST-1b transit using *HST*'s Space Telescope Imaging Spectrograph (STIS), but could not confirm the presence of an extended atmosphere. Hori & Ogihara (2020) found that all the primordially accreted hydrogen-rich atmospheres of TRAPPIST-1 planets would have been lost via hydrodynamic escape in the first few hundred Myr of planet formation. The parameters of TRAPPIST-1 with its planets b, e and f used in the analysis are shown below in the Table 2.3.

We observed a transit of TRAPPIST-1b on the night of UT 17 September 2020. This observation was carried out as a part of 2 open-use observation programs: S20B-069 (PI: Krishnamurthy) and S20A-UH104 (PI: Gaidos). The exposure time was set to

Table 2.3:: TRAPPIST-1 system

Stellar radius ($R_\odot$)	0.1192 ± 0.0013	Stellar mass ($M_\odot$)	0.0898 ± 0.0023$^{(b)}$
Spectral type	M8	T_{eff} (K)	2566 ± 26
Planet name	TRAPPIST-1b	Planet radius ($R_\oplus$)	$1.116^{+0.014}_{-0.012}$
Planet mass ($M_\oplus$)	1.374 ± 0.069	Impact parameter (b)	$0.095\ ^{+0.065}_{-0.061}$
Period (days)	1.510826±0.000006	Transit dur. (mins)	36.06 ± 0.11
T_c (BJD)	2457257.55044±0.00015	a (AU)	0.01154 ± 0.0001
Planet name	TRAPPIST-1e	Planet radius ($R_\oplus$)	$0.920^{+0.013}_{-0.012}$
Planet mass ($M_\oplus$)	0.692 ± 0.022	Impact parameter (b)	$0.191\ ^{+0.041}_{-0.041}$
Period (days)	6.101013±0.000035	Transit dur. (mins)	55.76 ± 0.26
T_c (BJD)	2457257.82771±0.00041	a (AU)	0.02925 ± 0.00025
Planet name	TRAPPIST-1f	Planet radius ($R_\oplus$)	$1.045^{+0.013}_{-0.012}$
Planet mass ($M_\oplus$)	1.039 ± 0.031	Impact parameter (b)	$0.312\ ^{+0.023}_{-0.018}$
Period (days)	9.207540±0.000032	Transit dur. (mins)	62.85 ± 0.25
T_c (BJD)	2457257.07426±0.00085	a (AU)	0.03849 ± 0.00033

Note: All parameters unless specifed are from Agol et al. (2021); $^{(b)}$ Mann et al. (2019)

300 seconds. We obtained 21 frames of TRAPPIST-1. We ended the observation with 3 frames of a rapidly-rotating A1 star, HIP 117774 to aid in telluric corrections. On that particular night, we had high winds and moderate seeing of ≈ 0.5”. On the transit night, the extracted 1D spectra had a per-pixel SNR of 19-20 at 1.0 μm. The airmass variation on the night of the transit is shown in the Figure 2.3.

We also used the data presented in Hirano et al. (2020a) in our analysis, where the transit of TRAPPIST-1b, e and f were captured (UT 2018 August 30). The primary

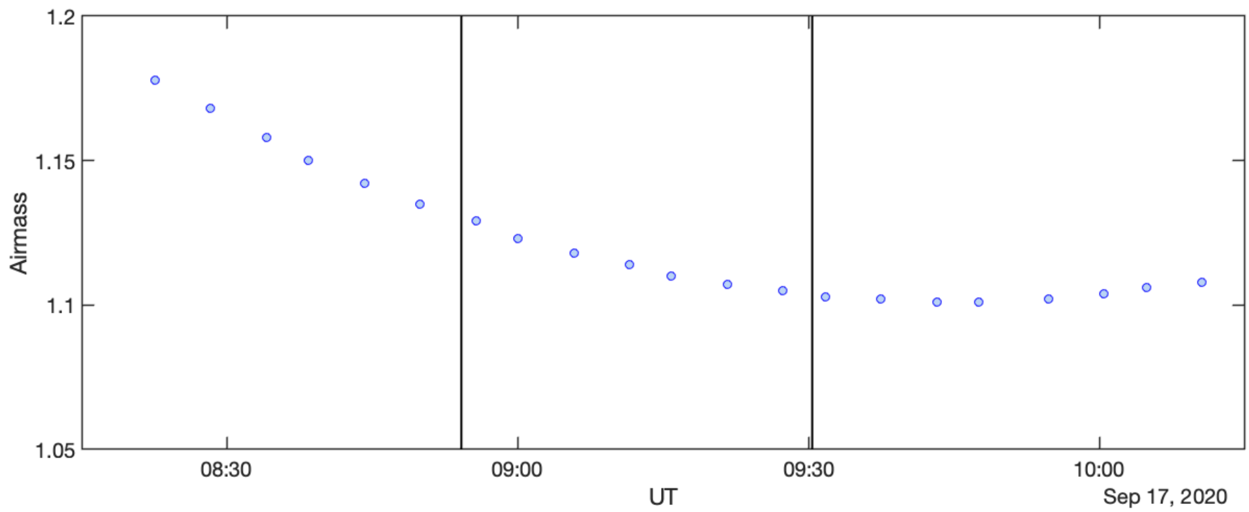

Figure 2.3: Airmass variation on the night of observation of TRAPPIST-1b's transit (UT 17 September 2020). The vertical lines correspond to the beginning and end of transit.

focus of their paper was the Rossiter–McLaughlin (RM) effect measurements and not atmosphere characterization. The per-pixel SNR for both these observations were similar and were from the same instrument, IRD.

Three more transits of TRAPPIST-1b were captured from the 10 m Hobby-Eberly telescope's Habitable-zone Planet Finder (HPF), fiber-fed high resolution (R = 55000) spectrograph (Mahadevan et al. 2012, 2014) on UT 02 October 2018, 31 July 2019 and 05 September 2020. The main focus of this study is the Rossiter–McLaughlin (RM) effect measurement on M-dwarf planets (Stefansson 2019). They obtained six 315-second exposures during transits for the first and third nights, with only three exposures for the second night due to bad weather. These spectra had a median SNR of 38, 14, and 31 at 1.0 μm per 1D extracted pixel, respectively. Due to low S/N of the data for the second transit, we did not use those spectra for the subsequent analysis. In addition to the in-transit data, they obtained out-of-transit observations from separate nights to create a high SNR out-of-transit reference spectrum from 68 out-of-transit spectra obtained with an exposure time of 315 seconds and 13 other spectra with an exposure time between 415 seconds and 1224 seconds.

2.1.4 TOI-1235b

TOI-1235 is a weakly active M0.5 star (Lépine et al. 2013), hosting a super-Earth in the radius gap (Cloutier et al. 2020; Bluhm et al. 2020). The emergence of radius gap in low-mass stars is not well established and this keystone planet, TOI-1235b could potentially provide some useful insight on evolution of radius gap planets' atmospheres.

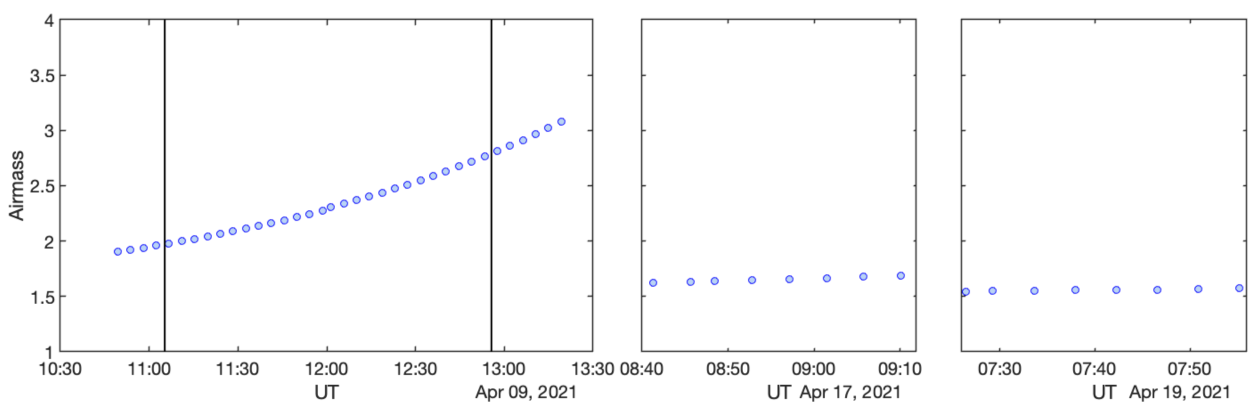

Figure 2.4: Airmass variation on the night of observation of TOI-1235b's transit (UT 09 April 2021) and other nights. The vertical lines correspond to the beginning and end of transit.

We observed a transit of TOI-1235b on UT 09 April 2021 under the program S21A-100N (PI: Krishnamurthy). Due to low elevation, we observed TOI-1235 for only 20 minutes after the transit ended and shifted to a A1-type rapid-rotator HIP 60044 for telluric corrections. Few more frames of TOI-1235 were obtained, when there was no known planets transiting on different nights to disentangle the telluric features from the stellar spectra. The airmass variation is shown in the Figure 2.4.

We had a good seeing on the night of UT 09 April 2021. The integration time was set to 240 seconds. In total we obtained 36 frames on UT 09 April 2021, 8 frames on UT 17 April 2021 and 8 frames on UT 19 April 2021. We obtained a per-pixel SNR of ~ 60 at 1μm in the 1-D reduced spectra. The Table 2.4 shows the parameters of the of the system used in the analysis.

Table 2.4:: TOI-1235 system

Stellar radius ($R_\odot$)	0.630 ± 0.015	Stellar mass ($M_\odot$)	0.640 ± 0.016
Spectral type	M0.5	T_{eff} (K)	3872 ± 70
Planet name	TOI-1235b	Planet radius ($R_\oplus$)	$1.738^{+0.087}_{-0.076}$
Planet mass ($M_\oplus$)	$6.91^{+0.75}_{-0.85}$	Impact parameter (b)	$0.45\ ^{+0.21}_{-0.19}$
Period (days)	$3.444729^{+0.000031}_{-0.000028}$	Transit duration (hours)	$1.84\ ^{+0.09}_{-0.16}$
T_c (BJD)	$2458845.51696^{+0.00099}_{-0.00098}$	Semi-major axis, a (AU)	$0.03845\ ^{+0.00037}_{-0.00040}$

Note: All parameters are from Cloutier et al. (2020)

2.1.5 HIP 67522b

HIP 67522 is a bright (V-mag = 9.80) and very young G-dwarf (17 Myr; Rizzuto et al. 2020) in the Sco-Cen OB association (de Zeeuw et al. 1999). Recently, a hot Jupiter, HIP 67522b was discovered by the *TESS* mission and confirmed by *Spitzer*'s IRAC CH2 photometry (Rizzuto et al. 2020). The transit of HIP 67522b was observed through IRD in the program S21A-129 (PI: Hirano) on UT 16 April 2021. The airmass variation on the night of transit in shown in the Figure 2.5.

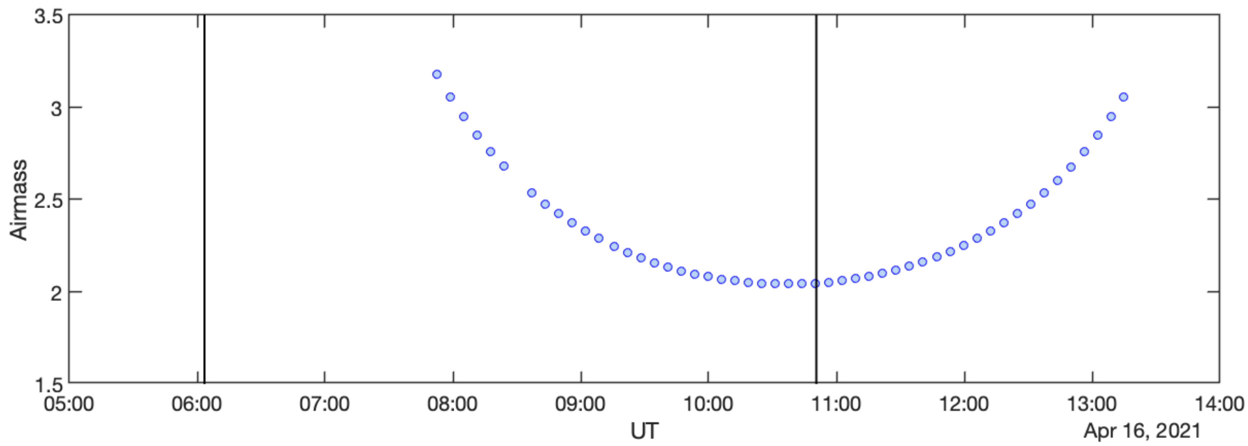

Figure 2.5: Airmass variation on the night of observation of HIP 67522b's transit (UT 16 April 2021). The vertical lines correspond to the beginning and end of transit.

About 65% of the transit was captured in this observation. On the transit night, there was moderate seeing of 0.9". A total of 50 frames were obtained on the night of transit with an integration time of 360 seconds. A SNR at 1μm of the 1-D reduced spectra was around 80. Additional 29 frames were obtained on different (non-transiting) nights with the same exposure time of 360 seconds. During these other non-transit observation nights, due to good seeing and high elevation of the target, the SNR reached around 110 at 1μm of the 1-D reduced spectra. The parameters used in the analysis are shown in the Table 2.5.

This 17 million year old infant system provides an interesting benchmark on the detection of evaporating atmospheres in hot main-sequence stars. Being a very young hot Jupiter, HIP 67522b is expected to be loosing Earth-masses of atmosphere per billion years due to photoevaporation (Kurokawa & Nakamoto 2014). As this planet is farther

Table 2.5:: HIP 67522 system

Stellar radius ($R_\odot$)	1.38 ± 0.06	Stellar mass ($M_\odot$)	1.22 ± 0.05
Spectral type	G0	T_{eff} (K)	5675 ± 75
Planet name	HIP 67522b	Planet radius ($R_\oplus$)	$10.07^{+0.47}_{-0.47}$
Planet mass ($M_\oplus$)	–	Impact parameter (b)	$0.134\ ^{+0.106}_{-0.092}$
Period (days)	$6.959503^{+0.000016}_{-0.000015}$	Transit duration (hours)	$4.822\ ^{+0.021}_{-0.019}$
T_c (BJD)	$2458604.02371^{+0.00036}_{-0.00037}$	Semi-major axis, a (AU)	$0.07535^{+0.00154}_{-0.00179}$

Note: All parameters are from *TESS* and *Spitzer* IRAC CH2 photometry presented in Rizzuto et al. (2020)

from its star than the other He I detected hot Jupiters, it can also test the prediction of evaporative models (Owen & Wu 2013, 2017).

2.2 Telluric correction

The observed IRD data were reduced to 1-D spectra using the `IRAF` package (Tody 1993) and wavelength calibrated following the steps of Hirano et al. (2020c). Each reduced 1-D spectra are checked for any intrinsic errors in the flux value. After verifying the flux, each spectra is normalized and is ready for analysis.

In the case of high-resolution transmission spectra, the telluric contamination can interfere with the analysis, especially with narrow absorption/emission features. Hence it is necessary to remove these features before the analysis. In this work, we employ two steps of telluric correction. First the correction using a secondary spectra of a rapid-rotating star (Jensen et al. 2012; Winn et al. 2004; Kawauchi et al. 2018). Rapid-rotating stars have highly broadened and shallow spectra owing to their rapid rotation. Hence while observing from ground, these can be regarded as pure telluric spectra as the stellar spectra are flattened. Assuming that Earth's atmosphere is a plane parallel atmosphere, the depth of the telluric absorption lines depends on the volume of air passed (airmass). Therefore, if the airmass at the observation time of target star is known, we can calculate the telluric spectrum at the observation time as,

$$T\left(\lambda\right) = T_o\left(\lambda\right)^{\left(\frac{a}{a_o}\right)} \tag{2.1}$$

where $\mathrm{T}\left(\lambda\right)$ is the telluric spectra at the time of observation with airmass, 'a'; and $\mathrm{T_o}\left(\lambda\right)$ is the telluric template spectra (i.e., the rapid-rotator spectra) at the airmass, '$\mathrm{a_o}$'. To obtain the telluric-free spectra, we divide the stellar spectra, $\mathrm{F}\left(\lambda\right)$ by this telluric spectra at the time of observation, $\mathrm{T}\left(\lambda\right)$ as seen in the equation 2.2 below.

$$F'\left(\lambda\right) = \frac{F\left(\lambda\right)}{T\left(\lambda\right)} \tag{2.2}$$

The telluric corrected spectra $\mathrm{F}'\left(\lambda\right)$, is not entirely telluric-free. This is due to the instantaneous variation in the Earth's atmosphere, especially the water-vapor content, wind velocity, etc. Such instantaneous variations are very difficult to remove and require additional simultaneous measurements, like precipitable water-vapor (PWV), from a radiometer (Kawauchi et al. 2018). In the current study, instead of other simultaneous measurements, we employed `SYSREM` algorithm (Tamuz et al. 2005). This second step of telluric correction uses a detrending algorithm to fit the systematic trend in the wavelength bin direction and remove any systematic effects such as airmass variation, water-vapor column variation, detector errors, etc (Nugroho et al. 2021). This algorithm, although was initially presented for photometric studies, have been successfully employed for high resolution spectroscopy (eg., Birkby et al. 2013).

Consider the case of M individual observation frames of a target, each with N wavelength bins. r_{ij} is defined as the residue after subtracting the mean flux in a particular wavelength bin 'i'.

$$r_{ij} = F'_{ij}(\lambda) - \frac{1}{N}\sum_{i=1}^{N} F'_{ij}(\lambda) \tag{2.3}$$

Let $\{a_j;\ j = 1, ..., M\}$ be the airmass at the j^{th} observation. If we define c_i as the effective extinction coefficient in the wavelength bin 'i' to be the slope of the best linear fit for the residuals, then our aim is to find the best c_i that minimizes the expression,

$$S_i^2 = \sum_j \frac{(r_{ij} - c_i a_j)^2}{\sigma_{ij}^2} \tag{2.4}$$

where, σ_{ij} is the uncertainty in the measurement. With airmasses known, a simple differentiation and equating to zero yields an estimate for the extinction coefficient:

$$c_i = \frac{\sum_j \left(\frac{r_{ij} a_j}{\sigma_{ij}^2}\right)}{\sum_j \left(\frac{a_j^2}{\sigma_{ij}^2}\right)} \tag{2.5}$$

Here each c_i is independent of all other c_i. Because atmospheric extinction might depend not only on the airmass but also on weather conditions, we can ask ourselves what is the most suitable 'airmass' of wavelength bin, given the known coefficient of every wavelength bin (Tamuz et al. 2005). Hence the best a_j that minimizes the expression,

$$S_j^2 = \sum_i \frac{(r_{ij} - c_i a_j)^2}{\sigma_{ij}^2} \tag{2.6}$$

is given by,

$$a_j^{(1)} = \frac{\sum_i \left(\frac{r_{ij} c_i}{\sigma_{ij}^2}\right)}{\sum_i \left(\frac{c_i^2}{\sigma_{ij}^2}\right)} \tag{2.7}$$

Note that this a_j might be very different from the actual airmass of that particular observation. We can now recalculate the best-fitting $\{c_i^{(1)}\}$ and continue iteratively. The new residue is calculated as,

$$^{(1)}r_{ij} = r_{ij} - c_i^{(1)} a_j^{(1)} \tag{2.8}$$

For the successive iterations, the same procedure is followed and the residue after k^{th} iteration is calculated as,

$$^{(k)}r_{ij} =^{(k-1)} r_{ij} - c_i^{(k)} a_j^{(k)} \tag{2.9}$$

In essence, we are looking for the best-fitting $\{\bar{c}_i\}$ and $\{\bar{a}_j\}$ that accounts for the atmospheric extinction. However, the number of iterations of `SYSREM` plays a key role in determining the usefulness of the residues. Several iterations of `SYSREM` can over-correct the atmospheric extinction and possibly remove planetary signals, if any (Yan et al. 2020). Hence in the current study, we analyse the data after each iteration of `SYSREM` algorithm.

In the case of He I analysis, if there are no known positions of telluric OH and H_2O features near the vicinity of the He I lines, we do not perform the `SYSREM` algorithm. This is to avoid any unnecessary removal of planetary signals (Yan et al. 2020).

2.3 Extraction of transmission spectrum

The telluric corrected residues/spectra are currently in the observer's rest frame (a.k.a. telluric rest frame). In order to make sense of planetary data, we must shift them to planet's rest frame. The first of this is to shift them to the stellar rest frame. The absolute RV of the system used in our analysis are given below in the Table 2.6.

Table 2.6:: Absolute RV of target systems

System	RV (km/s)	Reference
AU Mic	-4.25	Schneider et al. (2019)
GJ 9827	31.9	Sperauskas et al. (2016)
TRAPPIST-1	-52.5	Hirano et al. (2020a)
TOI-1235	-27.75	Gaia Collaboration (2018)
HIP 67522	5.40	Kharchenko et al. (2007)

After transferring the residues/spectra to stellar rest frame, we correct for the Doppler-shift induced by the transiting planet. This shifts the residues/spectra to the planet's rest frame. Each frame is then binned into evenly spaced wavelength bins. The frames obtained when no planet is transiting would have only the star's spectral features. In the case of `SYSREM` corrected residues, assuming the stellar spectra did not change drastically, we will end up with flat featureless spectra. We median-combined all the out-of-transit frames to form the master out-of-transit frame, $\mathcal{F}_{\text{star}}(\lambda)$. The frames obtained during transit would have planetary signatures imprinted on the stellar spectra. All the transit frames are median-combined to form the master in-transit frame, $\mathcal{F}_{\text{intransit}}(\lambda)$. Assuming there is no drastic change in stellar spectra during the observation, the transmission spectra, $\mathcal{F}_{trans}(\lambda)$ is created by dividing the master in-transit spectra, $\mathcal{F}_{\text{intransit}}(\lambda)$ by the pure stellar spectra (or the flat residues if the spectra is treated by `SYSREM` algorithm), $\mathcal{F}_{\text{star}}(\lambda)$ as shown below.

$$\mathcal{F}_{trans}(\lambda) = \mathcal{F}_{\text{intransit}}(\lambda) / \mathcal{F}_{\text{star}}(\lambda) \tag{2.10}$$

This computed transmission spectra for each planet is now ready for analysis in the upcoming chapters.

Chapter 3

Results of atmospheric analysis

"Science requires speculation, creativity, and wild ideas." - Debra Fischer

3.1 Analysis of transmission spectra: He I triplet at 1083 nm

3.1.1 AU Mic b

This subsection originally appeared in the literature in the paper: *"Limits on the Spin-Orbit Angle and Atmospheric Escape for the 22 Myr-old Planet AU Mic b"*

Authors: Teruyuki Hirano, Vigneshwaran Krishnamurthy, Eric Gaidos et al.

Journal: The Astrophysical Journal Letters

Year: 2020

The transmission spectra of AU Mic b from IRD and NIRSPEC around the He I triplet is shown in the Figure 3.1. The strongest doublet of the He I triplet, did not show any significant difference during the transit to indicate the presence of any planet related absorption. The difference spectra, i.e., in transit - out of transit in percentage is used instead of the flux ratio (in/out), as the feature is not seen clearly in the flux ratio spectra. The stellar He I positions are not contaminated by strong telluric lines. Hence extensive telluric line removal procedure is not done.

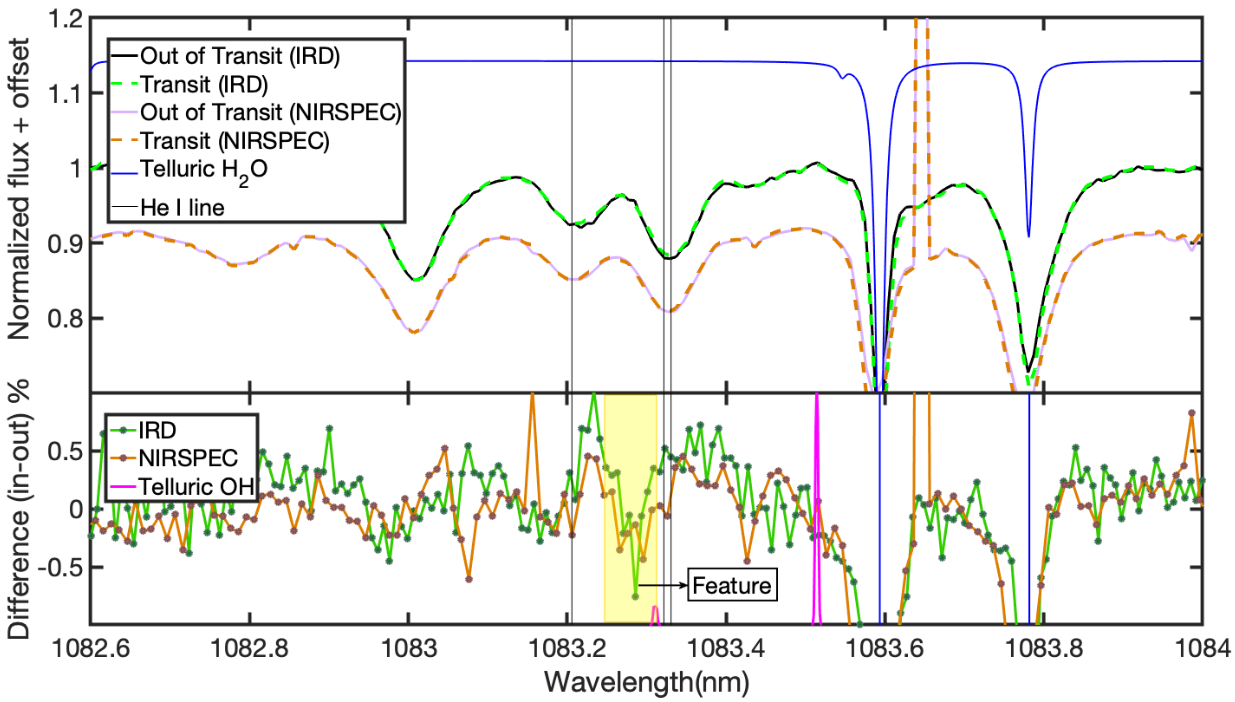

Figure 3.1: **Top**: Spectra of AU Mic in the vicinity of the He I lines (vertical black lines) obtained in and out of the transit of "b" by IRD (green and black) and NIRSPEC (orange and violet). Predicted telluric H_2O(blue) and OH (magenta) lines are from Breckinridge & Hall (1973) and Noll et al. (2012); Jones et al. (2013), respectively. **Bottom**: The corresponding difference spectra (in-out) in percentage. The yellow-shaded region shows the ~ 0.1 nm-wide feature. This is Figure 2 in Hirano et al. (2020b).

The unresolved $J = 1, 2$ doublet and the bluer $J = 0$ line of neutral orthohelium are both detected (Figure 3.1). The relative equivalent widths (EWs) suggest that the doublet is saturated and that the absorption arises from a relatively small filling factor (i.e. the fractional area coverage of the active regions) on the star (Andretta et al. 2017). The total EW (107 mÅ) is small for the star's X-ray activity with $L_X/L_{bol} = -2.82$, (Plavchan et al. 2009), possibly because emission partially fills in the line (Smith 2016).

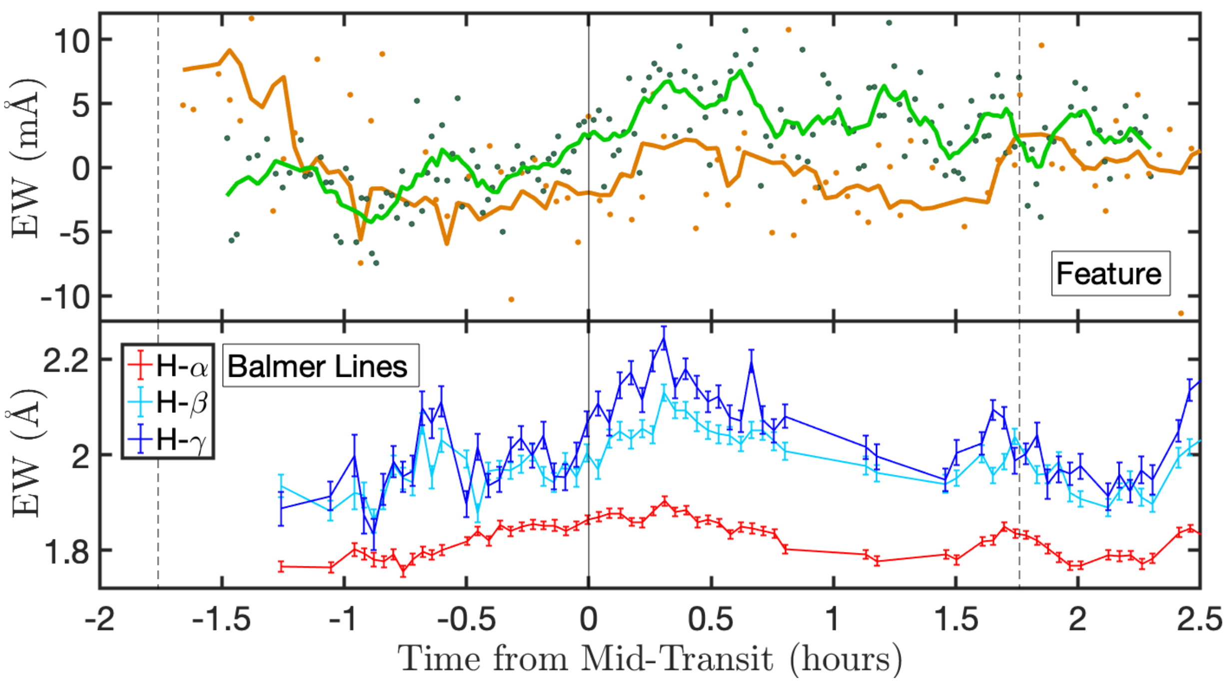

Figure 3.2: Top: Strength of the feature between 1083.225 and 1083.325 nm vs. time as measured in IRD (green) and NIRSPEC (orange) spectra. The solid lines represent 7-point, first-order Savitzky-Golay filtered versions. Bottom: EW of hydrogen Balmer lines: H-α (red), H-β (aqua) and H-γ (blue) as measured in SNIFS spectra. In both panels a positive value represents increasing emission. This is Figure 3 in Hirano et al. (2020b).

We used the transit ephemeris and duration from Plavchan et al. (2020) to sum subsets of spectra inside and outside of the transit. Individual IRD spectra were adjusted to account for the varying Doppler shift of the planet ($\pm 5\,\mathrm{km\,s^{-1}}$). Due to the lower resolution, this correction was unnecessary for the NIRSPEC spectra. A comparison of the summed spectra taken during transit and post-egress indicate no transit-related absorption at the wavelength of the strong doublet (Figure 3.1). To limit the presence of any planet-associated absorption, we assumed a Gaussian profile with thermal broadening of 1000-30000 K gas for the IRD data. We adopted an RMS value of 1.2% (as the standard deviation in our analysis) of the IRD difference spectrum for a 10 Å region in the vicinity of the line (1082-1083 nm). A similar model was implemented on NIRSPEC data. We used a simple 3-parameter (depth, line position and line width) Gaussian model to fit the feature we see in the difference spectra. We performed a χ^2 analysis to estimate the parameters. The line position was constrained to be within ± 2 nm from the doublet positions and the other two parameters were set to vary freely. From the estimated parameters, we limit the EW of any planet-associated signal to 4.4 and 3.7 mÅ (99% confidence) from the IRD spectra and NIRSPEC spectra, respectively.

A ~ 0.1 nm-wide feature about 0.05 nm blue-ward of the doublet center is apparent in both the IRD and NIRSPEC spectra (Figure 3.1). Since it appears in both independent data sets, it is not an artifact of the instrument or reduction routine. Such a feature could be Doppler-shifted absorption in a gaseous tail moving relative to the star at $\approx$-15 km s^{-1}, but it could also be a systematic, i.e.: (a) telluric variation over the transit/airmass; (b) a residual from changing Doppler shift of the stellar He I line over a few hours; (c) planetary occultation of active regions of the star responsible for the He I signal; (d) changing of the stellar line shape due to active regions appearing or disappearing from the stellar limb; and (e) changes in the stellar line due to activity. We consider (a) unlikely; there are no known H_2O lines in the vicinity (Figure 3.1). A weak OH line coincides with the feature but should have been subtracted by the rapid beam switching during the

NIRSPEC observations and other, stronger OH lines do not produce artifacts. We rule out (b) by simulating the effect, i.e., dividing the out-of-transit spectrum by a second out-of-transit spectrum that is Doppler shifted by the barycenter change of 440 m s^{-1} over the observation interval and finding negligible difference. We rule out (c) because we see no significant variation in the in-transit signal when binned into four intervals during the transit as the active regions cannot be present in all four bins. We consider (d) to be unlikely because the rotation period (4.86 days) is long compared to the observation interval.

Explanation (e) remains viable because our Balmer line series measurements with SNIFS show multiple rapid rises and slower (hour-timescale) declines consistent with flaring (Figure 3.2). Flaring could produce He I emission which is blue-shifted due to plasma motion (note that 15 $\mathrm{km\,s^{-1}}$ is twice the rotational velocity of the star). The strength of the feature in IRD spectra is significantly correlated with the Hα EW from SNIFS spectra (Spearman rank $\rho = 0.24$ and $p = 1.9 \times 10^{-3}$; Pearson's $R = 0.26$ with $p = 5.0 \times 10^{-4}$), supporting this scenario. NIRSPEC derived values are not correlated (Spearman rank $\rho = -0.03$ and $p = 0.80$; Pearson's $R = 0.07$ with $p = 0.53$), possibly due to lower instrument resolution and an early decline seen in the NIRSPEC but not the IRD data (Figure 3.2).

3.1.2 GJ 9827 system

The stellar He I lines are contaminated with a telluric sky OH emission line (Figure 3.3). Hence we used the airmass correction (Kawauchi et al. 2018) followed by `SYSREM` iterations (Tamuz et al. 2005; Birkby et al. 2013). We ran the `SYSREM` algorithm for 5 iterations.

The results are shown in Figure 3.4. As the `SYSREM` does not differentiate between the telluric features and any excess absorption from planets, we stopped after the 1st iteration and used the residuals for the search of planetary signals. We did not want to loose the planetary signal, if present in an attempt to remove the telluric features. Nevertheless, we show the residues after 1st, 2nd and 5th iterations of `SYSREM` in the Figure 3.4.

The residues after 1st iteration of `SYSREM` are transferred to the stellar rest frame accounting for system's absolute RV (31.9 km/s; Sperauskas et al. 2016) and the observation night's barycentric velocities. Individual transit frames are then accounted for the Doppler shift variation induced by the planet's transit, thereby shifting the residuals to the planet's rest frame (see Figure 3.4). Then the transit frames of planet GJ 9827b and GJ 9827d are median-combined individually to create the master in transit frame for each planet respectively. The rest of the out of transit frames are median combined to create the master out of transit frame. The flux residues of both the planets along with the flux residual ratio (in/out - 1) are plotted in Figures 3.5 and 3.6.

The telluric features are significantly removed from the flux (see Figure 3.4) after the first iteration of `SYSREM` algorithm. The flux ratio of the residues does not show any planet related absorption in both the planets (see bottom panels of Figures 3.5 and 3.6). To confirm this non-detection, we plotted the temporal variation of the equivalent width (EW) from 1083.18 nm to 1083.40 nm across the night. The temporal variation seen in the Figure 3.7, shows that there is no planet-related He I absorption in both the planets. The significant decrease in the EW at the end of the observation is probably due to the low elevation of the target and the arrival of morning twilight.

To limit any planet-related absorption, we ran a simple χ^2 analysis. We considered

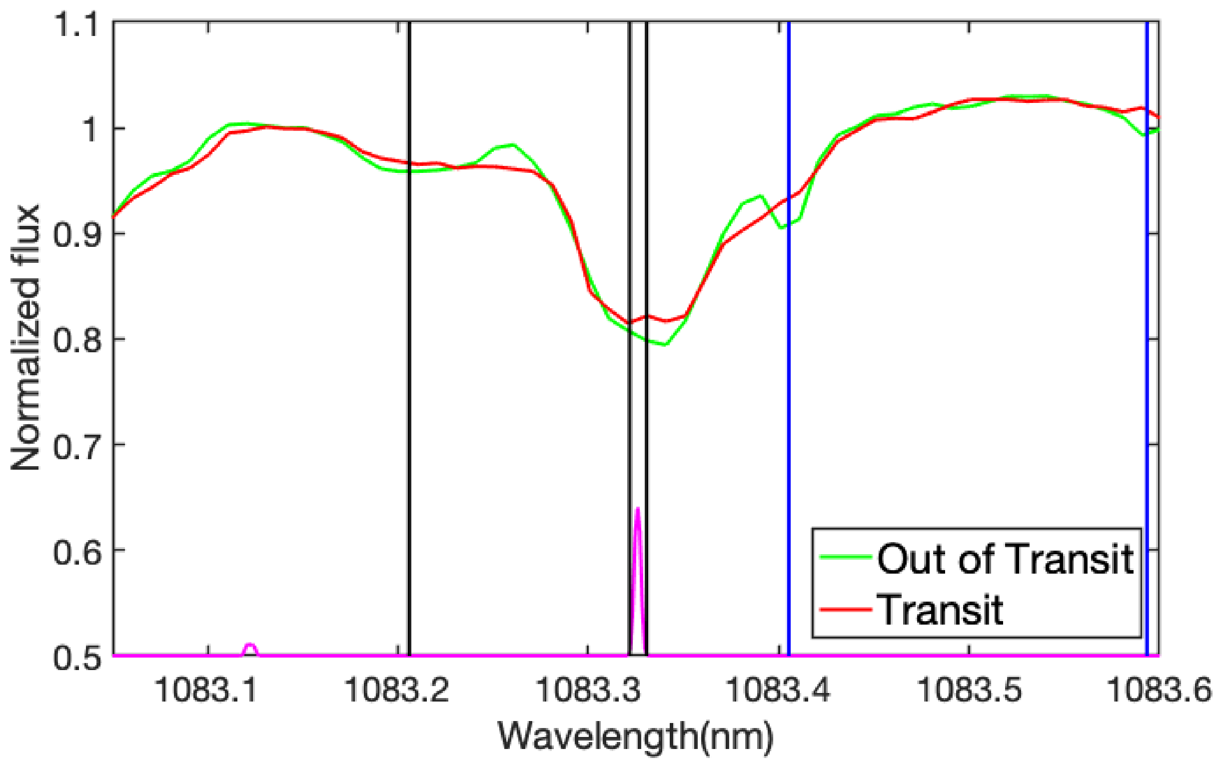

Figure 3.3: Telluric contamination in the spectra during the transit of GJ 9827b. The telluric positions of OH emission lines (magenta) and H_2O absorption lines (blue) are computed from Breckinridge & Hall (1973), Noll et al. (2012) and Jones et al. (2013). The black vertical lines mark the He I line positions.

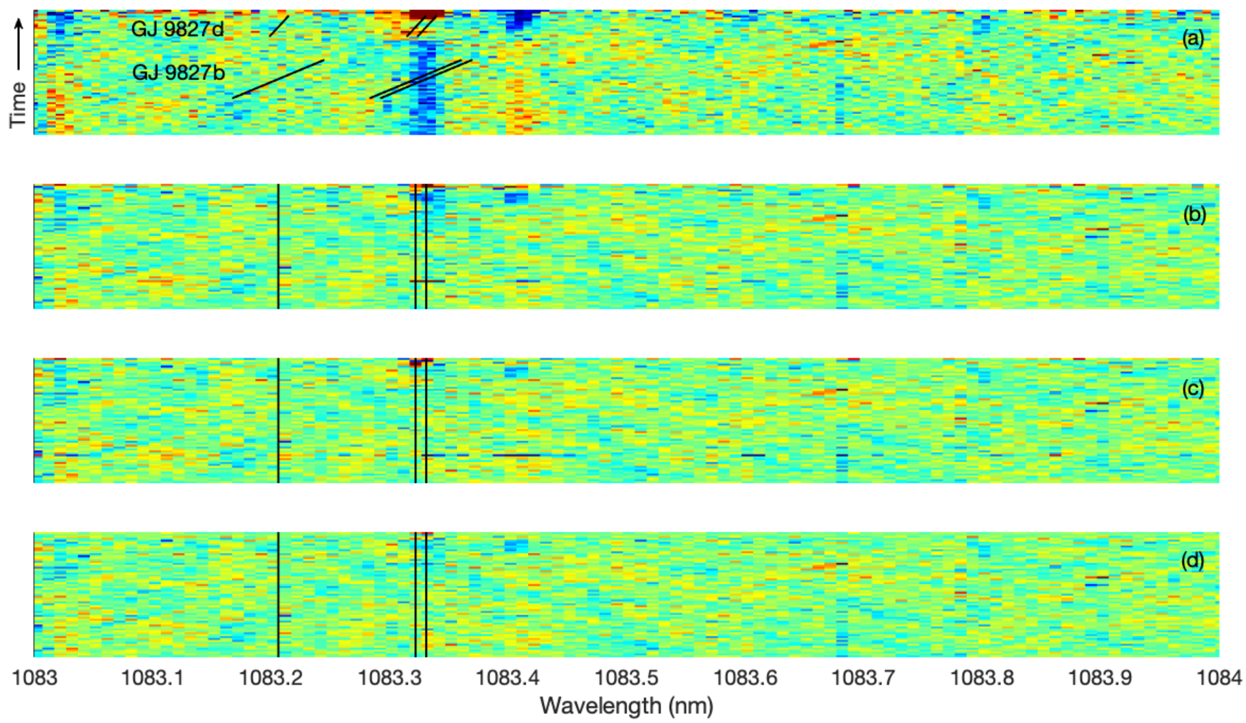

Figure 3.4: Implementation of SYSREM algorithm to correct for the telluric contamination in GJ 9827. The panel (a) shows the input to SYSREM algorithm in observer's rest frame. The black lines correspond to expected position of planetary signals, if any. The residue after 1st iteration of SYSREM , in the planet's rest frame is shown (b). The panels (c) and (d) show the residues after 2nd and 5th iterations of SYSREM respectively.

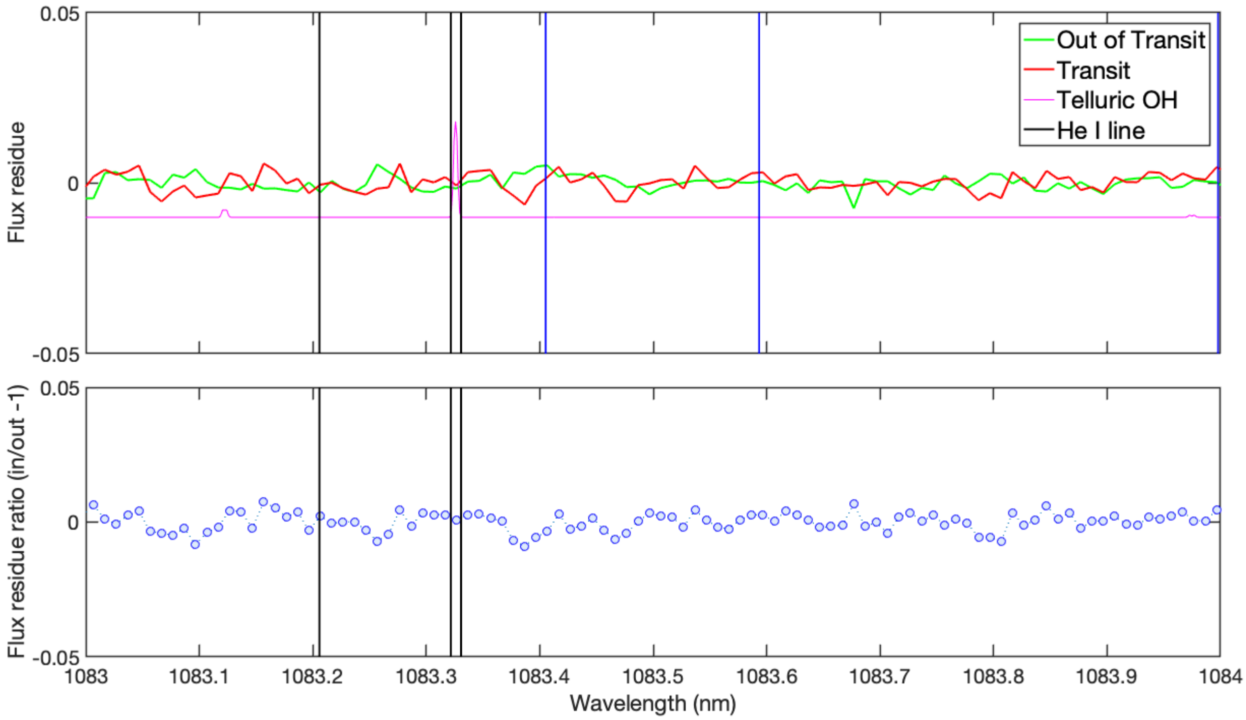

Figure 3.5: **Top**: Residual spectra of GJ 9827b after one iteration of `SYSREM` algorithm. The telluric positions of OH emission lines (magenta) and H_2O absorption lines (blue) are computed from Breckinridge & Hall (1973), Noll et al. (2012) and Jones et al. (2013). **Bottom**: The flux residual ratio (in/out - 1) of GJ 9827b. No planet related absorption is visibly seen.

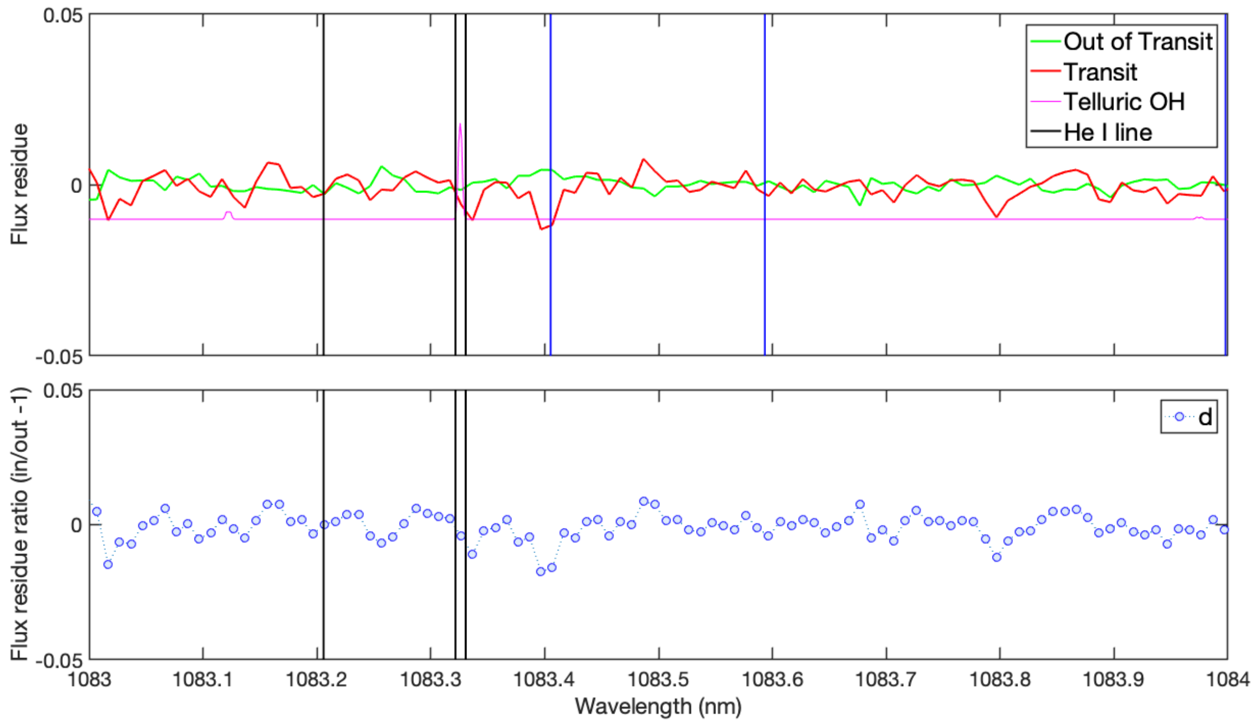

Figure 3.6: **Top**: Residual spectra of GJ 9827d after one iteration of `SYSREM` algorithm. The telluric positions of OH emission lines (magenta) and H_2O absorption lines (blue) are computed from Breckinridge & Hall (1973), Noll et al. (2012) and Jones et al. (2013). **Bottom**: The flux residual ratio of GJ 9827d. No planet related absorption signature is visibly seen.

Gaussian profile with thermal broadening up to 30000 K gas and RMS value of 1% as the standard deviation was taken from the flux ratio spectra for a region of 10 Å in the vicinity of the line (1084-1085 nm). This yielded an upper limit of 13.5101 mÅ for the planet GJ 9827b and 15.6374 mÅ for the planet GJ 9827d at 99% confidence.

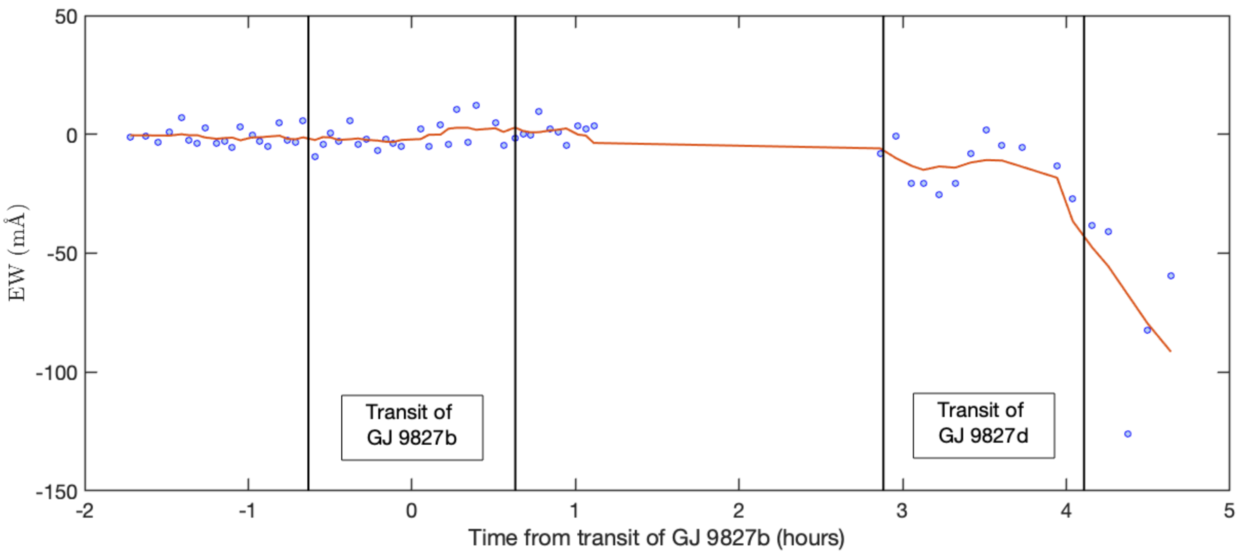

Figure 3.7: Temporal variation of flux ratio EW in the vicinity of the He I triplet. A 7-point first order Savitzky-Golay filter (red) is plotted along the raw data (blue). The beginning and end of GJ 9827b and GJ 9827d transits are marked by black vertical lines.

3.1.3 TRAPPIST-1 system

Each spectrum is transferred to the stellar rest frame by correcting for the barycentric velocity and absolute radial velocity (RV) of the system. Individual IRD and HPF spectra were adjusted to account for the Doppler shift variation of the planet, thereby shifting them to the planet's rest frame. During the transit of planet 'b', the master in-transit spectra was obtained by median-combining the 6+6 (from 2 transits; 2018 and 2020) individual transit spectra from IRD and HPF separately. For producing the master out-of-transit IRD spectra, we excluded the first 7 frames after the IRD 2018 transit data. This was done to eliminate the possibility of contaminating the out-of-transit spectra from a possible evaporating tail from the planet. We used all the available out-of-transit frames to create the median-combined HPF master out-of-transit frame.

In the case of planets 'e' and 'f' transits captured by IRD in 2018, there could be possible overlap of the tail from planet 'e' transit frames into the planet 'f' transit frames, as the transit of planet 'f' followed the transit of planet 'e' immediately. The median combined master in-transit and out-of-transit spectra for planet 'b' (from IRD and HPF), 'e' (from IRD) and 'f' (from IRD) are plotted in Figure 3.8.

The stellar He I lines are not detected in IRD and HPF spectra. The absence of stellar line is likely due to the low effective temperature of TRAPPIST-1 and not due to a line fill-in from collisional excitation (Fuhrmeister et al. 2019). From the IRD spectra of planet 'b', we see a ~ 0.02 nm wide feature about 0.03 nm blueward of the doublet center. This feature could originate from gaseous absorption from a Doppler-shifted tail moving relative to the star at -7 km/s. To confirm that the feature originated during transit, we compared the strength of in-transit spectra with the same number of randomly sampled out-of-transit spectra. We performed this comparison for 1000 iterations. We find that the mean-strength of feature during transit (EW=5.17 ± 3.18 mÅ) is higher than that of the random sampled out-of-transit spectra (EW=0.11 ± 3.79 mÅ) in the IRD data. We do not detect such a blueward feature in the HPF spectra.

The feature is not due to telluric variations over transit/airmass as we do not have any telluric H_2O and OH line in the vicinity (see Figure 3.8). It could also have its origin from planetary occultation of active regions of the star responsible for the He I signal.

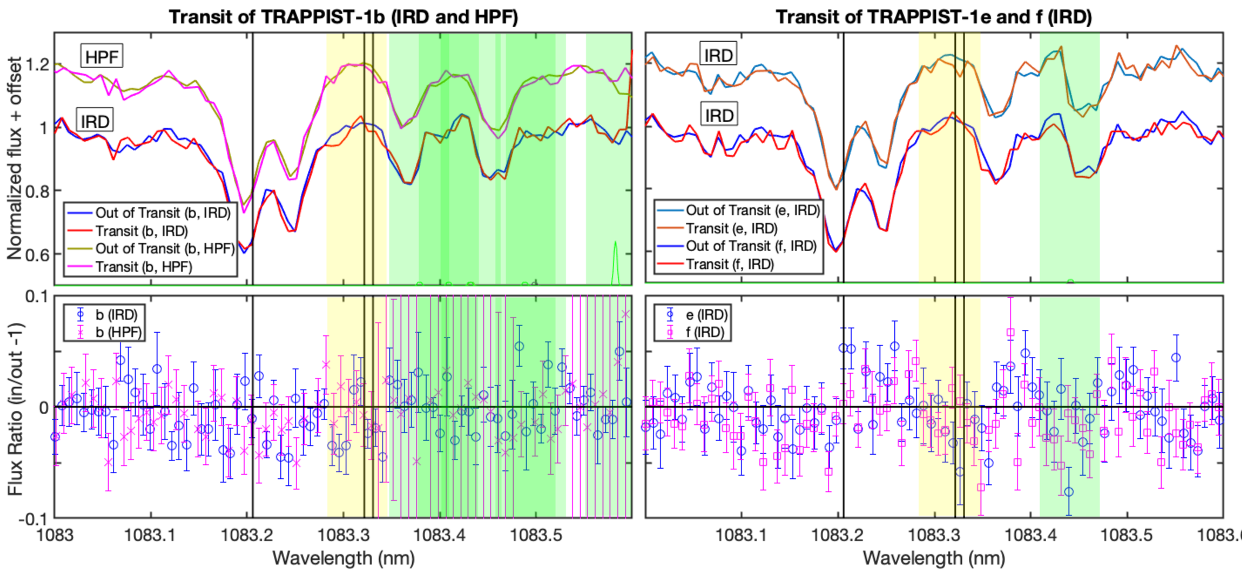

Figure 3.8: Transmission spectra of TRAPPIST-1 planets. The top panels show the spectra of TRAPPIST-1 in the vicinity of He I triplet lines (solid black vertical lines). **Top left**: The in- and out-of-transit spectra of planet 'b' from both IRD (red and blue) and HPF (magenta and light green) are shown. **Top right**: In- and out-of-transit spectra during the transit of planet 'e' (orange and light blue) and during the transit of planet 'f' (red and blue) from IRD (Hirano et al. 2020a). **Bottom**: Their respective flux ratios (in/out - 1). The green-shaded region corresponds to the OH-emission line position computed from Jones et al. (2013). The computed known telluric H_2O positions from Breckinridge & Hall (1973) do not fall in the vicinity of Helium lines. The yellow-shaded region is our "*region of interest*".

However, we rule this out because we could reproduce the feature from two transits of planet 'b' through IRD (see Figure 3.9: top panel) and since the rotational period of the star is different from the orbital period of planet 'b'. Changes of the stellar line shape due to active regions appearing or disappearing from the stellar limb could also mimic this signal. But we consider this to be unlikely as the rotation period (3.295 days; Vida et al. 2017) is long compared to the transit duration.

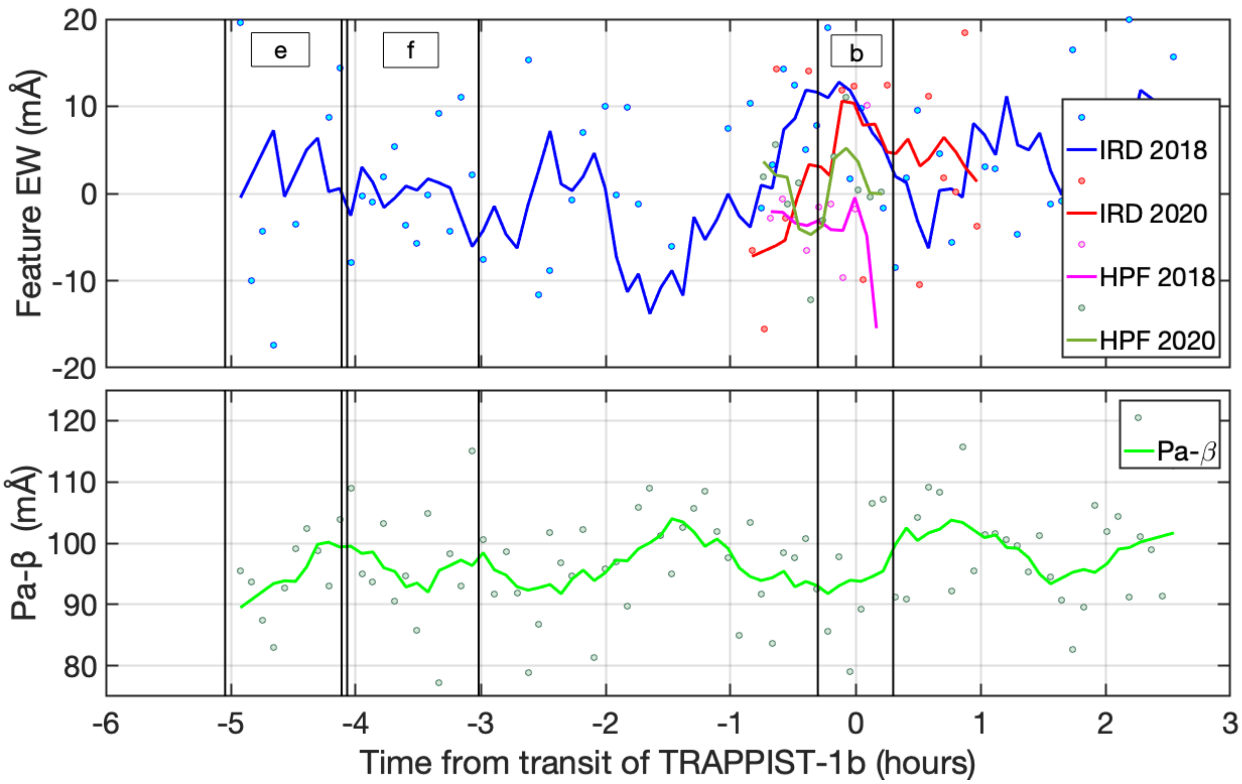

Figure 3.9: **Top**: Strength of the feature between 1083.285 and 1083.34 nm ("region of interest") vs. time as measured in IRD (UT 30 August 2018 - blue and UT 2020 September 16 - red) and HPF (UT 2018 October 2 - magenta and UT 2020 September 5 - green) spectra. The solid lines represent 7-point, first-order Savitzky-Golay filtered versions. **Bottom**: EW of Hydrogen Paschen beta line as measured in IRD spectra on UT 30 August 2018. Both panels correlates negatively.

The spectra of TRAPPIST-1e does show some variation in their in-transit spectra when compared to their out-of-transit spectra (see right panels of Figure 3.8). By performing a similar random sampling analysis, we find that the mean-strength of the feature during the transit of TRAPPIST-1e (EW=5.41±2.28 mÅ) is higher than the mean-strength during the out-of-transit (EW=0.11±3.79 mÅ). However, such features are not seen during the transit of TRAPPIST-1f in the IRD spectra.

TRAPPIST-1 being a fainter target, causes excess scatter in the RV data (Hirano et al. 2020a). Also, TRAPPIST-1 is prone to have strong activity on its surface (Wheatley et al. 2017; Vida et al. 2017) and with lack of simultaneous measurement of activity indicators (e.g., Hydrogen Balmer lines) we could not rule not the feature's origin from stellar activity. Since the stellar He I lines are not detected, we chose a $\sim$ 0.55 Åwide region as a "region of interest" around the strongest doublet (1083.285-1083.34 nm in vacuum) to compute upper limits. To limit any planet-related He I absorption in planet 'b', 'e' and 'f', we modeled a simple Gaussian profile with a thermal broadening of 1000-30000 K. Using a 3-parameters (depth, line position and line width) Gaussian, we try to fit the features we see in the "region of interest". We performed a Markow chain Monte Carlo (MCMC) analysis with 3-parameters and 30000 crawlers. The line position was constrained to be within ± 2 nm from the expected position of the doublet and the other two parameters were set to vary freely. From this analysis, we limit the Equivalent Width (EW) of any planet-associated absorption to 7.754 mÅ, 10.458 mÅ, and 4.143 mÅ for planets 'b', 'e', and 'f', respectively, from the IRD data, and 3.467 mÅ for planet 'b' from HPF data at 95% confidence.

The Paschen beta (Pa-β) emission line is considered as a tracer for outflow activity in T-Tauri stars (Whelan et al. 2004). In our observations, Pa-β line is seen as an absorption line. The temporal variation of the strength of "region of interest" with the Pa-β from the IRD 2018 spectra is shown in Figure 3.9. The EW of the feature in "region of interest" from IRD does not correlate with the Pa-β line. This insignificant negative correlation coefficient (Pearson's R = -0.0438 and p = 0.6905; Spearman Rank ρ = -0.0171 and p = 0.8766) could have arisen from the large scatter in the spectra, emphasizing the need for more observations. The 7-point, first-order Savitzky-Golay filtered version correlates with a better significance (Pearson's R = -0.2403 and p = 0.0267; Spearman Rank ρ = -0.2275 and p = 0.0365). The HPF data too shows a negative correlation with the Pa-β feature (Pearson's R = -0.4097 and p = 0:2108; Spearman Rank ρ = -0.4727 and p = 0:1456). The Savitzky-Golay filtered version of HPF He I data does not correlate with the Pa-β feature, possibly due to the absence of post-egress data from the transit night. The Pa-β line from 2020 IRD observations were redundant as they were contaminated by a telluric OH-emission line. The HPF Pa-β data was not usable as it lacked the pre-ingress and post-egress data, making it impossible to extract any useful information in the temporal analysis. The comparison of Pa-β feature from 2018 IRD data with the data from other instruments and various nights is not ideal as several factors (eg., spectral resolution, seeing, airmass, etc.) affect the quality of this comparison. However, this comparison is made to just visualize the trend and not to extract any quantitative information to characterize the planet's atmosphere.

The results of the analysis presented in this sub-section have been published in the following paper. Given below are the details:

Title: Non-detection of Helium in the upper atmospheres of TRAPPIST-1b, e and f

Authors: Vigneshwaran Krishnamurthy, Teruyuki Hirano + 33

Journal: the Astronomical Journal (Vigneshwaran Krishnamurthy et al 2021 AJ 162 82).

3.1.4 TOI-1235b

The TOI-1235b's 26 transit frames are median-combined to form the master in-transit spectra. The remaining 26 frames, when there is no transit of TOI-1235b are median-combined to form the master out-of-transit spectra. The transmission spectra of TOI-1235b is plotted in Figure 3.10. We can clearly see that there is no visible planetary absorption signal.

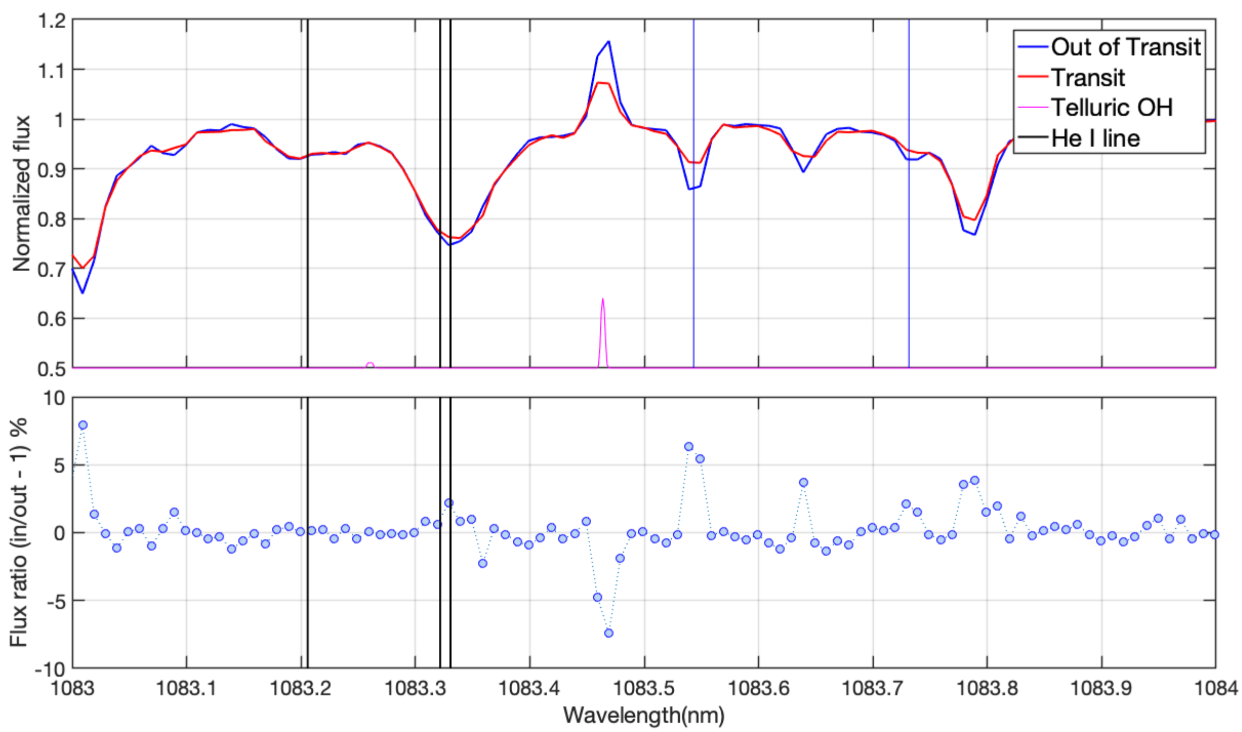

Figure 3.10: **Top**: The in- and out-of-transit spectra of TOI-1235b. The black vertical lines mark the He I triplet positions. The telluric positions of OH emission lines (magenta) and H_2O absorption lines (blue) are computed from Breckinridge & Hall (1973), Noll et al. (2012) and Jones et al. (2013). **Bottom**: The flux ratio (in/out - 1) in percentage of TOI-1235b. No planet related absorption is visibly seen.

The excess depth seen in lines other than the telluric lines during the out-of-transit could originate from unknown telluric water lines or from the poor observing conditions by the end of observations on UT 2021 April 09. In order to limit any planet-related absorption, we estimated the equivalent width (EW) of the stellar Helium lines across the transit night. The temporal variation is plotted in the top panels of Figure 3.11.

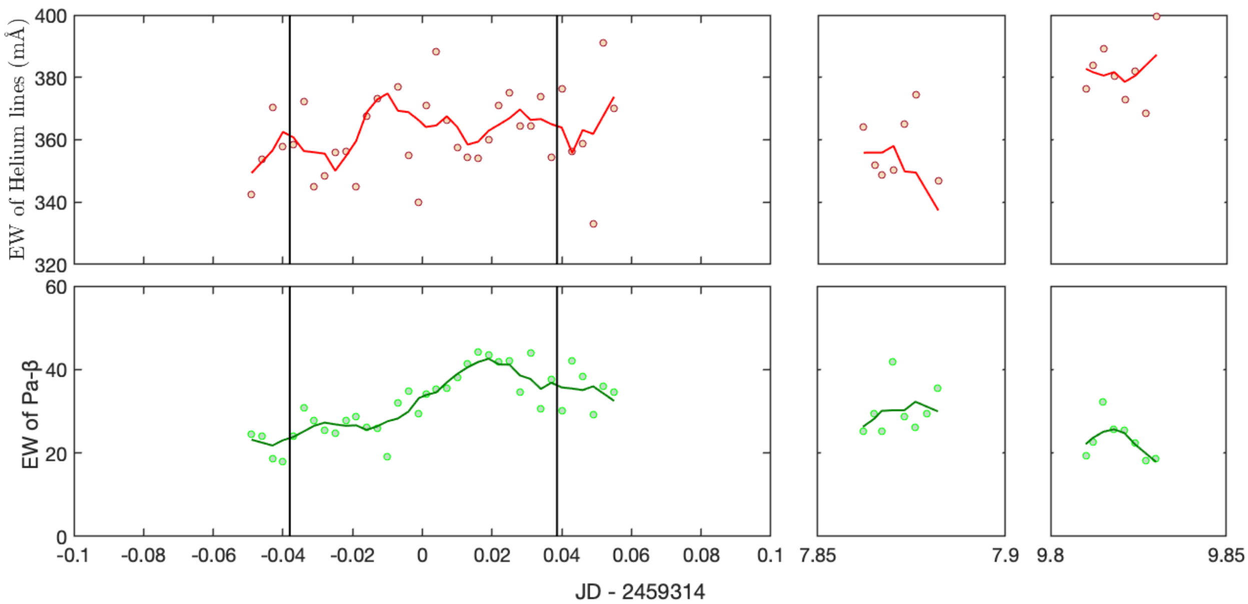

Figure 3.11: **Top**: Strength of Helium vs. time. The solid red lines represent 7-point, first-order Savitzky-Golay filtered versions. **Bottom**: EW of Hydrogen Paschen beta line seen in absorption.

The EW of Paschen beta line seen in absorption is plotted in the bottom panels of Figure 3.11. There is no strong correlation between the He I triplet lines and the Pa-β line. The raw data yields a Pearson's correlation of R = 0.0263 and a p-value of 0.8789; and Spearman's ρ = 0.1308 and p-value = 0.4457. However, there is a hint of negative correlation between helium and Pa-β outside the transit, giving us a Pearson's correlation of R = -0.4886 and p-value of 0.0548; and Spearman's ρ = -0.4882 and p-value of 0.0572. Comparing He I lines with Pa-β during the transit yields us a weakly insignificant correlation (Pearson's R = -0.0865 and p-value = 0.6744). This anomaly seen during the transit indicate there is some unknown process, and begs the need for more observations. Following a similar χ^2 analysis performed for other planets, we limit any planet related absorption to be less than 1.42 mÅ at 95% confidence.

3.1.5 HIP 67522b

The transit of this hot Jupiter was not fully captured on UT 16 April 2021. HIP 67522b's orbital phase from ϕ=-0.004 to ϕ=0.03 was captured on that night, with ϕ=-0.004 to ϕ=0.014 were during the transit (about last 65% of the transit). Several additional spectra of HIP 67522 when there was no transit of the planet HIP 67522b were obtained on successive nights. We used all these out-of-transit spectra to remove any systematic error in our analysis. There were no known telluric positions in the vicinity that interfered in our He I analysis, hence we did not run the `SYSREM` iterations. The median combined in-transit and out-of-transit spectra are shown in the Figure 3.12.

We detect a decrease in flux, during the transit of HIP 67522b at the He I positions. The OH emission line and H_2O absorption line redward of 1083.4 nm might interfere with the redward tail of He I absorption but not the core of this absorption feature. The weak emission line at 1083.22 nm might interfere with the planetary signal, however its intensity is expected to be weak. To confirm if this feature is actually of planetary origin, we plotted the temporal variation of He I from 1083.18 nm and only until 1083.4 nm to neglect the effect of the OH emission line (see top panel in Figure 3.13). The drastic increase in the EW during transit (from 350 mÅ to a peak of ~500 mÅ) strongly indicate the feature originated during transit.

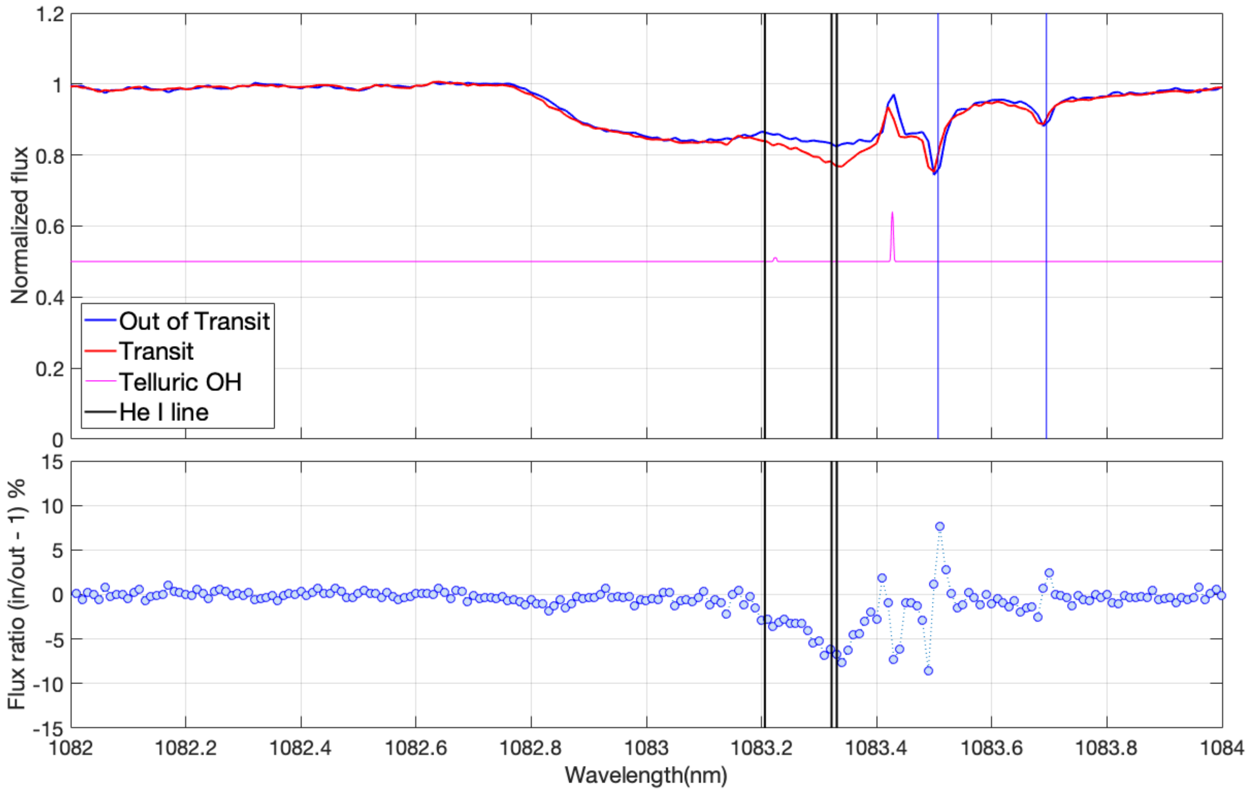

Figure 3.12: **Top**: The in- and out-of-transit spectra of HIP-67522b. The black vertical lines mark the He I triplet positions. The telluric positions of OH emission lines (magenta) and H_2O absorption lines (blue) are computed from Breckinridge & Hall (1973), Noll et al. (2012) and Jones et al. (2013). **Bottom**: The flux ratio (in/out - 1) in percentage of HIP-67522b. Clear He I absorption is seen in the doublet positions.

The invariance in Paschen-beta (Pa-β) temporal plot indicates that there was no strong stellar activity during this phase of observation (see Figure 3.13). All the analysis is carried out on the planet rest frame. After accounting for the planet induced Doppler-shift, we shift the spectra from the stellar rest frame (Figure 3.14) to the planet rest frame (Figure 3.15). Using simple six parameter χ^2 analysis, we fit a model for the excess absorption of He I in HIP 67522b. During this analysis, we mask the telluric OH and H_2O dominated regions (1083.4 - 1083.7 nm). Our best fit model estimates an excess

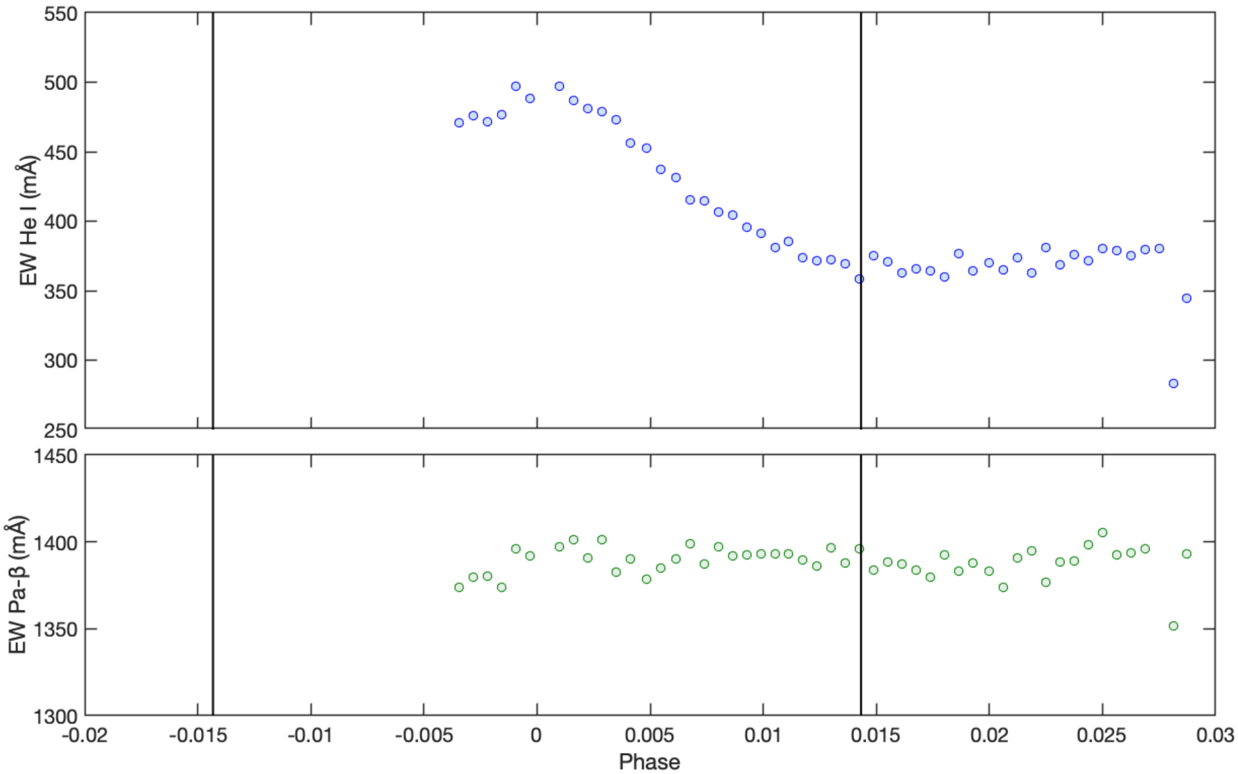

Figure 3.13: **Top**: Strength of Helium (between 1083.18 - 1083.4 nm) vs. time. **Bottom**: EW of Hydrogen Paschen beta line seen in absorption.

absorption of 7.1 ± 0.7 %. (Figure 3.16).

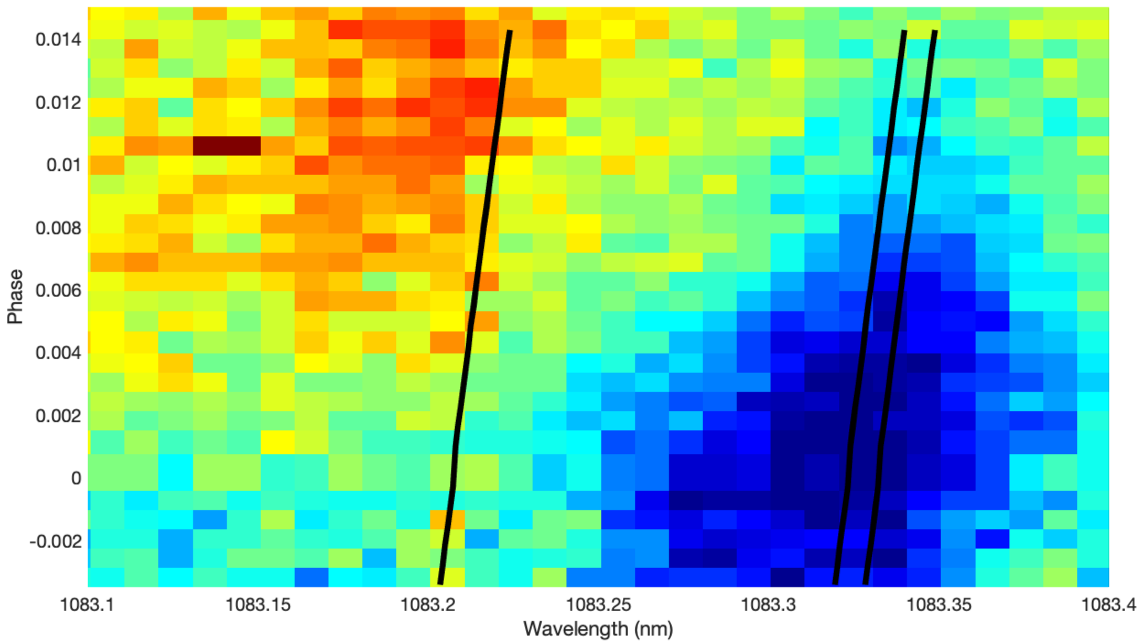

Figure 3.14: Temporal variation map in the stellar rest frame. Black lines mark the position of He I triplet lines. Blue indicates lower and red indicates higher flux values.

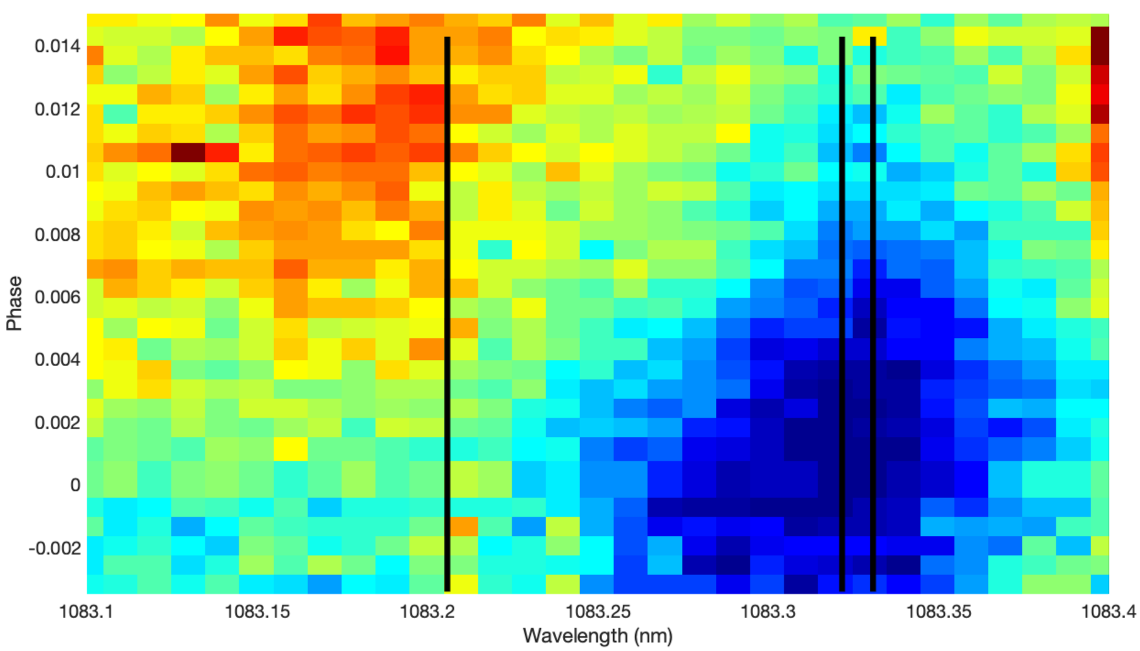

Figure 3.15: Temporal variation map in the planet rest frame. Black vertical lines mark the position of He I triplet lines. Blue indicates lower and red indicates higher flux values.

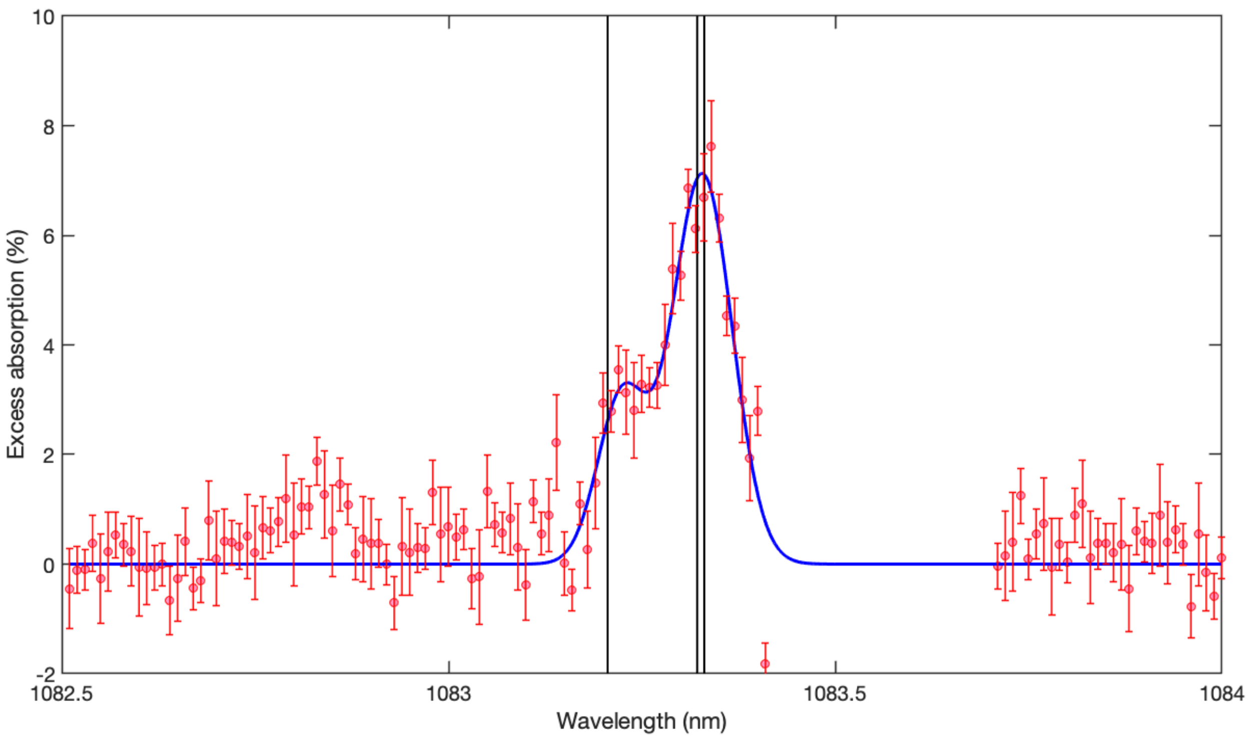

Figure 3.16: Excess absorption of He I in HIP 67522b. The best fit model (blue) estimates an excess absorption of 7.1 ± 0.7 %. The telluric affected region (1083.4 - 1083.7 nm) are masked.

This detection makes HIP 67522b the youngest hot Jupiter to have its evaporating atmosphere detected. It is also the largest He I absorption depth seen in a G-dwarf planet.

3.2 Analysis of transmission spectra: NIR O_2 at 1.27 μm

The TRAPPIST-1 planets provide an interesting opportunity of probing the NIR O_2 feature at 1.27 μm with planets 'e' and 'f' in the habitable zone of the star (Luger et al.

2017; Grimm et al. 2018). Since Earth's telluric O_2 dominates this spectral regime (see Figure 3.17) and the expected lower atmosphere transit depths are in the order of 0.01%, we planned to use the cross-correlation analysis to search for the feature. Although it is impossible to retrieve the abundances of a species from the cross-correlation analysis, detection of a species is possible.

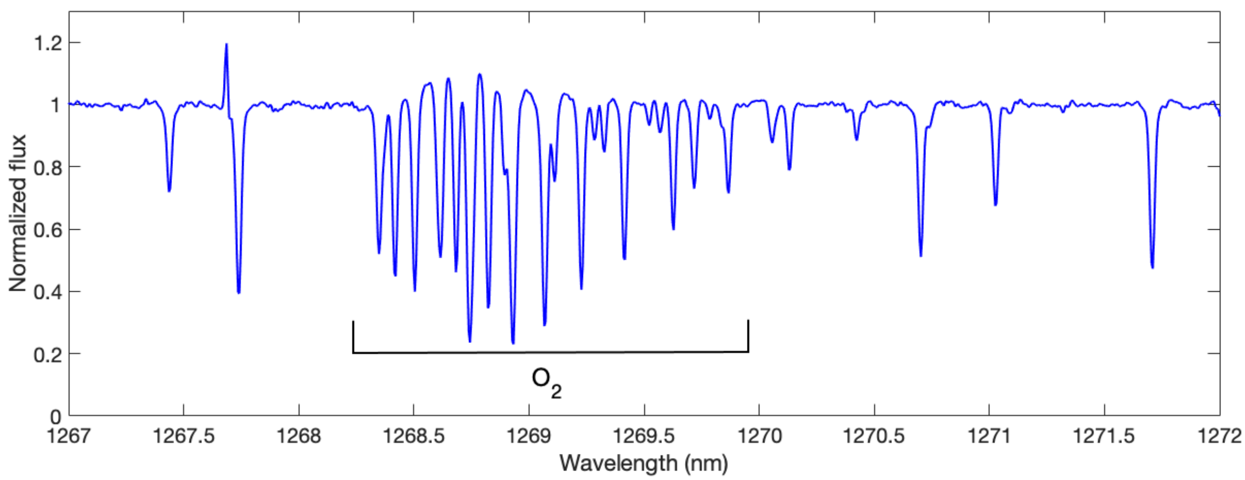

Figure 3.17: Telluric O_2 features seen during the observation of HD 195689, a A0-type rapid rotator. Spectra was obtained from IRD on UT 31 August 2018 (Hirano et al. 2020a).

After the telluric correction using the airmass (Kawauchi et al. 2018), we implemented the `SYSREM` iterations (Tamuz et al. 2005; Birkby et al. 2013). We ran the `SYSREM` algorithm for 20 iterations and performed the cross-correlation analysis on the residues after each iteration. Figure 3.18 shows the residues after airmass correction and `SYSREM` iterations.

For O_2 feature, we used the molecular line-list database of HITRAN (Gordon et al. 2017; Rothman et al. 2013). These were convolved with the IRD's Instrumental Profile (IP) to create the template spectra. Then it is subtracted by one to remove the continuum.

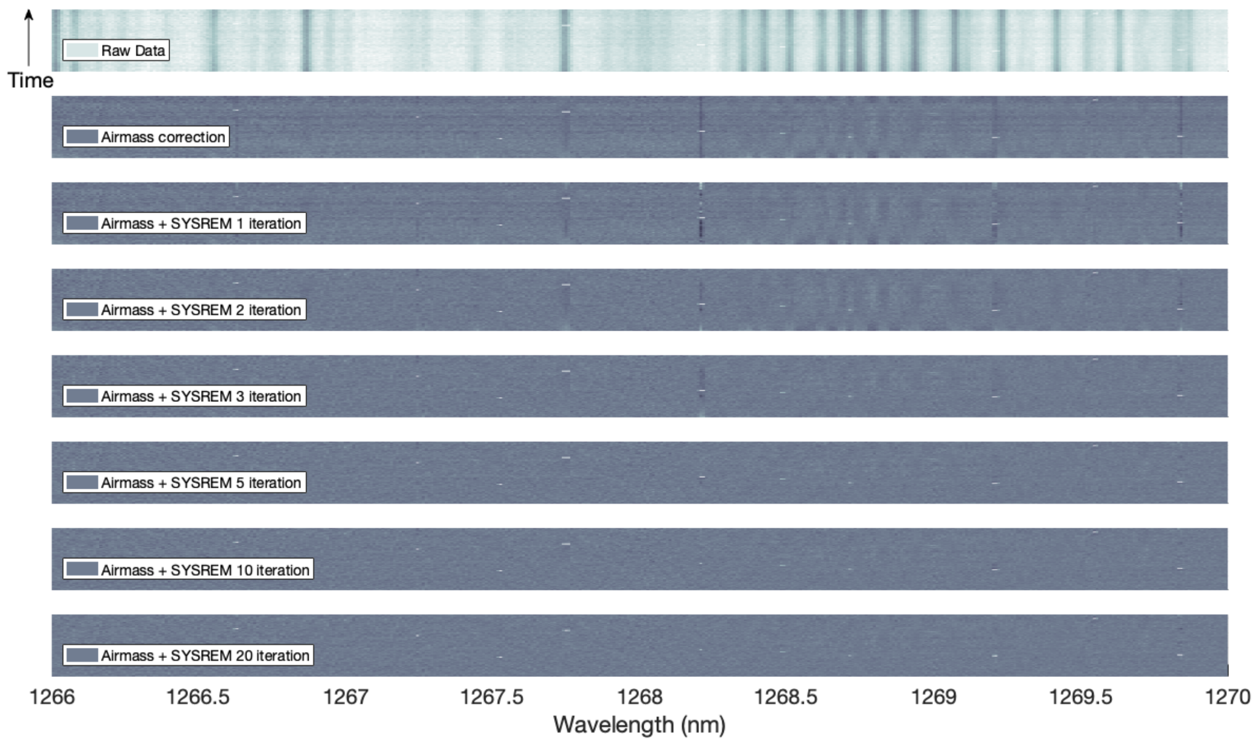

Figure 3.18: Telluric correction in the vicinity of NIR O_2 feature. The top panel shows the raw TRAPPIST-1 spectral data. The successive panels show the residue after the airmass correction (Kawauchi et al. 2018), followed by `SYSREM` iterations (Tamuz et al. 2005; Birkby et al. 2013).

We used the 2018 transit data (Hirano et al. 2020a) and 2020 transit data of TRAPPIST-1 planets for our analysis. Each normalized IRD frame have been corrected for the telluric lines in the observer's rest frame. Then the continuum is removed by subtracting one. Now the IRD spectra is ready for cross-correlation analysis.

The cross-correlation function (CCF) is calculated by the formula,

$$CCF(v) = \int_{\lambda_1}^{\lambda_2} F\left(\lambda - \frac{v}{c}\lambda\right) \times G\left(\lambda\right)\, d\lambda \tag{3.1}$$

where, F(λ) is the individual TRAPPIST-1 spectra and G(λ) is the O_2 template spectra.

v is the radial velocity and c is the speed of light. This CCF is computed in the wavelength interval of $\lambda_1 = 1260\,\mathrm{nm}$ to $\lambda_2 = 1275\,\mathrm{nm}$ and a velocity range of -150 $\mathrm{km\,s^{-1}}$ to +150 $\mathrm{km\,s^{-1}}$ in the observer's rest frame (a.k.a., telluric rest frame).

The computed CCFs are transferred to the stellar rest frame, accounting for the absolute RV and barycentric velocities. The transit frames are further transferred to the planet's rest frame. In the case of TRAPPIST-1b's transit frames, we used both the transits from 2018 and 2020. And for TRAPPIST-1e and TRAPPIST-1f transit frames, we used the data from 2018. Then the individual planet's in-transit CCFs are median-combined to form a master in-transit CCF map and the out-of-transit CCFs are median-combined to form a master out-of-transit CCF map. This process is done for the residues from each iteration of `SYSREM` algorithm, as the `SYSREM` process might over-correct the telluric features, removing the planetary signals, if any.

The CCF plots are plotted for all three planets after 1, 3, 4, 5, 10 and 20 `SYSREM` iterations in Figures 3.19, 3.20, 3.21, 3.22, 3.23 and 3.24 respectively.

We can see that the `SYSREM` algorithm couldn't effectively remove the telluric O_2 features in the first few iterations. This can be seen at the velocity of 52.5 $\mathrm{km\,s^{-1}}$, the telluric rest velocity in the planet's rest frame. However, by 4^{th} and 5^{th} iterations, one can see that the telluric features are completely removed (see Figure 3.21 and 3.22). The planetary signals are expected around 0 $\mathrm{km\,s^{-1}}$. The signal-to-noise ratio (SNR) is computed by estimating the standard deviation from the CCF data, ±25 km/s away from the region of expected planet signals. The computed SNR for the transit frames in the vicinity of planet rest velocity (0 km/s) for a selected number of `SYSREM` iterations are shown in Figure 3.25.

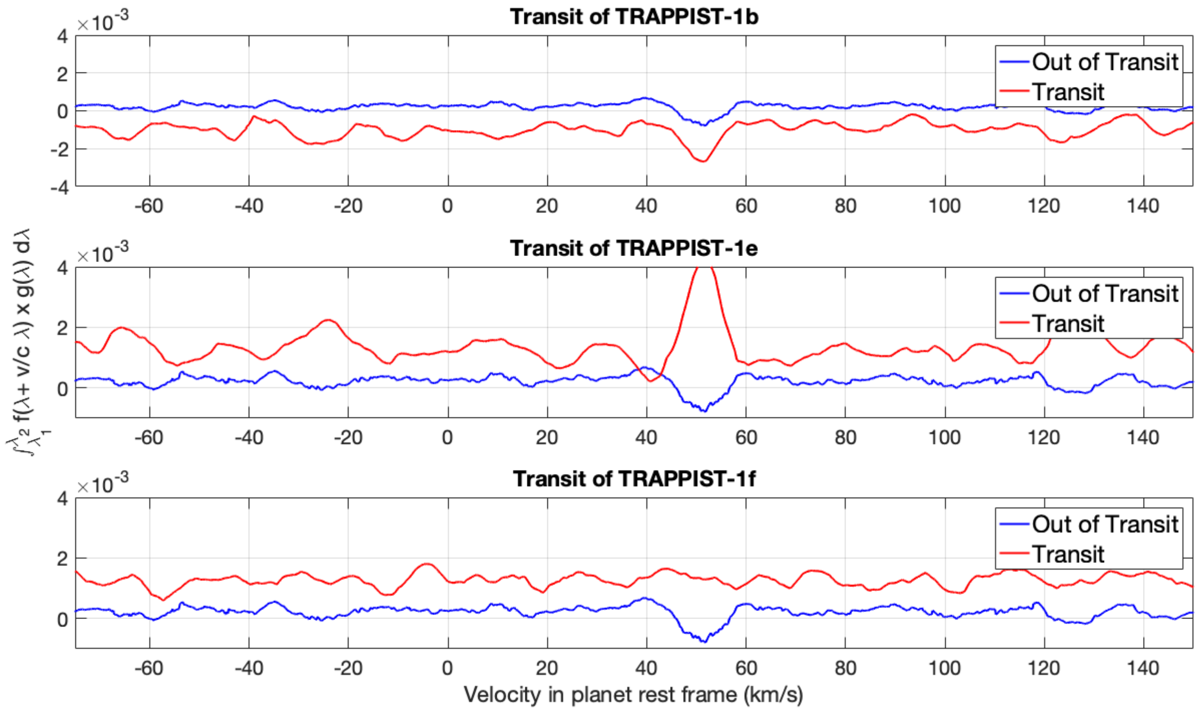

Figure 3.19: CCF plots for TRAPPIST-1 planets after SYSREM one iteration.

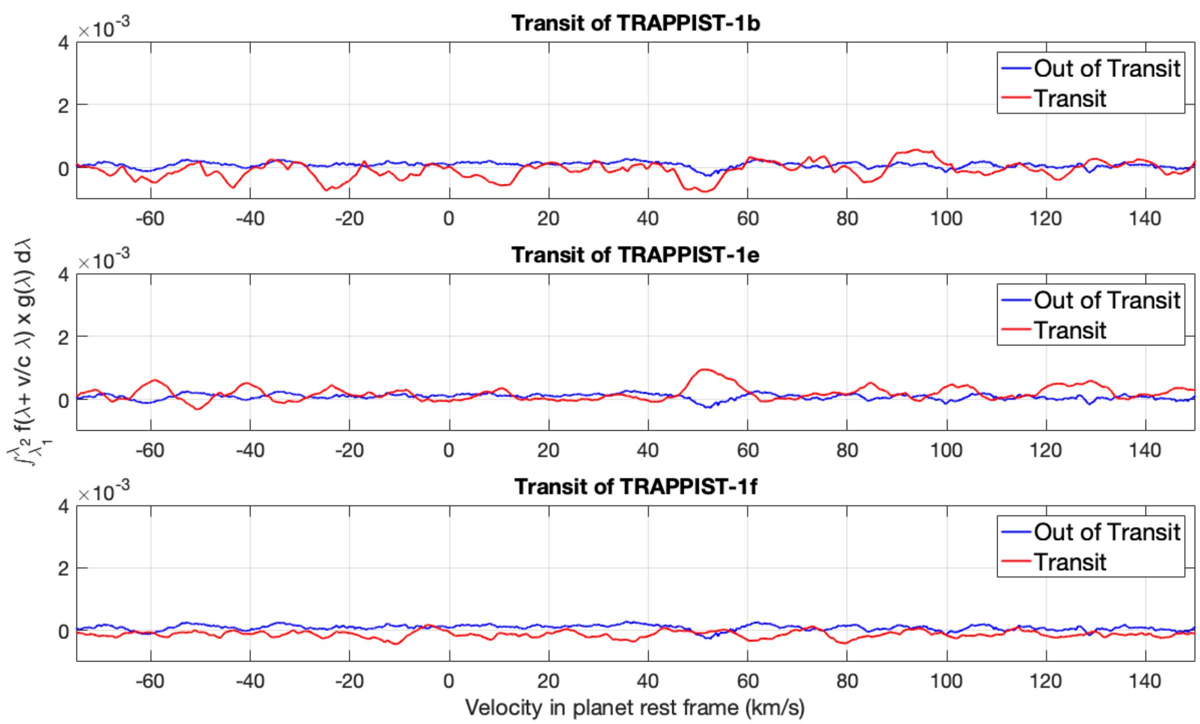

Figure 3.20: CCF plots for TRAPPIST-1 planets after SYSREM three iterations.

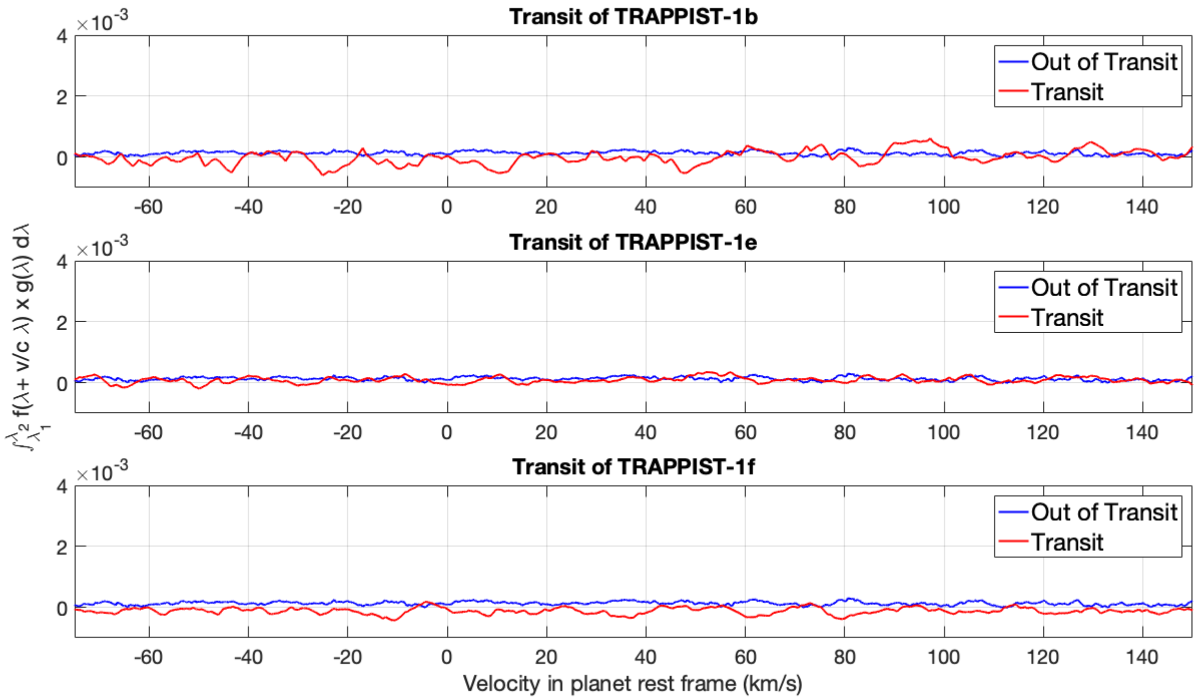

Figure 3.21: CCF plots for TRAPPIST-1 planets after SYSREM four iterations.

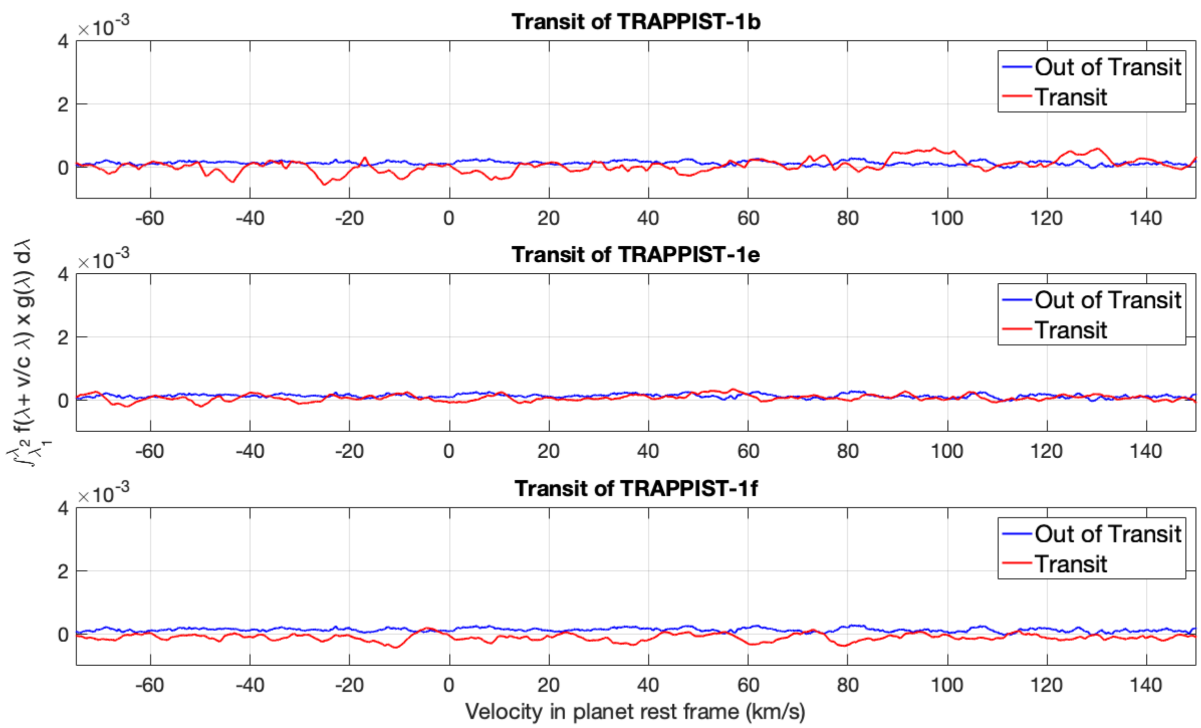

Figure 3.22: CCF plots for TRAPPIST-1 planets after SYSREM five iterations.

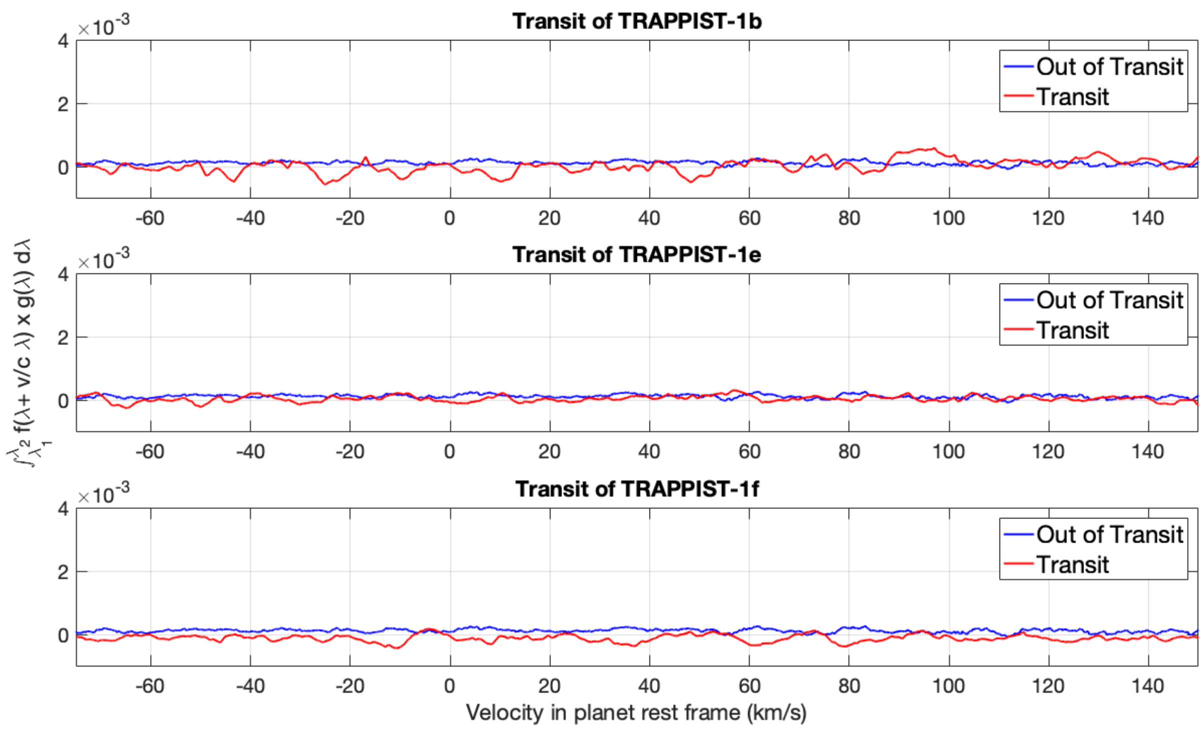

Figure 3.23: CCF plots for TRAPPIST-1 planets after `SYSREM` ten iterations.

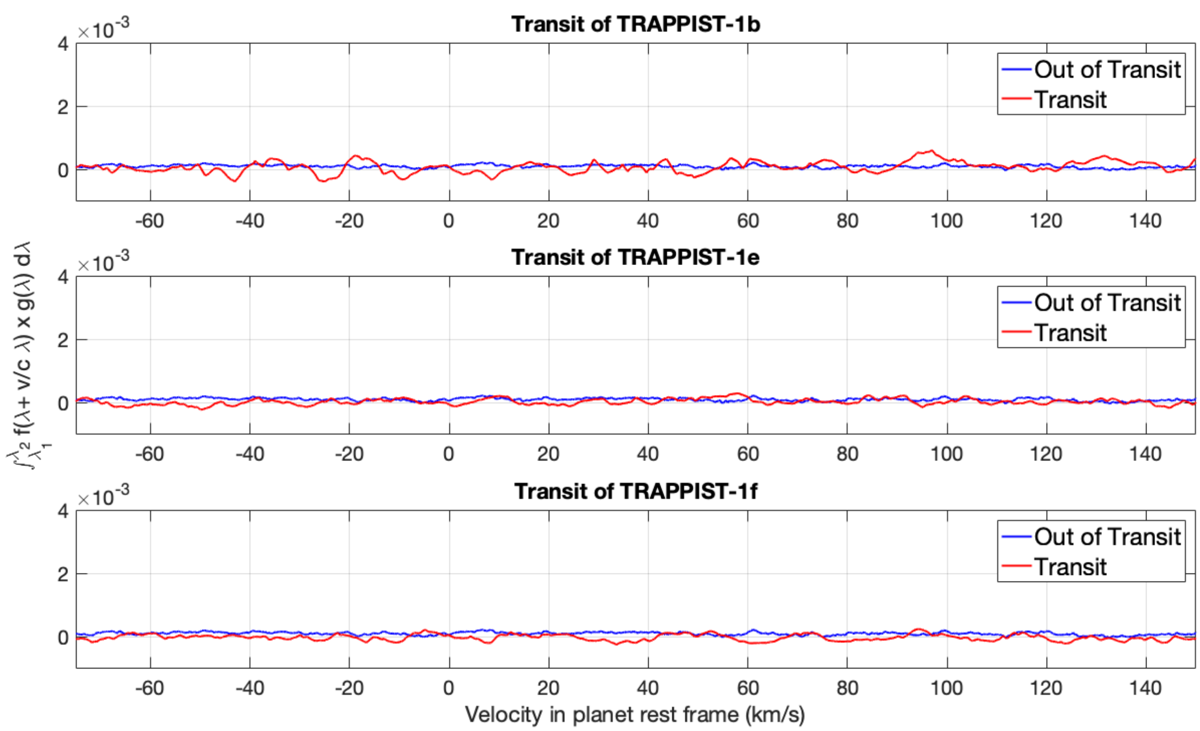

Figure 3.24: CCF plots for TRAPPIST-1 planets after `SYSREM` twenty iterations.

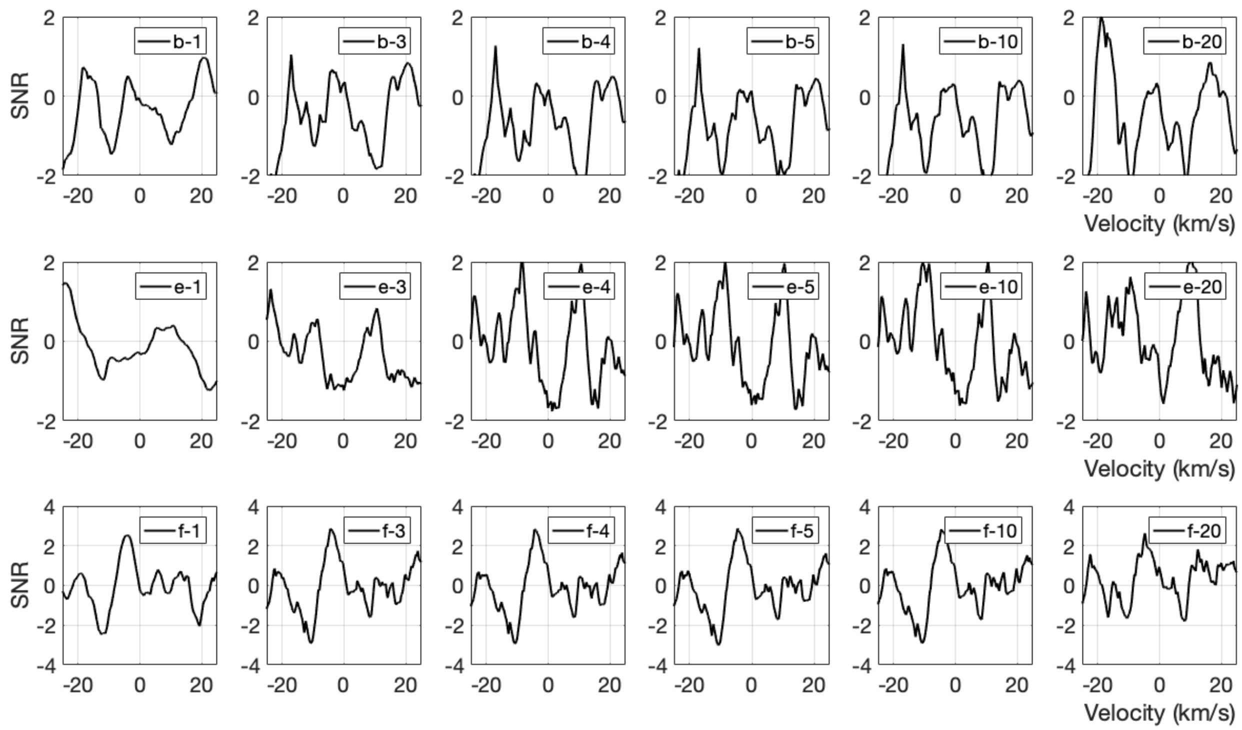

Figure 3.25: SNR variation of the CCF plots after different `SYSREM` iterations. The letter in each panel correspond to the planet (eg., 'b' corresponds to TRAPPIST-1b). The number next to the letter correspond to the number of `SYSREM` iterations.

There is no strong peak near the planet rest velocity in planets 'b' and 'e'. But there is a local maximum at ≈ -4 $\mathrm{km\,s^{-1}}$ in planet 'f' (see bottom row in Figure 3.25). This feature stays even after 20 `SYSREM` iterations. This feature could have arisen as a CCF artifact. Or this could be evaporating oxygen in a desiccated world that lost several Earth-oceans of water due to extreme radiation in the early years (Luger & Barnes 2015).

To confirm this feature, we plotted a SNR map for the residues after 5 iterations of `SYSREM` algorithm. Figure 3.26 shows the SNR map in the stellar rest frame and Figure 3.27 shows the SNR map in the planet rest frame. The variation induced by planetary Doppler-shift in these small planets are in the order of $\pm$1-2 $\mathrm{km\,s^{-1}}$, hence the difference is

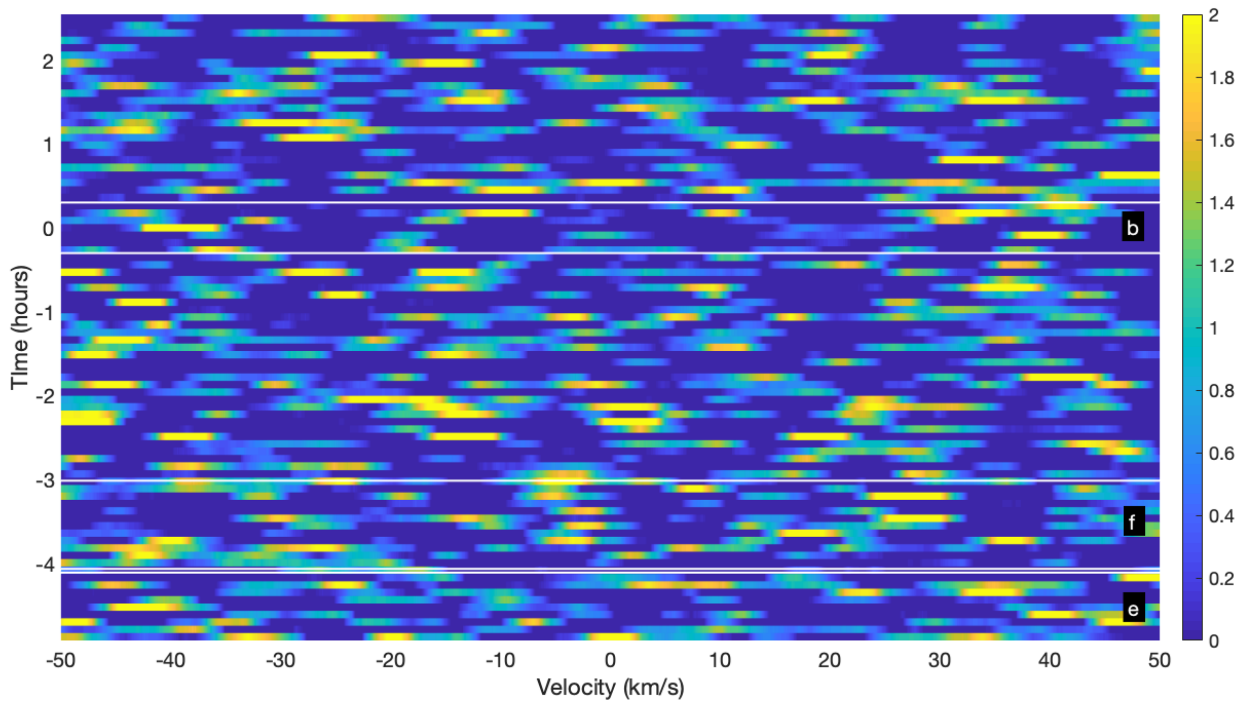

Figure 3.26: SNR map for residues after five iterations of SYSREM in stellar rest frame

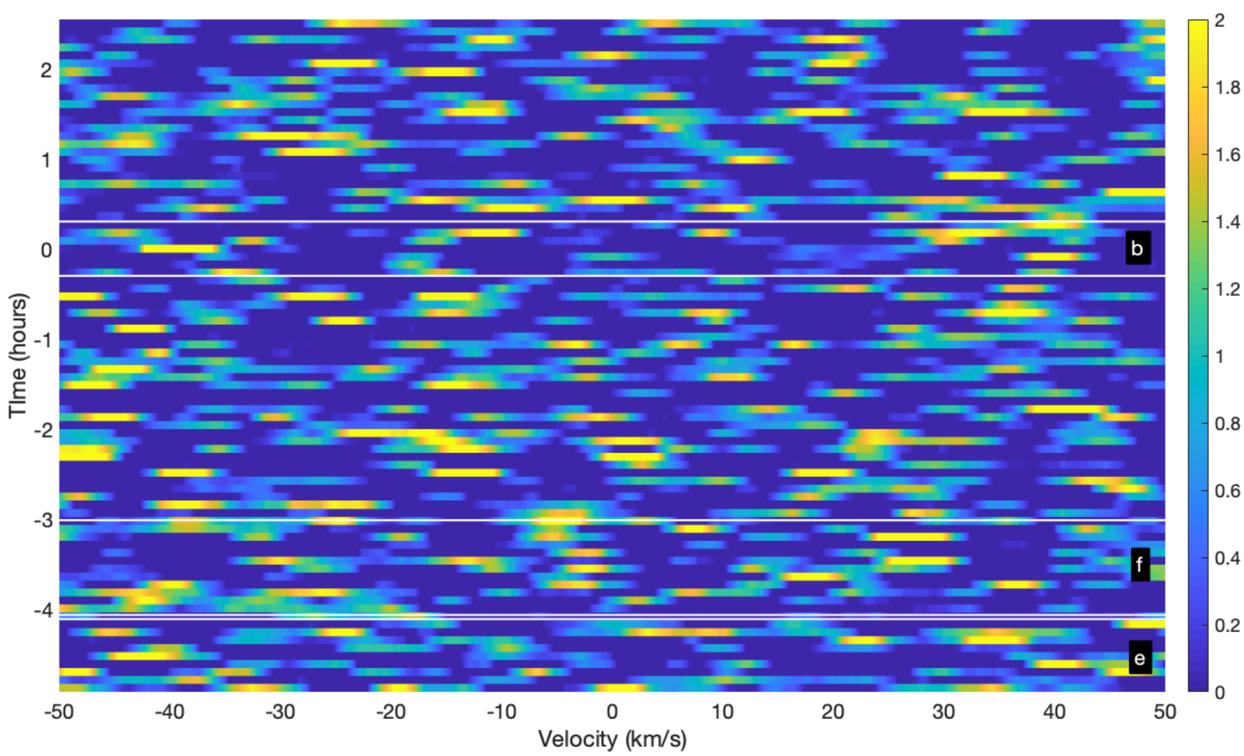

Figure 3.27: SNR map for residues after five iterations of SYSREM in planet rest frame

not apparent. One can see the SNR ~ 2 peak during the transit of planet 'f' at -4 $\mathrm{km\,s^{-1}}$ in both these plots. The significance of this detection is not very high, necessitating the need for more observations. The possibility on the origin of this marginally-detected feature is discussed in the Discussion Chapter.

3.2.1 Injection - Retrieval test

To confirm if the planetary NIR O_2 features can be detected after the telluric corrections, we performed an injection test. In this test, we artificially injected a planetary signal, 100 times the strength of 10 bar O_2 atmosphere. After injecting, we performed the same analysis and tried to retrieve back the signal. The Figure 3.28 shows the feature retrieved back in the planet's rest velocity after 5 iterations of `SYSREM` algorithm. We can see that the telluric features are removed and only the injected signal remains.

This shows us that implementing cross-correlation analysis after telluric corrections can indeed retrieve back any planetary signals from the atmospheres, if they are present.

3.3 Investigation on detectability of Oxygen from future 30m class telescope

The molecular oxygen O_2 feature at 1.27 μm provide an interesting window to probe the atmospheres of temperate and tropical planets (Kawahara et al. 2012; Meadows et al. 2018a). This marker requires hundreds to thousands of M-dwarf HZ Earth-sized planet's transit observations to confirm a 5-σ detection on a 8-10 m class telescope. This ob-

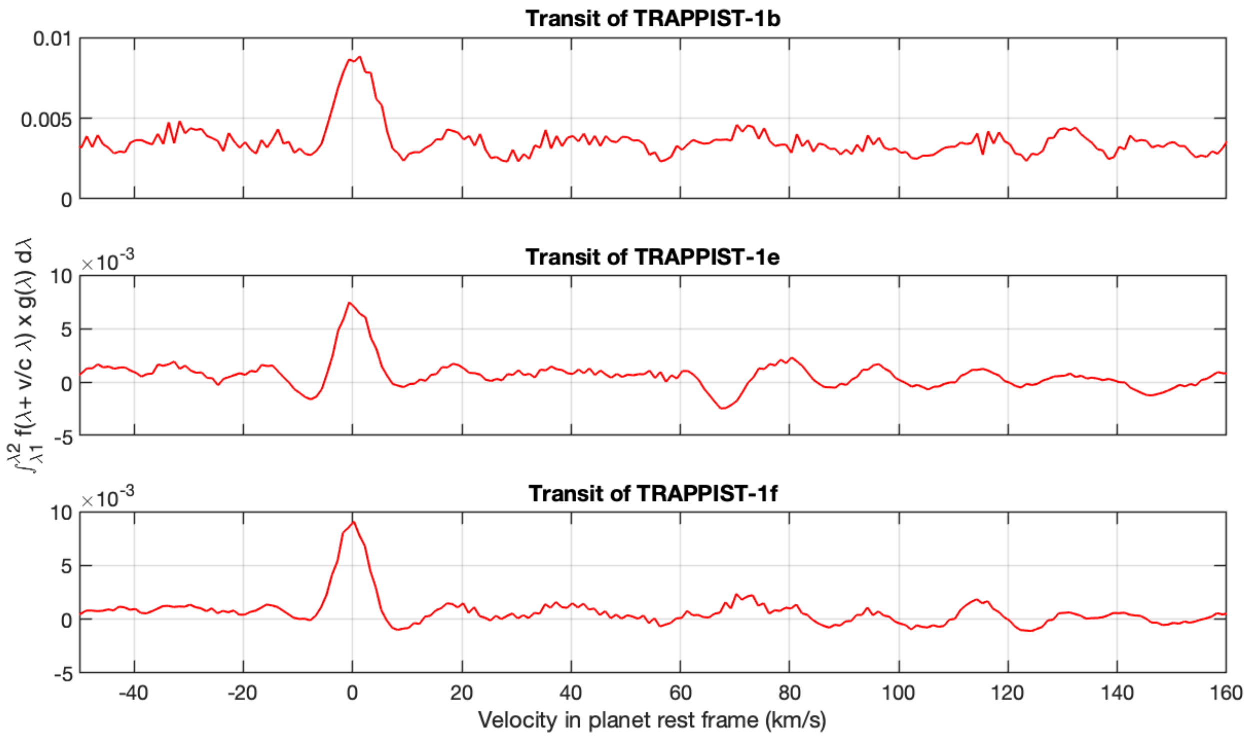

Figure 3.28: CCF plot for injection test. 100 times the strength of 10 bar O_2 atmosphere was injected and retrieved back in all three planets.

servation is cost-ineffective as the observation would last several decades (Snellen et al. 2013). The hope is even lower for hotter FGK stars, as the planets produce shallower transit depths. However there is scope for such observations in a *reasonable* observation timescale in the next-generation Extremely Large Telescopes (ELT) like the Thirty Meter Telecope (TMT) (Sanders 2013; Skidmore et al. 2015) and European-Extremely Large Telescope E-ELT (Gilmozzi & Spyromilio 2007; Tamai & Spyromilio 2014). These large telescopes will have large light gathering power and state-of-the-art high-resolution (R $\geq$ 100,000) spectrographs and detectors (Skidmore et al. 2015; Tamai & Spyromilio 2014). Few of these spectrographs like Multi-Object Diffraction-limited High-Resolution Infrared Spectrograph (MODHIS) in TMT (Mawet et al. 2019), Exo-Planet Imaging Camera and

Spectrograph (EPICS) (Kasper et al. 2010) and SIMPLE (Oliva & Origlia 2008) on the E-ELT are expected to operate in the NIR wavelengths.

The feasibility study on detecting the 1.27 μm O_2 feature for such instruments are crucial in planning the observations. Kawahara et al. (2012) presented the possibility of detecting this 1.27 μm O_2 feature from future ground-based facilities for which the detection contrast is limited by photon noise. Snellen et al. (2013) showed that it would take 4-20 years of observations for late M-dwarf HZ planets and up to 90 years of observations for early M-dwarf HZ planets to have their terrestrial Earth-level oxygen to be detected using this marker on a 39m ELT telescope with an optimistic throughput of 20%.

Here we present a feasibility study on the detectability of 1.27 μm O_2 feature in the atmospheres of TRAPPIST-1b, e and f planets (Gillon et al. 2016, 2017) from a 30m class telescope. These planets around a very small star ($0.12\,R_\odot$; Agol et al. 2021) provide the best test cases for probing their stratosphere/upper troposphere and test the capabilities of such high resolution spectrographs on a 30m class telescope. This study is different from other studies presented before (eg., Snellen et al. 2013) as it considers realistic throughput of 10%. Also we use focus on a variety of atmospheres on planets at different orbital distances (not just in the HZ) from the star. In addition, we use our IRD observation data to construct the stellar template in the analysis.

3.3.1 Specification of the telescope and spectrograph

We are considering the simulation on a 30m class telescope with a single primary mirror. The spectrograph has a resolution of R = 100,000. The telescope beam has a FWHM of 0.2 arcsec. The wavelength range of 1.25 μm to 1.3 μm was chosen in order to accommodate them in a single spectral order with a pixel scale of 0.0125 nm/pixel. The detector is assumed to have a conservative shot-noise (readout noise) of 20 e^{-}/pixel and a dark current shot-noise in the thermally excited electrons of 0.05 e^{-}/s. This future telescope is expected to have a total throughput of 10%.

3.3.2 Observation plan

The zodiacal light is the faint and diffuse radiation across the ecliptic plane originating from scattered sunlight by interplanetary dust. The brightness of the zodiacal light decreases with distance from the Sun, with a notable increase at opposition due to backscattered sunlight (Villanueva et al. 2018). Hence choosing an optimized time to observe the target helps to reduce the background noise. Observing TRAPPIST-1 during the most optimized time gives the Zodiacal noise of Level 2 (Kwon et al. 2004; Leinert et al. 1998). The stellar and planetary parameters of TRAPPIST-1b, e and f are shown in the Table 2.3.

Each transit visit consists of obtaining n number of transit spectra and $2 \times n$ number of out-of-transit spectra. The integration time was set to a constant 300 seconds. This gives the number of spectra per transit visit for TRAPPIST-1b as 21 (7 transit + 14 out-of-transit), for TRAPPIST-1e as 33 (11 + 22) and for TRAPPIST-1f as 36 (12 + 24).

3.3.3 Injecting atmospheres and noise

We are considering two types of atmospheres with two different composition each. And all these cases are evaluated for 3 levels of pressure. All the different cases are shown in the Table 3.1 below.

Table 3.1:: Different cases of atmospheres

Type	Continuum process	Pressure	Case Name
Desiccated O_2	Present	1 bar	Case 1
Desiccated O_2	Present	10 bar	Case 2
Desiccated O_2	Present	100 bar	Case 3
Desiccated O_2	Absent	1 bar	Case 4
Desiccated O_2	Absent	10 bar	Case 5
Desiccated O_2	Absent	100 bar	Case 6
Earth-like	Present	1 bar	Case 7
Earth-like	Present	10 bar	Case 8
Earth-like	Present	100 bar	Case 9
Earth-like	Absent	1 bar	Case 10
Earth-like	Absent	10 bar	Case 11
Earth-like	Absent	100 bar	Case 12

The first type of atmosphere is desiccated O_2 . The atmosphere is totally filled with pure O_2 . This type of atmosphere can be created from the photolysis of huge quantities of water (equivalent to several Earth oceans; Luger & Barnes 2015). The second type of atmosphere is same as Earth, with similar compositions and temperature-pressure (T-P) profile (Figure 3.29). This T-P profile is also used for O_2 atmospheres. Both these types of atmospheres are reciprocated with and without the continuum processes. Here we have considered two continuum processes: Collision-Induced Absorption (CIA) for all the species present in the atmosphere and Rayleigh scattering. Refraction effects were not modeled as they negligibly impact the transmission spectrum, even for an Earth–M5V system (Bétrémieux & Kaltenegger 2014). Clouds and hazes are also not modeled in these simulations. And all the types of atmospheres are simulated for different surface pressure levels: 1 bar, 10 bar and 100 bar.

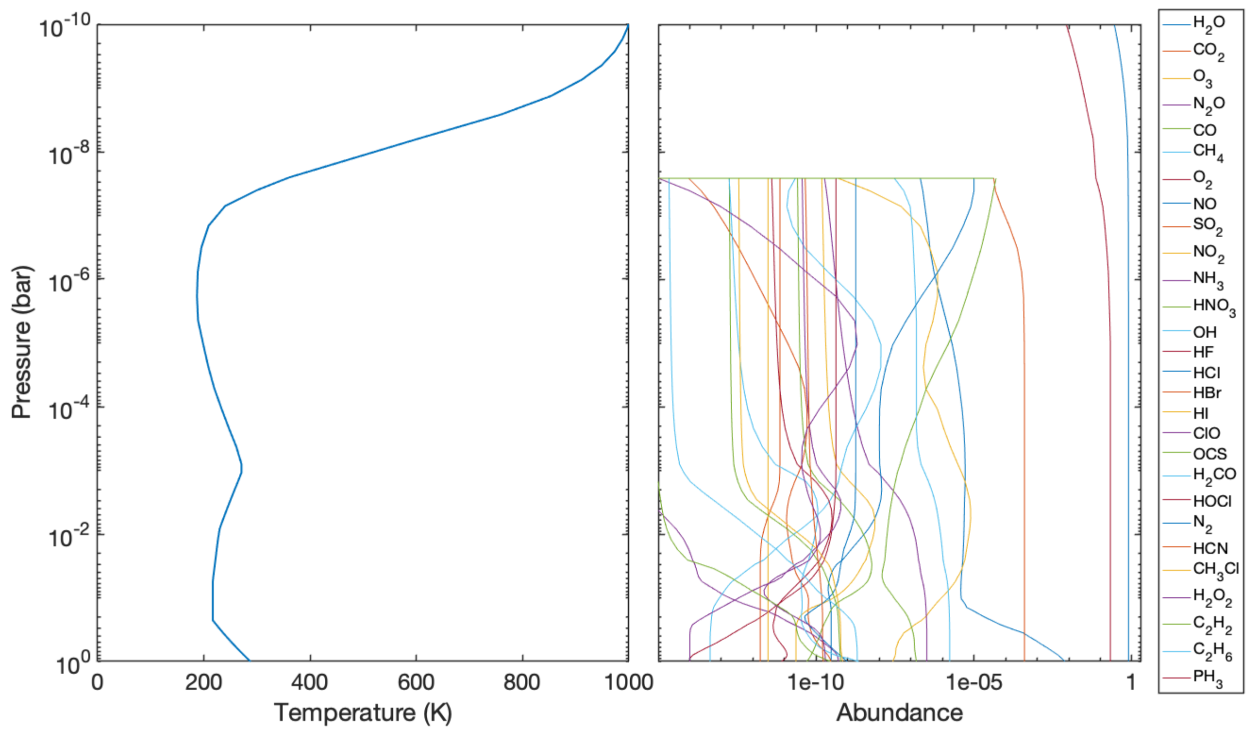

Figure 3.29: **Left**: Temperature-Pressure profile adopted in the analysis for 1 bar atmosphere. **Right**: The abundances of different species in an Earth-like atmosphere (1 bar).

An example of atmosphere with and without the continuum opacities is shown in Figure 3.30. The planet's transmission spectra is created by assuming 60 layers from surface pressure to 10^{-10} bar of 1D plane-parallel hydrostatic atmosphere. The inverted T-P profile is adopted from Robinson & Catling (2014). The species opacities were calculated from HITRAN2016 line-list (Gordon et al. 2017) and continuum opacities (CIA and

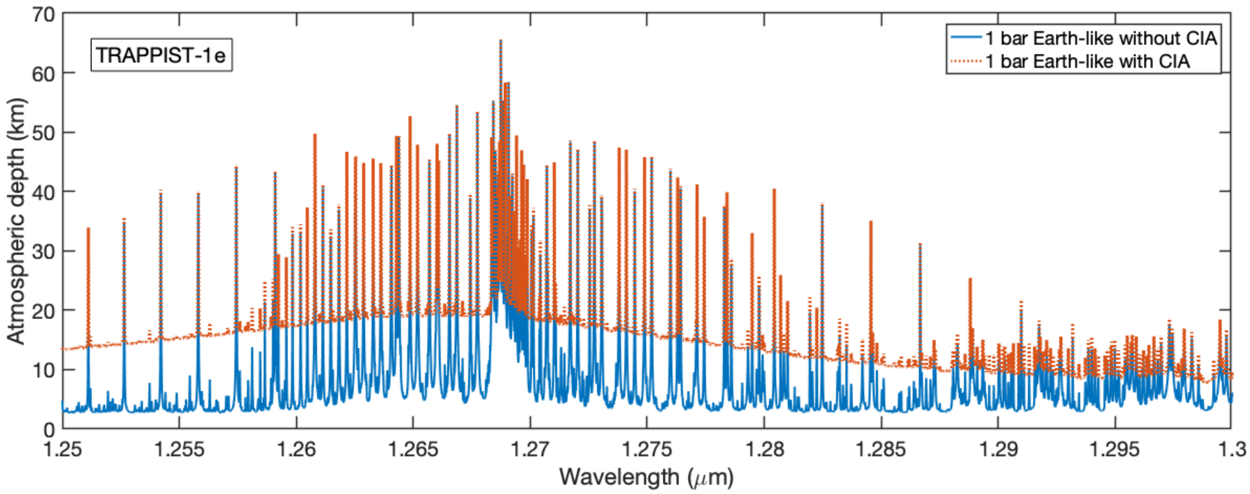

Figure 3.30: Atmospheric depths (in km) of TRAPPIST-1e with 1 bar Earth-like atmosphere with the continuum opacities (in dashed red line) and without the continuum opacities (in solid blue line) are shown here.

Rayleigh scattering) are calculated from Kofman & Villanueva (2021). The bond albedo is taken as zero in all three planets. The expected planetary signal and noise are generated using the Planetary Spectrum Generator (PSG) code (Villanueva et al. 2018). PSG uses PUMAS, or Planetary and Universal Model of Atmospheric Scattering (Villanueva et al. 2015), is a layer-by-layer radiative transfer for computing spectra of hydrostatic equilibrium atmospheres. It integrates the latest radiative-transfer methods and spectroscopic parameterizations, in order to compute high resolution spectra via line-by-line calculations (Villanueva et al. 2018). Throughout the analysis, Local Thermodynamic Equilibrium, LTE condition is assumed.

The Poisson noise is injected into all the observation spectra. The planet's transmission spectra is injected only in the transit observation frames. For simplicity, the planet's transmission spectra is injected in all the transit frames assuming a constant orbital phase, as the planet induced Doppler-shift is less than 1 km/s in all three planets.

Contamination from telluric lines were not added to the spectra, under the assumption that complete telluric features can be removed through airmass corrections (Winn et al. 2004; Jensen et al. 2012; Kawauchi et al. 2018) and through detrending algorithm like `SYSREM` (Tamuz et al. 2005; Birkby et al. 2013).

3.3.4 Cross-correlation Analysis

Each frame is divided by a median combined out-of-transit spectra to remove the stellar features and retain the transit features from the planet. This flux ratio is subtracted by 1 in order to remove spurious results in the upcoming step of cross-correlation, thereby shifting the pseudo-continuum to 0. Each transit will have N observations, where $N = N_t + N_{out}$, is the sum of number of transit observations and out-of-transit observations respectively. The flux ratio is then given by,

$$F_i(\lambda) = \frac{f_i}{\bar{f}_{out}} - 1 \tag{3.2}$$

where f_i is the normalized flux. For n^{th} transit visit, each with N observations, index i runs from i = 1, 2, 3, ..., n×N. Also $\bar{f}_{out}$ is the median-combined master out-of-transit frame until the n^{th} transit visit.

Each $F_i(\lambda)$ is then cross-correlated with an atmosphere template $F_{atm}(\lambda)$ (same atmosphere that was injected in the planet) to compute the cross-correlation function (CCF) in the velocity range of ± 200 km/s.

$$CCF_i(v) = \int_{\lambda_1}^{\lambda_2} F_i\left(\lambda - \frac{v}{c}\lambda\right) \times F_{atm}(\lambda)\ d\lambda \tag{3.3}$$

with the limits $\lambda_1 = 1.25$ μm and $\lambda_2 = 1.30$ μm. Then all the transit CCFs and the out-of-transit CCFs are separately median-combined to create the master in-transit cross-correlation function, $\overline{CCF}_t(v)$ and master out-of-transit cross-correlation function, $\overline{CCF}_{out}(v)$ respectively. They are then divided to create the CCF flux ratio, $\overline{CCF}(v)$ as shown in the equation below.

$$\overline{CCF}(v) = \frac{\overline{CCF}_t(v)}{\overline{CCF}_{out}(v)} \tag{3.4}$$

The planetary signals are searched in the vicinity (i.e., ±25 km/s) of the planet's rest velocity (v = 0 km/s). The SNR of the detection is computed from the noise in the in-transit and out-of-transit observations that were used to compute the flux ratio $F_i(\lambda)$, by comparing it with the expected planetary signals in the atmosphere template $F_{atm}(\lambda)$. We estimated the significance of detection by dividing the $\overline{CCF}(v)$ at velocity v, by its uncertainty.

We consider the atmosphere to be detected, when we reach a 5-σ detection level. An example of the CCF plots of planet TRAPPIST-1b for 1 bar Earth-like atmosphere and 1 bar desiccated O_2 atmosphere is shown in Figure 3.31.

The number of transits required for all three planets, TRAPPIST-1b, e and f to reach the above detection levels are shown in the Table 3.2 below. We restricted the maximum number of transits to 200 in all our analysis. In the case of planet TRAPPIST-1b, we can see that the desiccated O_2 atmospheres can be easily detected with less than 10 transits (see Figure 3.32) and the high surface pressure 100 bar O_2 can be detected with just 2 transits. The high surface pressure Earth-like atmospheres are difficult to be confirmed with 5-σ significance especially when we consider them with continuum processes.

In the case of habitable zone planets of TRAPPIST-1, planets 'e' and 'f', both show reasonable requests for transits of desiccated O_2 atmospheres, with the quickest detection for 100 bar O_2 case without the continuum processes (see Figures 3.33 and 3.34). In fact,

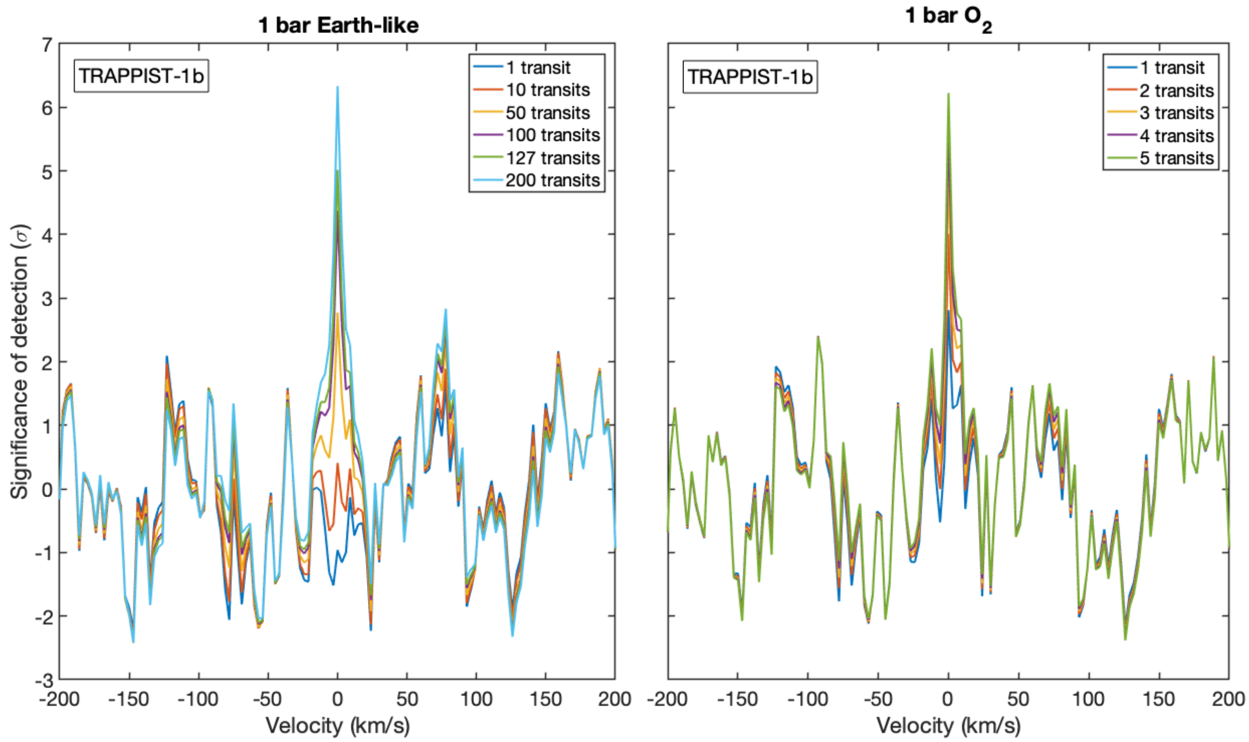

Figure 3.31: CCF plots for different number of transits of TRAPPIST-1b with 1 bar Earth-like atmosphere [left] and 1 bar desiccated O_2 [right].

the continuum processes make it difficult to detect any high pressure atmosphere as they dominate over the individual spectral lines (see Figure 3.30).

For a 1 bar Earth-like atmosphere with CIA and Rayleigh scattering in any of TRAPPIST-1b, e or f planet, the confirmation is not possible even with 200 transits. However, in the absence of continuum opacities, the detection is possible in 70 transits for TRAPPIST-1f and over 100 transits for TRAPPIST-1b and e.

However, with 2-σ significance we can rule out Earth-like atmospheres in all three planets under 50 transits. Also we can rule out the presence of desiccated O_2 atmospheres in all three planets in all pressure levels under 15-20 transits with 2-σ significance.

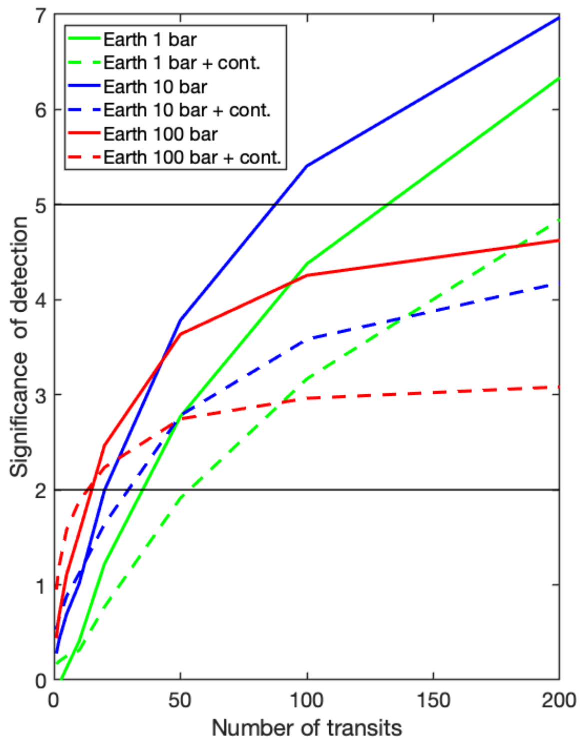

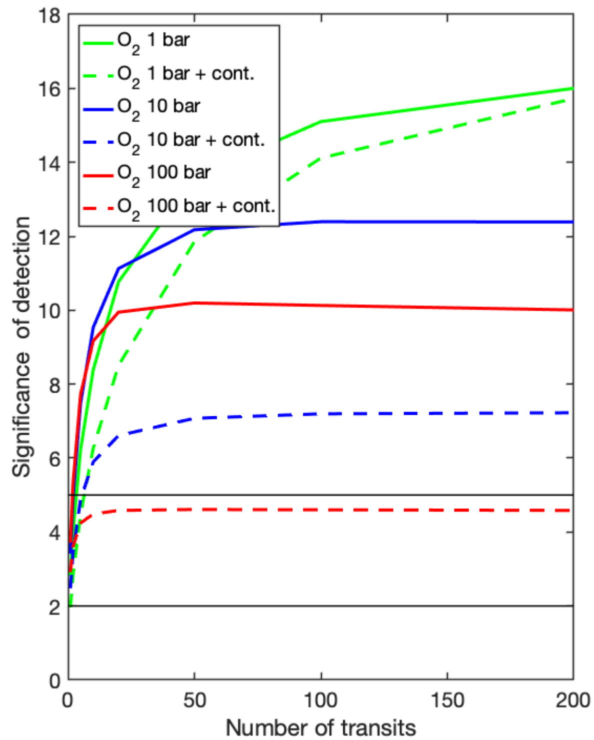

Figure 3.32: **Left**: Number of transits of TRAPPIST-1b required to reach a 5-σ detection in an Earth-like atmosphere for different pressures with continuum processes (dashed lines) and without the continuum processes (solid lines). **Right**: Similar plots for desiccated O_2 atmospheres. Black horizontal lines in both panels mark the 2-σ and 5-σ detection levels.

In a nutshell, with a limit on the available telescope time, the best science case we can make is to propose/rule out the desiccated O_2 atmospheres with high significance. For low pressure, Earth-like atmospheres in all three planets, the detection possibility is very low as the atmosphere would be within 1 scale-height of the planet. The possibilities on the origin of high pressure desiccated O_2 and Earth-like atmospheres are discussed in the Discussions chapter.

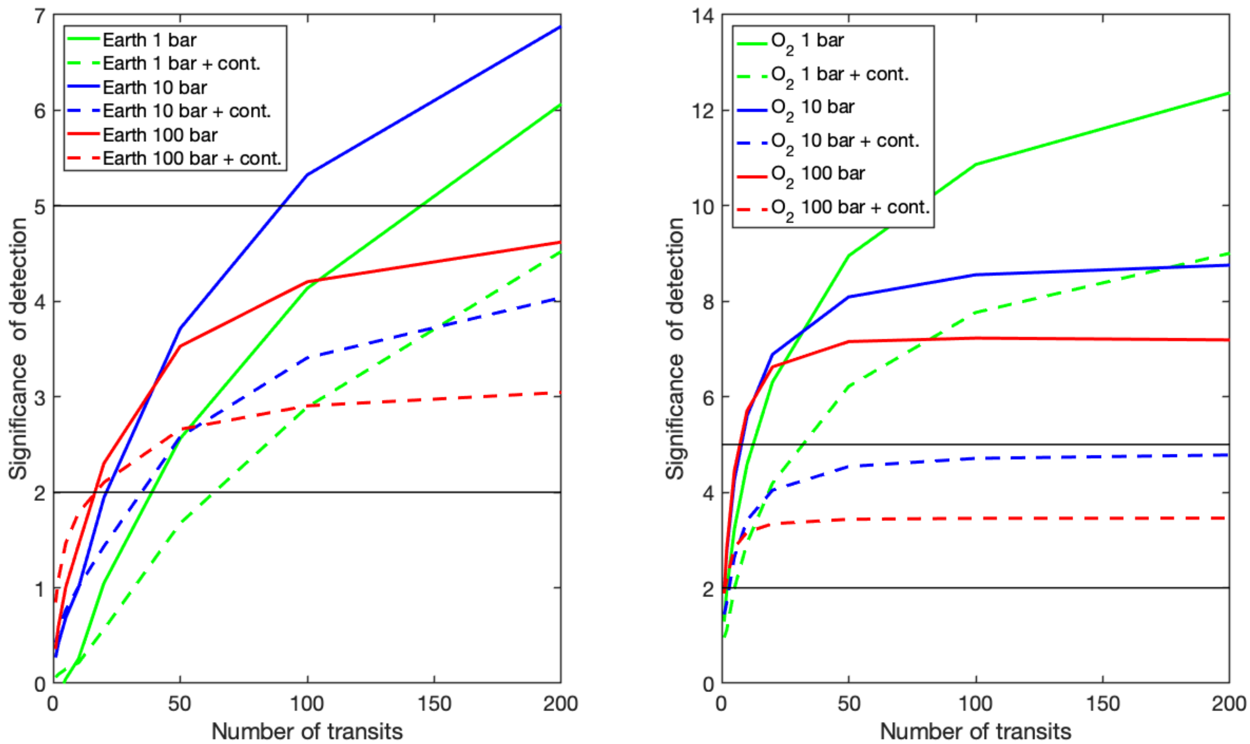

Figure 3.33: **Left**: Number of transits of TRAPPIST-1e required to reach a 5-σ detection in an Earth-like atmosphere for different pressures with continuum processes (dashed lines) and without the continuum processes (solid lines). **Right**: Similar plots for desiccated O_2 atmospheres. Black horizontal lines in both panels mark the 2-σ and 5-σ detection levels.

Table 3.2:: Number of transits to achieve 5-σ detection

Type	TRAPPIST-1b	TRAPPIST-1e	TRAPPIST-1f
Desiccated O_2 1 bar	4 (0.4031)	12 (0.624)	9 (0.7259)
Desiccated O_2 1 bar + cont.	7(0.5398)	30 (0.9971)	23 (1.1724)
Desiccated O_2 10 bar	3 (0.3544)	8 (0.5146)	6 (0.5981)
Desiccated O_2 10 bar + cont.	6 (0.5102)	>200 (2.6129)	>200 (3.5042)
Desiccated O_2 100 bar	2 (0.2953)	7 (0.4881)	5 (0.5528)
Desiccated O_2 100 bar + cont.	4 (0.4254)	>200 (2.6527)	>200 (3.5527)
Earth-like 1 bar	127 (2.2575)	139 (2.1126)	69 (2.0035)
Earth-like 1 bar + cont.	>200 (2.8395)	>200 (2.5448)	122 (2.6714)
Earth-like 10 bar	85 (1.8612)	88 (1.6977)	46 (1.6492)
Earth-like 10 bar + cont.	>200 (2.862)	>200 (2.5664)	>200 (3.449)
Earth-like 100 bar	>200 (2.8778)	>200 (2.5814)	88 (2.3002)
Earth-like 100 bar + cont.	>200 (2.8845)	>200 (2.5881)	>200 (3.4775)

Note: The number in the bracket denotes the SNR at the 5-σ detection transit. If the number of transit is > 200, the number in the bracket denotes the SNR at the 200^{th} transit.

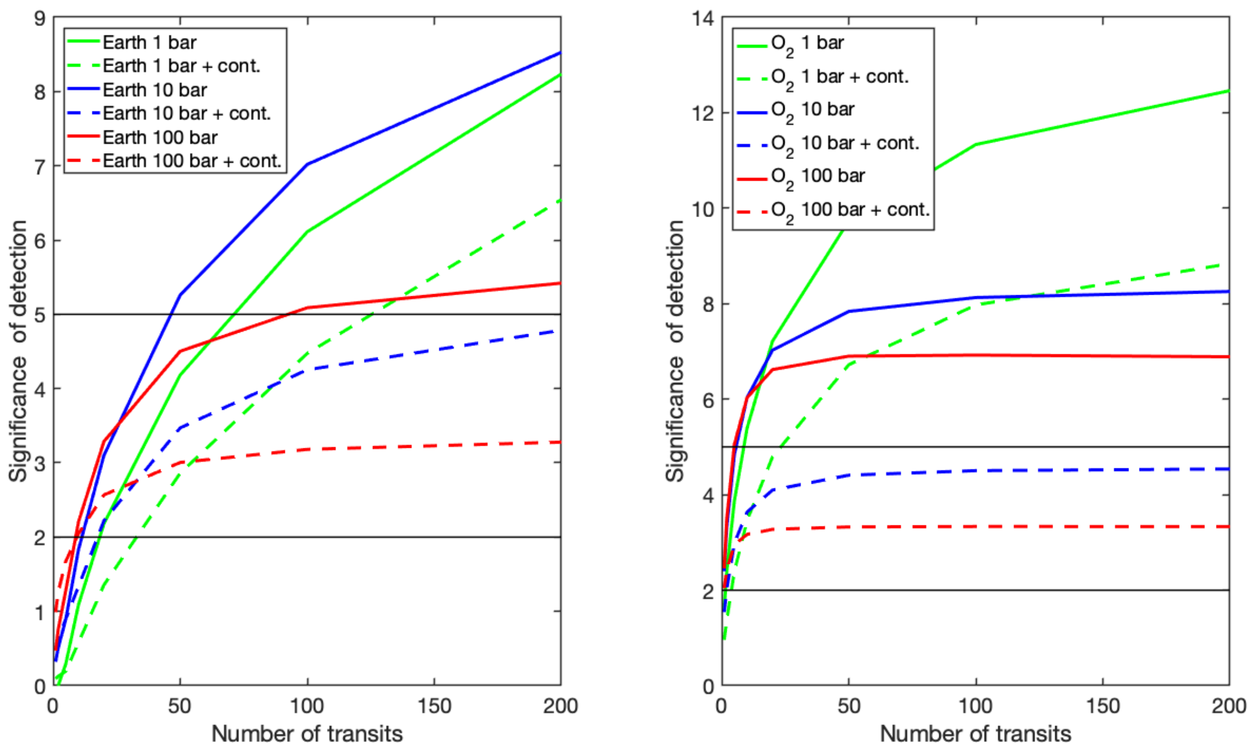

Figure 3.34: **Left**: Number of transits of TRAPPIST-1f required to reach a 5-σ detection in an Earth-like atmosphere for different pressures with continuum processes (dashed lines) and without the continuum processes (solid lines). **Right**: Similar plots for desiccated O_2 atmospheres. Black horizontal lines in both panels mark the 2-σ and 5-σ detection levels.

Chapter 4

Discussion

"With all things being equal, the simplest explanation tends to be the right one."

- William of Ockham, 14^{th} century.

4.1 Significance of He I observations

In this work we presented the observations of 8 different planets on 5 different planetary systems from 3 different telescopes and instruments. Most of our targets lie in the radius gap or Neptunian evaporation valley (Fulton et al. 2017; Owen & Wu 2013, 2017) of low-mass stars. Thanks to *Kepler*, the concept of radius gap and evaporation valley is well understood in the bright solar-mass stars. However, the evolution of planets around low-mass stars is not well understood, due to the lack of targets and well characterized planets (Hirano et al. 2018). Hence this study is motivated in bridging the knowledge gap of atmospheric evolution from solar-mass stars' planets to the low-mass stars' planets.

He I triplet at 1083 nm, the photoevaporation marker in this study is ideal for characterizing evaporative atmospheres in K-dwarfs and M-dwarfs (Oklopčić 2019). The non-detection atmospheric escape upper-limit of all K- and M-dwarf planets from our observations along with best estimate of age are presented in the Table 4.1 below.

Table 4.1:: Atmospheric escape upper-limit estimation of our targets

Planet name	Upper limit EW	Spec. type	Age (Gyr)
AU Mic b	<4.4 mÅ (IRD)	pre-main	0.022[⋆]
	<3.7 mÅ (NIRSPEC)		
TRAPPIST-1b	<7.754 mÅ (IRD)	M8	7.6±2.2[#]
	<3.467 mÅ (HPF)		
TRAPPIST-1e	<10.458 mÅ (IRD)	M8	7.6±2.2[#]
TRAPPIST-1f	<4.143 mÅ (IRD)	M8	7.6±2.2[#]
TOI-1235b	<1.42 mÅ (IRD)	M0.5	<10[+]
GJ 9827b	<13.5101 mÅ (IRD)	K5	-
GJ 9827d	<15.6374 mÅ (IRD)	K5	-

Note: All the upper-limits are at 99% confidence except TOI-1235b and TRAPPIST-1 planets, which are at 95% confidence. The age of GJ 9827 star is not known to any certainty.

Reference: [⋆] Mamajek & Bell (2014); [#] Burgasser & Mamajek (2017) [+] Bluhm et al. (2020)

The non-detection in TRAPPIST-1 planets are not surprising as these planets are very old, rocky and receives less than efficient insolation from its star for populating the metastable state of Helium atoms (see Section 4.5 for a brief discussion). The higher upper-limit EW of TRAPPIST-1e compared to its neighbor TRAPPIST-1f could arise from a variety of reasons. If this EW is due to a planetary signal, then the temporal variation of EW should show an inverted V- or U-profile peaking during the mid transit, a trademark of planetary excess absorption (eg., as seen in HIP 67522b; Figure 3.13). We do not see such a trend during the transit of TRAPPIST-1e. However, if there was a trend, it could be hidden in the noise as TRAPPIST-1 is a faint star that shows large scatter in the RV data (Hirano et al. 2020a). Another probable cause of this large EW might arise from the observing conditions on the night of TRAPPIST-1e transit. The transit began before the beginning of the observation and also when the target was at a low elevation (i.e., high airmass). This perturbed observing conditions accompanied by high winds might have caused the increase in the observed EW.

In the case of GJ 9827b and d, the stellar He I line positions were contaminated with telluric lines. Hence we had to perform `SYSREM` to remove the telluric features. This process might leave residues which show large scatter (Nugroho et al. 2021), leading to higher estimate of EW upper-limits. Also GJ 9827 was at a very low elevation when the transit of GJ 9827d began, increasing the strength of the telluric line that was contaminating the stellar He line. This sharp increase might have not have been corrected by `SYSREM` leaving behind a higher EW in the He I region.

In the case of AU Mic b, the system is very young and should be evaporating its atmosphere. However the non-detection result in AU Mic b poses an interesting question, '*What determines the possibility of detecting the He I signal in young planets?*'. There probably are several prongs to this question. Primary thought dwells to the atmosphere of the planet. Being born in a gas-poor planetary nebula, the AU Mic b might not have accreted sufficient gas before the gas disk was dispersed. And the accreted gas might have been evaporated within its first 22 Myr. Energy-limited mass-loss estimates with assumed efficiency presented in Section 4.3 shows the time for evaporation is around $\sim$270 Myr. But if the planet accreted even less gas than the assumed 0.1% of the planet's mass, then the non-detection would make sense. Essentially, the planet might be a rocky super Earth than a gaseous Neptune. One other possibility could be that the planet might have extended atmosphere, but not sufficient energy to excite the Helium atoms to metastable state to produce the 1083 nm feature. It is quite difficult to verify the presence of Helium through other markers as the stronger markers of Helium lie in ultra-short UV wavelengths (eg., 58 nm feature; Herzberg 1958). The other possibility is that the composition of the atmosphere might not be similar to the assumed solar-like composition (i.e. 90% H and 10% He). If the atmosphere is highly dominant with Hydrogen, then observing the Lyman-α feature in UV might give us some information. Section 4.9 presents the possible scenarios for such multi-band observations. Finally, another interesting possibility arises from the presence of protoplanetary disk in the AU Mic system. The dust grains could essentially block the He I feature, restricting our window of observation.

The non-detection in TOI-1235b is surprising because the planet receives sufficient insolation and orbits an early M-dwarf, one of the ideal stellar host for producing the He I feature (Oklopčić 2019). But since the age of the system is not known, it is not possible to pin-point the reason for this non-detection without having observations in other bands (eg., Lyman-α). A brief comparison of the age of the system and He I detection is shown Section 4.5.

4.2 Photoevaporation in low-mass star planets?

The upper-limit estimates are from the analysis of transmission spectra presented in Chapter 3. All the planets' upper-limit are estimated at 99% confidence, except TOI-1235b and TRAPPIST-1 planets which are estimated at 95% confidence. In the case of TOI-1235b, it is primarily due to the negative absorption during the transit of TOI-1235b, i.e., transmission spectra show negative absorption (see Figure 3.10), producing spurious upper-limits with higher confidence.

The age plays a major role in determining if the planet is currently loosing the extended atmosphere or not. In the case of Jupiter-sized planets, the evaporation might still persists even after the initial XUV dominant first few hundred Myrs for solar type stars and 1-5 Gyr for lower mass stars. But for the smaller planets around the radius gap, age might be critical (Owen & Wu 2017). As the small planets in close-in orbits around low-mass stars receive strong high energy radiation for more than 1 Gyr (Johnstone et al. 2021), the accreted primordial H/He atmosphere might completely evaporate. The non-detections seen in the above systems could be because of that as the photoevaporation would have scalped the entire atmosphere, leaving behind a rocky planet. Mention must be made here that the age of GJ 9827 system and TOI-1235 system are not accurately estimated.

These planets could also be sculpted by core-powered mass-loss process (Ginzburg et al. 2016, 2018; Gupta & Schlichting 2019, 2020). Following the dispersal of the protoplanetary disc, the heat from the cooling inner layers of the atmosphere unbinds the loosely bound outer layers, on a timescale of a few million years (Ginzburg et al. 2018). This results in shrinking of the planet's radius roughly to twice the radius of rocky core at this time (Owen & Wu 2016; Ginzburg et al. 2018). After this, if the core dominates in heat capacity, then its cooling luminosity might strip off the entire atmosphere envelope leaving behind a bare core (Ginzburg et al. 2016). More massive atmospheres, on the other hand, survive and cool without being affected by the core's luminosity. And since the massive atmospheres are unaffected and small atmospheres are completely stripped off, this process too produces the bimodal distribution final atmosphere masses and planet radii (Ginzburg et al. 2018). The core-powered mass-loss scenario has weak dependence of stellar mass (Gupta & Schlichting 2019, 2020; Cloutier & Menou 2020), making it difficult to rely on this mechanism alone as the reason behind the origin of radius gap. In general, it could be a combination of both photoevaporation and core-powered mass-loss mechanisms at play in sculpting the atmospheres.

The sub-sample of planets that lie on either side (GJ 9827b and d) and right in the middle of radius gap (TOI-1235b) were our primary targets in this study. However the lack of detection in these planets might indicate the atmospheric evolution of low-mass star's planets might be different from those of solar-type star's planets. Recent study like Cloutier & Menou (2020) on the *K2* targets reveal that the low-mass stars prefer having rocky planets in their close-orbits than non-rocky planets with volatiles. Although the radius valley structure in the occurrence rate of small close-in planets is demonstrated to persist in low-mass stars (Hirano et al. 2018), the occurrence rate of non-rocky planets with volatiles ($\sim 2\,R_\oplus$ peak of the bimodal peaks seen in Fulton et al. (2017)) decreases steadily as we move from mid-K dwarfs to mid-M dwarfs (Cloutier & Menou 2020). The non-rocky planet peak in the bimodal occurrence rates effectively vanishes around mid-M dwarfs as rocky planets increasingly dominate the close-in planet population toward later spectral types. Also the radius gap is not void of planets as shown in Cloutier &

Menou (2020). This is supported from our results of non-detection in GJ 9827b, GJ 9827d and TOI-1235b. If these planets are populating the radius gap, then it is an indication that the evolution of low-mass stars' close-in planets would be different from those of solar-type stars. Another mechanism that has been proposed to explain this pattern of planet distribution in low-mass star planets is the scenario of planets forming in gas-poor environments (Lopez & Rice 2018). Dynamical fiction in the disk delays the gas accretion with the core still embedded in protoplanetary disk. This friction continues for few million years, within which the gaseous disk has almost completely dissipated (Lee et al. 2014; Lee & Chiang 2016; Lopez & Rice 2018). This scenario might be applicable to AU Mic system as well, as the observation of its protoplanetary disk show that it has low gas-to-dust ratio (Roberge et al. 2005).

However, if the photoevaporation mechanism and core-powered mass-loss mechanism are still at play, then the partial filling of the radius gap would imply that photoevaporation or core-powered mass-loss is less efficient around lower-mass stars (Cloutier & Menou 2020). It is possible to distinguish between photoevaporation/core-powered mass-loss and planets forming in gas-poor disk by observing close-in planets around low-mass stars. There exist a region, where the predictions of these two classes of models differ, and characterizing the planets in the overlapping regions might give us the clarity in resolving this dilemma. Please see Section 4.5 for a brief discussion on the predictions of various models.

4.3 Quantitative estimates of mass-loss

The EW estimates for our planets shown in Table 4.1 give the upper-limits on the strength of planetary absorption signals. To get a physical sense of the EW estimates, we calculate the height of the atmosphere from these upper-limits. We modelled these EW into Gaussian with the same stellar line width and positions to calculate the excess absorption depth. This line depth can be translated to atmospheric altitudes using the expression, absorption signal (%) $\approx 2\mathrm{nHR}_p/\mathrm{R}_\star^2$. Here, H is the atmospheric scale-height for an atmosphere of near-solar composition (μ=2.3). And 'n' denotes the number of scale heights corresponding to the absorption signal. The resulting altitude of atmospheres are shown in Table 4.2. The extremely high values of TRAPPIST-1e, GJ 9827b and GJ 9827d are due to the poor observing conditions and telluric contamination (see Section 4.1).

Given the non-detection upper-limits from our target planets, we attempt to estimate the escape mass-loss rates for the planets. We estimate an energy-limited escape rate by combining the available X-ray and photoionizing EUV (< 912 Å) irradiances, F_{XUV} for the planets as shown in the equation presented in Watson et al. (1981) and Erkaev et al. (2007).

$$\dot{M}_{EL} = \frac{\eta\pi F_{XUV} R_{XUV}^3}{KGM_p} \tag{4.1}$$

Here, we assume a nominal efficiency of η=10% (Shematovich et al. 2014). R_{XUV} is the effective radius at the level of the atmosphere where the XUV radiation is absorbed and from which escape occurs. Here we assume it to be the planet's radius, R_p. G is the Newton's gravitational constant and K is a correction factor (taken as 1) that accounts for a finite Roche radius (Erkaev et al. 2007).

In the case of AU Mic system, the X-ray and EUV luminosities are taken from Tsikoudi & Kellett (2000). In the mass-loss calculations, we assumed the planet AU Mic b's mass to be the best estimate of 11.8 $M_\oplus$ (Hirano et al. 2020b). In the case of TRAPPIST-1 planets, the XUV and Lyα fluxes are obtained from Bourrier et al. (2017). For the GJ 9827 system, the XUV flux is obtained from Carleo et al. (2021). The XUV luminosities are not measured for TOI-1235 and HIP 67522. And since the age is not accurately estimated for TOI-1235 we used the available X-ray and EUV luminosities of a similar M0.5 type star (YY Gem A; Johnstone et al. 2021) in the place of TOI-1235b. The estimated mass-loss rates are shown in the Table 4.2 below.

Table 4.2:: Atmospheric escape mass-loss rates of our targets

Planet name	F_{XUV} (ergs s^{-1} cm^{-2})	$\dot{m}$ ($M_\oplus$/Gyr)	t_{eva} (Gyr)	atm. altitude (R_p)
AU Mic b	6367.2	0.0431	0.2735	< 0.4006
TRAPPIST-1b	1916	2.1×10^{-3}	6.5822	< 0.6082
TRAPPIST-1e	297	3.599×10^{-4}	19.2255	< 1.2070
TRAPPIST-1f	172	2.034×10^{-4}	51.0669	< 0.3706
TOI-1235b	24811.9	0.0203	3.4036	< 0.5151
GJ 9827b	37364.1	0.0295	1.6488	< 7.0033
GJ 9827d	4223.7	0.0103	3.1845	< 4.9582

In general, the above calculation are made with an assumption that the planets are born with about 1% by mass of primordial atmosphere. However, in the case of AU Mic b, the planetary disk has a low gas to dust ratio of 6:1 rather than the expected 100:1 (Roberge et al. 2005). Hence, here we assume a lower mass of primordial atmosphere, about 0.1% of planet's mass. The atmospheric evaporation time for a constant XUV flux is shown as t_{eva} in the Table 4.2. The closest TRAPPIST-1 planet would have lost its primordial atmosphere in the 6.6 Gyr of it's lifetime while TRAPPIST-1e & f might still hold on to its primordial atmosphere. However, the updated densities of these planets indicate the planets do not host any extended atmospheres (Agol et al. 2021). In the case of TOI-1235b, our model predicts the time to completely evaporate the primordial atmosphere is 3.4 Gyr. If the planet's age is accurately estimated to be older than this, then we can rule out the presence of extended atmosphere by energy-limited estimates. The same scenario holds for GJ 9827b (t_{eva} = 1.65 Gyr) and GJ 9827d (t_{eva} = 3.18 Gyr). The recent findings of Carleo et al. (2021) show that GJ 9827b GJ 9827d have a mass-loss rate of 1.9 $M_{\oplus}$/Gyr and 0.3 $M_{\oplus}$/Gyr. Both our results and results from Carleo et al. (2021) indicate that the atmosphere in both the planets might have been completely stripped off. If we assume a Earth-like atmosphere ($\sim m_{atm} = 5 \times 10^{21}$ gms) the TRAPPIST-1 planets would take less than 4.5 Myr to evaporate the atmosphere (TRAPPIST-1b takes only 0.4 Myr). And in the case of water ocean world atmosphere ($\sim m_{atm} = 1.4 \times 10^{24}$ gms), the planets would take only 1.2 Gyr to evaporate them (TRAPPIST-1b takes only 0.1 Gyr). These mass-loss rates and evaporation time should be taken with caution as planets of TRAPPIST-1 system (also GJ 9827 and TOI-1235, if their age is beyond the saturated timescale) would have received higher XUV radiation in their early years.

4.4 Evaporating atmosphere in HIP 67522b

The evaporating Helium in the atmosphere of hot Jupiter HIP 67522b is detected with an excess absorption of 7.1 ± 0.7% (altitude of 7.9644 R_p). This is the largest He I absorption seen in a G-dwarf planet and the first planet to have its He I detected with IRD instrument in the Subaru Telescope. The telluric correction was not performed on this target's transit observations as the correction might affect the red-ward wing of the He I absorption feature. Instead, we completely masked the telluric dominant region (1083.4 - 1083.7 nm) in all our analysis.

As shown in Oklopčić (2019), the spectra is considered as a 'hard' spectra if the ratio of XUV flux to mid-UV flux is higher. Such a hard stellar flux is efficient in exciting the Helium atoms to the triplet metastable state and are seen in K-dwarfs and early M-dwarfs. Although young stars are expected to be active, we did not see any signatures of flare-like activities in the temporal variation (see Figure 3.13) of HIP 67522, indicating the star has a lower XUV flux. Stars with such lower XUV flux are expected to have softer spectra for producing the Helium in metastable state. This is not a surprise, as G-dwarfs in general are expected to have softer spectra. Planets irradiated by these softer stellar spectra produces low density of free electrons to balance Helium recombination. Hence in these planetary atmospheres, the recombination is balanced by the direct photoionization of the metastable state, driven by the stellar mid-UV flux. Therefore the fraction of Helium atoms in the triplet state increases with increase in EUV flux and decreases with increasing mid-UV flux, making it marginally efficient in producing the metastable Helium feature.

While examining the He I feature of HIP-67522b, we noticed an excess absorption of

≈1.5% at 1082.8 nm (see Figure 3.16). This excess absorption raised the curiosity on its origin. From the National Institute of Standards and Technology database, NIST database (Ralchenko 2005), we looked for an atomic species that has a transition at the expected wavelength. The primary candidate was Vanadium I (V I) as the wavelength matched the expected position. There were two V I lines in the vicinity of 1082.8 nm. Both these lines arise from successive transitions. The 1082.756 nm arises from the transition of $3d^4$ 4s to $3d^4$ 4p and 1082.831 nm arises from the transition of $3d^4$ 4p to $3d^5$. There are no known OH and H_2O telluric lines in the vicinity of these vanadium lines. The Figure 4.1 shows the excess absorption seen in the IRD data (red). Using 6-parameters χ^2 analysis, we estimate the excess absorption to be 1.4 ± 0.8 % (altitude of 1.5705 R_p) and the best fit model is shown in blue in Figure 4.1.

Although TiO and VO have been detected in a few hot Jupiters (Désert et al. 2008; Evans et al. 2016), the atomic vanadium has not been detected in any exoplanet. To estimate the mass-loss rates, we need to know the XUV flux of the planet. And since in the case of the young solar analogue HIP 67522, the X-ray and EUV luminosities are not measured, we used the Rossby Number-X-ray luminosity relations for the young stars (Johnstone et al. 2021) to estimate them. The mass-loss rate estimated using Equation 4.1 for an assumed planetary mass of 1 $M_{\rm Jup}$, comes out to be 1.07×10^{13} g/s (∼56 $M_\oplus$/Gyr). Under the current assumption of energy-limited efficiency of 10%, the photoevaporation process is expected continue until 52.8 Myr of the planet (current age is 17 Myr).

Although detection of evaporating atmosphere in a G-dwarf planet is not in line with the primary focus of this study, which focuses on evolution of atmospheres in low-mass star's planets, this result is highly beneficial to the exoplanet community. This is the longest orbit planet till date for which the Helium is detected. In addition, getting more

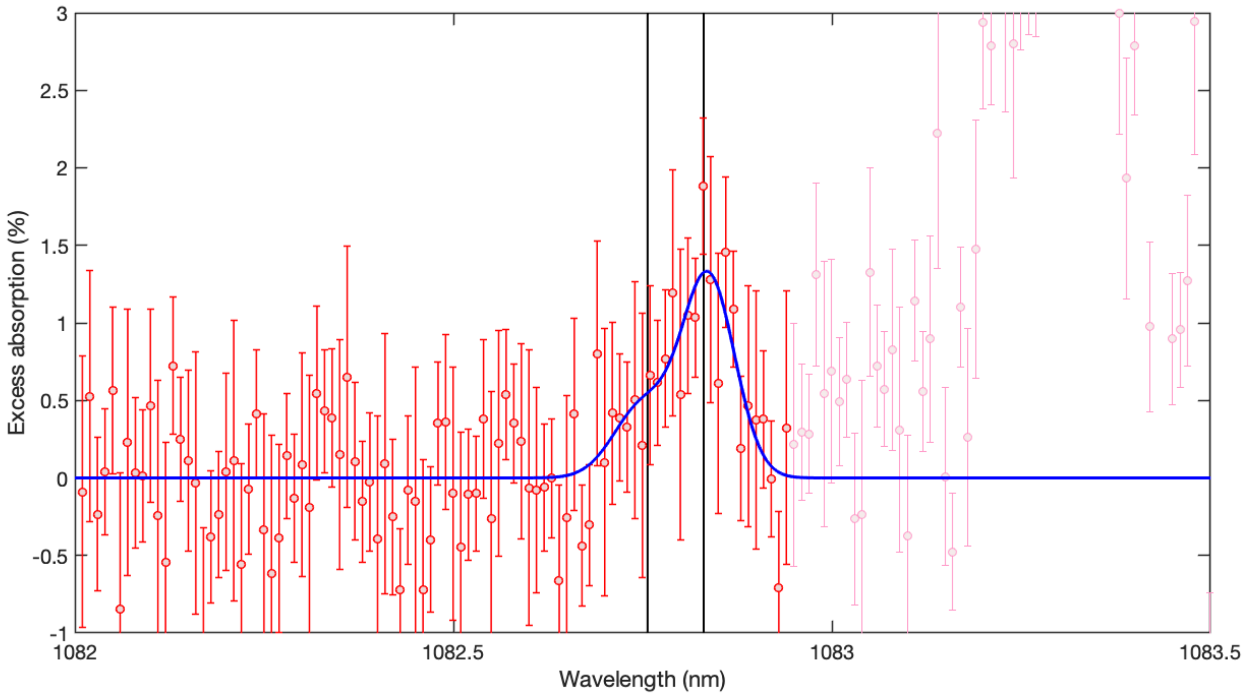

Figure 4.1: Excess absorption of V I in HIP 67522b. The best fit model (blue) estimates an excess absorption of 1.4 ± 0.8 %. The black vertical lines mark the positions of the two V I lines: 1082.756 nm and 1082.831 nm. The spectra beyond 1082.95 nm is not used in the analysis as they would be contaminated by He I absorption.

planets with evaporating atmosphere aids in getting a better constrain on the stellar dependence of evaporation.

4.5 Ideal targets for He I studies

The insolation-semi-major axis plot of all the observed targets from this study is plotted along with the previously observed targets from literature in Figure 4.2. One can clearly see the demarcation in the detected and non-detected planets' distribution in the insolation-semi-major axis plot. Planets in the top left corner receive extreme amounts of radiation from their host star that the entire primordial H/He atmosphere the planet hosted would have been lost in the first few million years, after the orbit stabilization (Owen & Wu 2013). The planets in the lower half receive low radiation such that the fraction of photoionized Hydrogen and Helium reduces, thereby reducing the available Helium in the metastable state to create this 1083 nm feature.

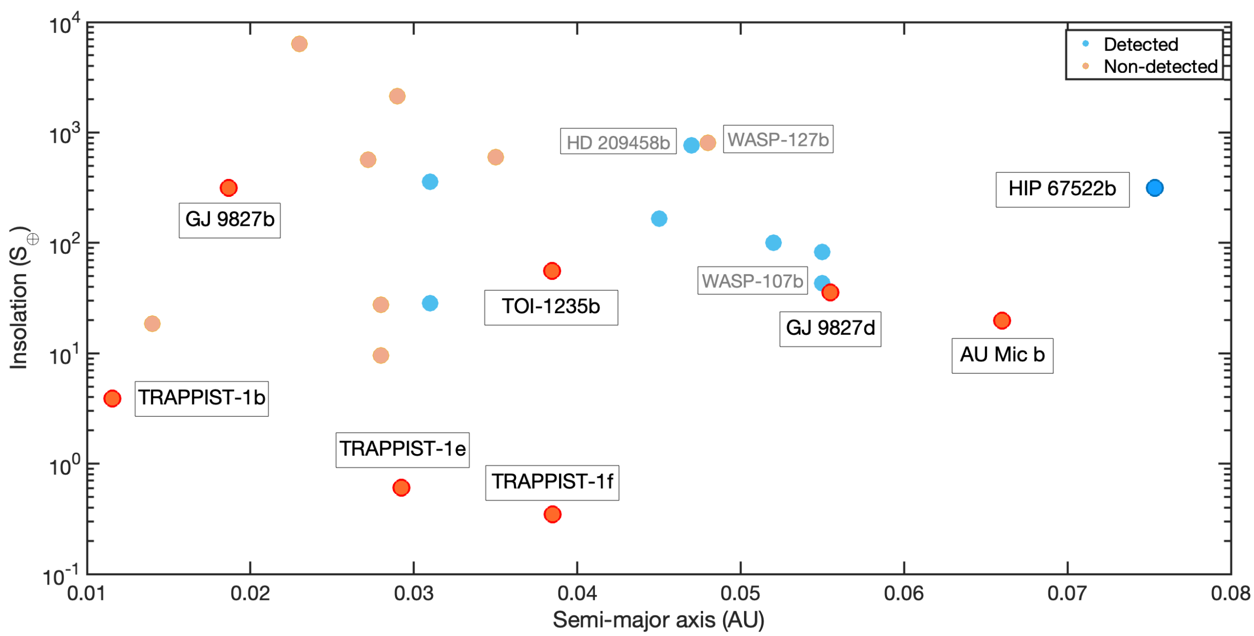

Figure 4.2: Insolation - semi-major axis plot for He I observed targets from this study along with previously observed targets from literature. The He I detected planets (blue) receive moderate insolation from their host star when compared to the non-detected planets (red).

Same explanation holds for planets that are further away from the star. There is a window that changes with the age of the star in this plot that would give us a rough idea if the planet is currently loosing its atmosphere. Of course there are numerous other factors (eg., stellar type; Oklopčić 2019) that contributes to this photoevaporation, here we focus on two such factors: age and semi-major axis. As the age increases, the detectable window moves from top left corner to middle of the insolation-semi-major axis plot. Planets beyond this observable window would not loose its primordial atmosphere, if present, through photoevaporation. There are a couple of curious cases seen from this plot. The evaporating atmosphere has been detected in WASP-107b but not in GJ 9827d, although they receive almost identical stellar flux. Since the age of both these systems are not accurately estimated, it is impossible to distinguish the reason behind the non-detection. Young systems are the ideal candidates for characterizing the evaporative atmospheres. However, the number of transiting young systems are very rare (Tofflemire et al. 2020) as well as the host stars exhibit numerous flares on their surface, making it impractical to estimate the mass through RV measurements. However, we can overcome this impracticality in multi-planet system using the TTV measurements for the mass estimation. The stellar mass (equivalent to spectral type) - insolation plot (Figure 4.3) clearly shows that the He I detected planets are around K-dwarfs and G-dwarfs ($0.5\,\mathrm{M}_\odot < M_\star < 1.5\,\mathrm{M}_\odot$), supporting the predictions of Oklopčić (2019). The He I detected planet between AU Mic b and GJ 9827d is GJ 3470b, a Neptune-sized planet orbiting a moderately active early M-dwarf. On the lower stellar mass side of AU Mic b is GJ 436b, another Neptune-sized planet orbiting an inactive red dwarf for which the He I in extended atmosphere is not detected. Active stars have stronger XUV luminosity compared to the inactive stars, thereby increasing the population of Helium in the metastable state (Oklopčić 2019). In the case of GJ 436b, the Ly-α exosphere was detected (Kulow et al. 2014; Ehrenreich et al. 2015), but its old age (7.4 Gyr; Saffe et al. 2005) and low XUV flux make it difficult to excite the He I triplet atoms.

In the case of K2-25b, although this mid M-dwarf system is young (in Hyades cluster, 650 Myr; Mann et al. 2016), the planet does not receive sufficient insolation. The planet needs to be much more closer than the current orbit to receive sufficient energy to excite the Helium atoms. Also no Ly-α absorption was detected to confirm any excess atmosphere (Rockcliffe & Newton 2019). GJ 1214b orbiting another mid M-dwarf is probably an old system ($\sim$ 3 Gyr, slow rotator Berta et al. 2011). Although the orbit is closer than GJ 436b to its host star, it is not close-enough to excite the Helium atoms to metastable state.

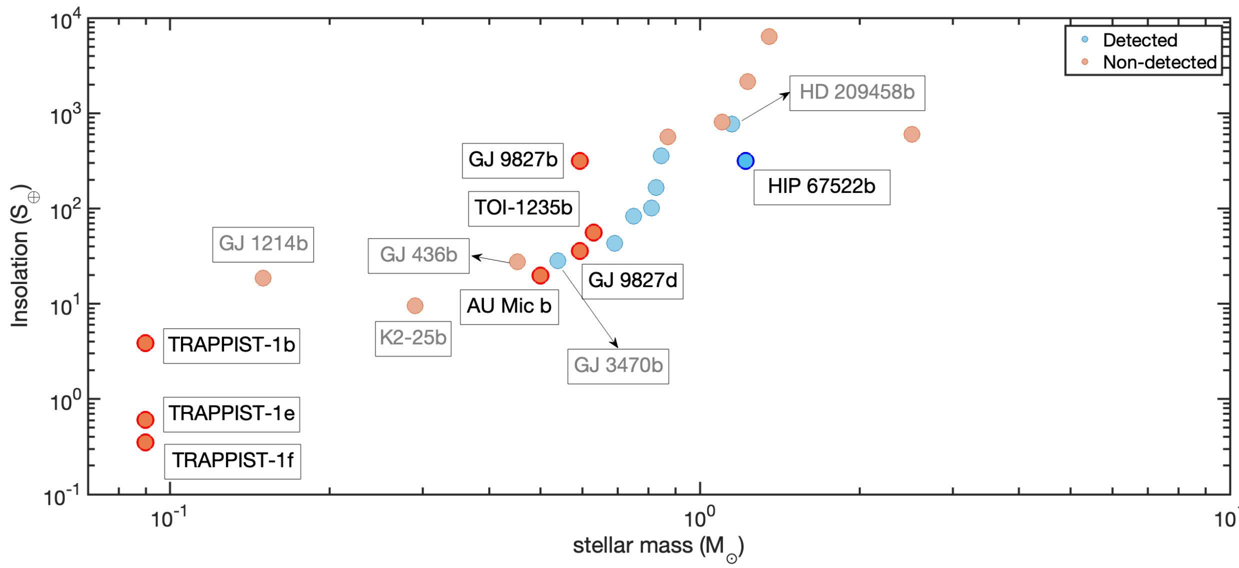

Figure 4.3: Insolation - stellar mass plot for He I observed targets from this study along with previously observed targets from literature. The He I detected planets are marked as blue and non-detected planets as red.

Another aspect of gaining more insight is by looking at the insolation-radius plot. Three different models predict different variations for transition of rocky to non-rocky planets (i.e. the location of radius gap) in low-mass star planets. The photoevaporation models predict the slope of radius gap varies with insolation as $r_{p,gap} \propto S_\oplus^{0.11}$ (Lopez & Rice 2018) while the core-powered mass-loss models predict the slope to be $r_{p,gap} \propto S_\oplus^{0.10}$ (Gupta & Schlichting 2019). The second class of models, i.e., the gas-poor formation models predict the slope of radius gap varies with insolation as $r_{p,gap} \propto S_{\oplus}^{-0.06}$ (Cloutier & Menou 2020).

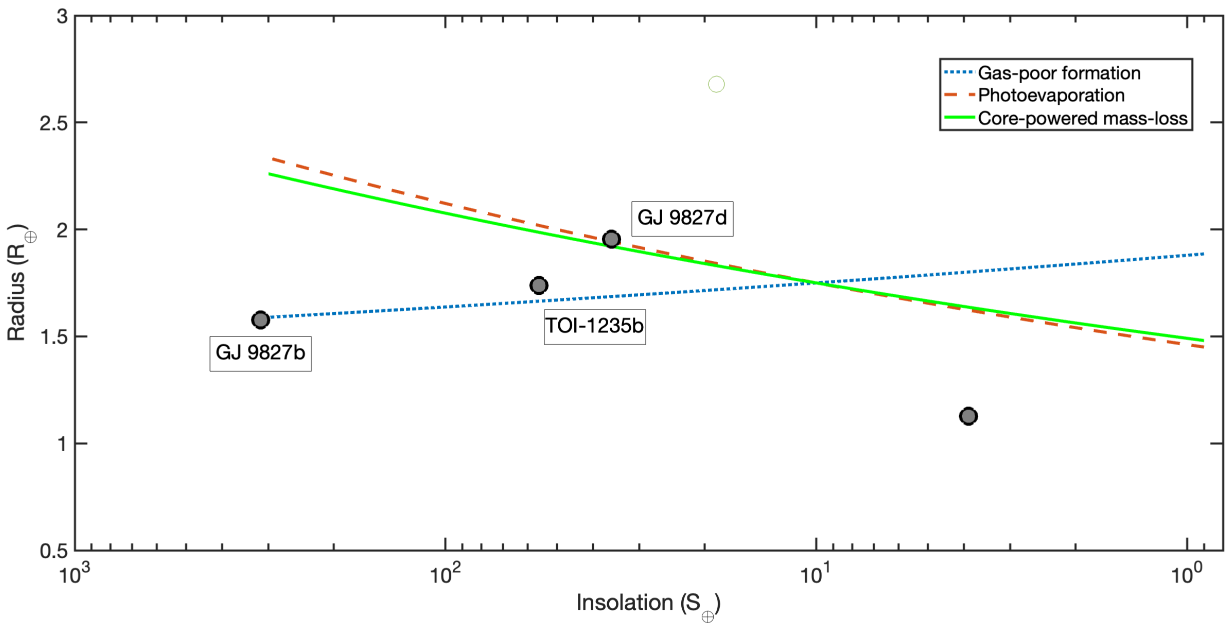

Figure 4.4: Insolation - radius plot with selected targets from this study along with various model prediction on the rocky - non-rocky transition.

Gas-poor formation models have a different slope than the photoevaporation/core-powered mass-loss models. This creates a region in the insolation-radius plot where the two classes of models predict the planets to have opposite characteristics (see Figure 4.4). The planet TOI-1235b lie exactly in the middle of this region, where photoevaporation/core-powered mass-loss models predict the planet should be rocky and gas-poor formation models predict the planet to be non-rocky. From the He I non-detection in this study and bulk properties from the literature (Cloutier et al. 2020; Bluhm et al. 2020), the planet TOI-1235b tends to be envelope-free rocky planet and supporting the scenario of photoevaporation and/or core-powered mass-loss. However, the planets GJ 9827b and GJ 9827d are barely in the gap, making it difficult to pin-point the model. Either way, to confirm the validity of these models, more planets in this sub-space need to be identified and characterized.

4.6 Stellar Helium line

The stellar He I feature is not detected in the low temperature star, TRAPPIST-1. The absence of stellar line is likely due to the low effective temperature of TRAPPIST-1 and not due to a line fill-in from collisional excitation (Fuhrmeister et al. 2019). To confirm this hypothesis, we computed the pseudo-equivalent width (pEW) of stellar Helium line at 1083 nm of 30+ targets from IRD-Subaru Strategic Program (SSP) (PI: Bun'ei Sato; Sato & IRD-SSP Team 2019). The targets of IRD-SSP program consist of late-M dwarf stars (spectral type later than M4). We used 37 stars from their sample and computed the pEW of the stellar Helium line. Since these are low temperature stars, there is a possibility of molecular lines occupying the same location. Hence we chose a 1Å wide region (1083.277 - 1083.377 nm) centered at the doublet of the He I triplet lines to compute the pEW. The temperature of the stars are computed from the broadband photometric magnitudes from GAIA DR2 (Gaia Collaboration et al. 2016) and using the BT-settl models (Allard 2014). The computed pEWs are plotted in Figure 4.5.

The temperature of TRAPPIST-1 is uniquely very low that none of the SSP targets are in the same temperature space as TRAPPIST-1 (see Figure 4.5). A 1-D fit to the data shows that the expected pEW for TRAPPIST-1 is very low around 8.5 ± 8 mÅ, indicating the stellar Helium line is not present due to its low temperature and confirming our hypothesis.

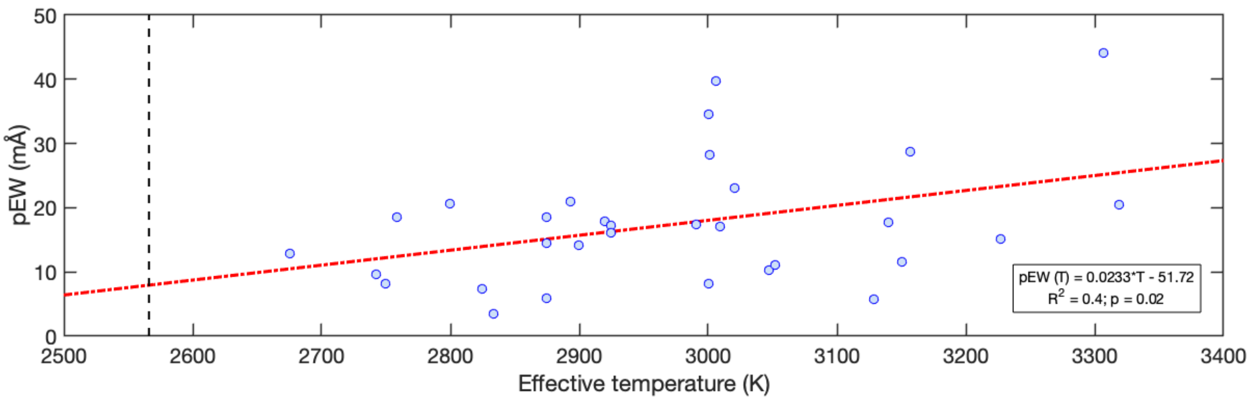

Figure 4.5: The stellar He I pEW variation of IRD-SSP samples (Sato & IRD-SSP Team 2019). Best fit 1-D model is shown in red and vertical black dashed line marks the effective temperature of TRAPPIST-1.

The Hydrogen Paschen-beta (Pa-β) line is created by the transition of electron from second excited state (n = 3) to fourth excited state (n = 5) (Wiese & Fuhr 2009) and occurs at the wavelength 1282.2 nm. Seen in emission in T-Tauri stars, it is a known tracer for accretion of material onto the central stars (Whelan et al. 2004). However, in our observations, we detected the Pa-β line in absorption. Also there exist a negative correlation between Pa-β and He I absorption as seen in the TRAPPIST-1 observations (see Figure 3.9). However the physical significance of this correlation is not well understood.

4.7 NIR O_2 observations

The NIR O_2 feature at 1.27 μm was analysed for TRAPPIST-1b, e and f planets. No detectable signals are seen in the CCF plots of planets TRAPPIST-1b and TRAPPIST-1e near the planet's rest velocity. In the case of TRAPPIST-1f, there is a local maximum feature at -4 km/s in the CCF plot (refer Figure 3.25). This could be an artifact introduced by the detrending algorithm `SYSREM` (Yan et al. 2020). As `SYSREM` does not differentiate the telluric spectra with the stellar/planetary spectra, it is difficult to pin-point the source of this feature. This SNR ~ 2 feature could also originate from an evaporating desiccated O_2 atmosphere (Luger & Barnes 2015).

Terrestrial planets in the habitable zone of M dwarfs older than 1 Gyr could have been in a runaway greenhouses for several hundred million years following their formation due to the star's extended pre-main sequence phase, provided they form with abundant surface water (Kopparapu et al. 2014, 2017). Such extended runaway greenhouses can lead to atmospheric evolution divergent from that of Earth. Due to the prolonged pre-main sequence phase of M-dwarfs, the HZs to move inward up to an order of magnitude in semimajor axis over the course of first few hundred million years (Luger & Barnes 2015). So the planets currently in the HZ of the star, like TRAPPIST-1f, were not in the HZs when they formed. If these planets formed with water, they may have experienced extended runaway greenhouses for about $\sim$1 Gyr. During a runaway greenhouse, photolysis of water vapor in the stratosphere followed by the hydrodynamic escape of the upper atmosphere can lead to the rapid loss of a planet's surface water. Because hydrogen escapes preferentially over oxygen, large quantities of O_2 also build up, up to several hundreds to thousands of bar of O_2 (Luger & Barnes 2015). And if the sinks for removing O_2 (like XUV driven hydrodynamic escape) are not strong, then the O_2 can stay for several Gyr as the loss through diffusion is extremely low.

Given the old age of TRAPPIST-1 system, TRAPPIST-1f, which is currently in the outer edge of the HZ could have been outside the HZ in the initial few hundred million years and if it acquired water in those forming years, it might still be holding on to several hundreds and thousands of bar of O_2 .

To check if such a detection is possible with Subaru class telescope, we ran a mock transmission spectra using the Planetary Spectrum Generator (Villanueva et al. 2018). We followed the same procedure as described in the Section 3.3. For this study, we used a spectrograph with a resolution of 70,000; similar to that of IRD. We assumed a nominal throughput of 3% for the 8.2m telescope. We injected the transit spectra with 1 bar, 10 bar, 100 bar and 1000 bar of O_2 and try to retrieve it back through cross-correlation analysis. Figure 4.6 shows the significance of detection for different desiccated O_2 surface pressures.

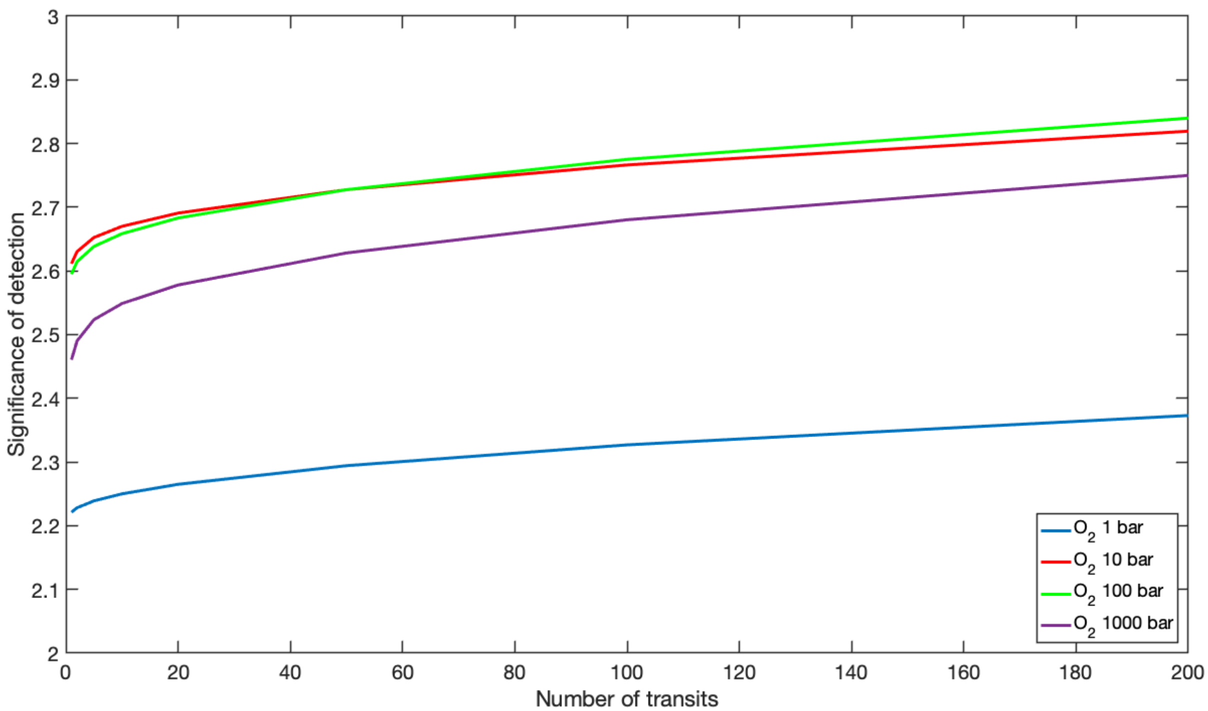

Figure 4.6: Number of transits of TRAPPIST-1f needed to detect desiccated O_2 atmospheres from a 8.2m telescope for different pressures.

The significance of detection did not reach the 5-σ level, even with 200 transits for all the cases. However, even with a single transit, we are able to achieve a 2-σ marginal detection.

This simulation along with the CCF analysis of actual IRD specrta does not provide evidence for O_2 detected in the atmosphere of TRAPPIST-1f, but just a hint of possibility of O_2 atmosphere, urging the exoplanet community to observe more transits of TRAPPIST-1f, possibly from different instruments to reciprocate the results.

4.8 Significance of O_2 feasibility study

The feasibility study for detecting lower atmospheres of TRAPPIST-1b, e and f from a 30 meter class telescope and a spectrograph with resolution of 100,000 was shown in Section 3.3. The analysis was under the assumption that the throughput of the next-generation telescopes would reach at 10%. This study would give the astronomers a clear pathway to choose the planets and detection criteria for their observations. The SNR achieved at the 5-σ detection level were similar to the results presented by Snellen et al. (2013). From this feasibility study, it can be seen that the best atmospheres that can be detected with reasonable number of transits is desiccated O_2 atmospheres. The collision-induced absorption of O_2 - O_2 near 1.27 μm dominate over the individual molecular O_2 line, making the atmosphere detectable with high-significance. Under the assumption that limited telescope time would be available for exoplanetary science, and even more limited time for a single system, the maximum science we can extract would be the detection/absence of desiccated O_2 atmospheres with high significance and ruling out Earth-like atmospheres of all pressure levels with low significance.

4.9 Observations in other wavelength bands

Observing evaporative mechanism in different wavelength bands is limited by the expected species of the primordial atmosphere (Seager & Sasselov 2000). Hydrogen being the most common (about 70-90% by mass) is the primary species of interest. Its Lyman-α line in UV is the most prominent marker (Seager & Sasselov 2000; Vidal-Madjar et al. 2003). Because of the abundance of hydrogen and the strength of the Lyα line, Lyα exospheres can absorb a very large fraction of starlight during transit (Zhang et al. 2021). In the Neptune-sized planet GJ 436b, for example, Lyα line has a transit depth of 56% in blue wing and 47% in the red wing (Lavie et al. 2017b). The Lyα core is wiped out by the interstellar medium (ISM) absorption, hence the wings of this broad line is studied.

Next most abundant species is Helium, occupying the remaining mass fraction. The next important marker is Helium in NIR, the explanation of which is extensively shown in Section 1.3.1. This metastable Helium line is not absorbed by the ISM and probes low-velocity Helium in the denser part of the exosphere, closer to the planet's surface ($\sim$3 planetary radii). These two observations complement each other as the Lyα line probes the high-velocity less dense part of the upper exosphere, about 10-12 planetary radii from the surface. Probing our targets in Lyα might yield similar result of non-detection for TOI-1235b, GJ 9827b and d as the mass measurements confirms that the planets do not have extended exospheres. The recent *HST* Lyα observations of GJ 9827b (Carleo et al. 2021) showed no extended atmosphere present in the planet, supporting our results. Transit of TRAPPIST-1 planets have been observed in Lyα and yielded marginal decrease in stellar flux. But the signal could not be confirmed as of planetary origin (Bourrier et al. 2017). In the case of HIP 67522b, we would expect a huge absorption in the Lyα wings as the system is very young and is currently loosing its atmosphere.

In the observations of secondary lower atmospheres ($\sim$ 1 scale-height from planet's surface), there are several bands of H_2O in NIR that can be used (Aronson & Waldén 2015). Strong bands of carbon bearing molecular species like CH_4, CO_2 can be observed in mid-infrared (MIR) from space-based telescopes (Quanz et al. 2018, 2019; Fujii & Matsuo 2021). The upcoming James-Webb Space Telescope (JWST; Beichman et al. 2014) has the mid-IR instrument (MIRI; Wright et al. 2004) that has been proposed to probe the lower atmospheres, targeting the carbon-bearing species along with oxygen and water (Fauchez et al. 2020).

Chapter 5

Conclusion

In this study, we presented observations of eight different planets in five different systems with three different telescopes. The primary focus is on the atmospheric evolution of close-in planets around low-mass stars. The presence of radius gap is not well understood, especially in low-mass star planets. Our low-mass stars' target planets lie in and around the radius gap, providing an excellent opportunity to test the photoevaporation models. We detected evaporating helium exosphere from a very young hot Jupiter HIP 67522b around a G-dwarf. We also analysed the Near Infra-Red (NIR) molecular oxygen O_2 feature at 1.27 μm in the TRAPPIST-1 planets (b, e and f). This wavelength window gives an unique opportunity to probe the upper tropospheric and stratospheric layers of their lower atmospheres. We also added a feasibility study on the detection of this NIR O_2 feature in the atmospheres of the same TRAPPIST-1 planets from a future 30m class telescope with a NIR spectrograph with resolution R = 100,000. The main take away points from our study is given below:

- The transit observations of AU Mic b, GJ 9827b, GJ 9827d, TOI-1235b, TRAPPIST-1b, TRAPPIST-1e and TRAPPIST-1f yielded no detection of helium at the 1083 nm He I triplet. The planets GJ 9827b and GJ 9827d are on either side of the radius gap (Fulton et al. 2017); with GJ 9827d expected to have rocky cores with volatiles (Owen & Wu 2017). And TOI-1235b with radius $\approx 1.75\ R_{\oplus}$ puts it right in the middle of radius gap. The non-detection from these three planets questions the role of photoevaporation in the evolution of close-in small planets around low-mass stars. Other scenarios like planets forming in a gas-poor environment might be dominant in low-mass star planets as they predict continuous distribution rocky planets, with planets filling in the radius gap. The non-detection of evaporating helium in other low insolated planets (see Figure 4.2) indicate the necessity of high energy to drive the atmosphere, thereby justifying our understanding of atmospheric evolution. Our observations would add essential and critical data to the weakly populated dataset of small close-in planets around low-mass stars.

- The absence of stellar helium line in TRAPPIST-1 star is consistent with our expectations of low EW for such an ultra-cool small star (see Figure 4.5) and not due to a line fill-in from collisional excitation (Fuhrmeister et al. 2019).

- We detected the escaping helium in the young hot Jupiter HIP-67522. We estimated an excess absorption of 7.1±0.7% He I triplet from our transit observations. We also detect, ground state Vanadium (V I) in the atmosphere of HIP 67522b, making it the first exoplanet to have it's atmosphere detected with Vanadium. We estimate an excess absorption of 1.4±0.8%.

- We analysed the transit observations of TRAPPIST-1 planets (b, e and f) in the wavelength regime of NIR O_2 at 1.27 μm. After correcting for the telluric lines using airmass-correction (Winn et al. 2004; Jensen et al. 2012; Kawauchi et al. 2018) and with a de-trending algorithm like `SYSREM` (Tamuz et al. 2005), we performed a cross-correlation analysis to search for any planetary signals. We couldn't detect any planetary O_2 from this analysis. However, the marginal-detection in TRAPPIST-1f at v = -4 km/s with SNR $\sim$ 2 in the planet rest frame could not be ruled out as an artifact as we could reproduce the feature from mock-transmission spectrum simulation (with PSG; Villanueva et al. 2018). However, we insist that more observations are needed to confirm this detection.

- We also made a feasibility study on the detection of this NIR O_2 at 1.27 μm in the TRAPPIST-1 planets (b, e and f) from a 30m class telescope with a resolution of 100,000. Although we simulated several types of atmospheres, the cost-effective and feasible detection would be for a desiccated O_2 atmosphere without any continuum processes in all three TRAPPIST-1 planets (b, e and f) for pressures as high as 100 bar.

The observations were part of the following programs/papers published :

- Subaru program: S20A-UH104 (PI: Eric Gaidos)
- Subaru program: S20B-069 (PI: Vigneshwaran Krishnamurthy)
- Subaru program: S21A-100 (PI: Vigneshwaran Krishnamurthy)
- Subaru program: S21A-129 (PI: Teruyuki Hirano)
- Subaru program: IRD-SSP (PI: Bun'ei Sato)
- Article: Krishnamurthy et al. 2021

- Article: Hirano et al. (2020a)
- Article: Hirano et al. (2020b)

References

Agol, E., Dorn, C., Grimm, S. L., et al. 2021, The Planetary Science Journal, 2, 1

Alibert, Y., Mordasini, C., Benz, W., & Winisdoerffer, C. 2005, A&A, 434, 343

Allard, F. 2014, in Exploring the Formation and Evolution of Planetary Systems, ed. M. Booth, B. C. Matthews, & J. R. Graham, Vol. 299, 271–272

Allart, R., Bourrier, V., Lovis, C., et al. 2018, Science, 362, 1384

—. 2019, A&A, 623, A58

Alonso-Floriano, F. J., Snellen, I. A. G., Czesla, S., et al. 2019, A&A, 629, A110

Andretta, V., Giampapa, M. S., Covino, E., Reiners, A., & Beeck, B. 2017, ApJ, 839, 97

Andretta, V., & Jones, H. P. 1997, ApJ, 489, 375

Aronson, E., & Waldén, P. 2015, A&A, 578, A133

Barclay, T., Pepper, J., & Quintana, E. V. 2018, ApJS, 239, 2

Barstow, J. K., & Irwin, P. G. J. 2016, MNRAS, 461, L92

Batalha, N. E., Lewis, N. K., Line, M. R., Valenti, J., & Stevenson, K. 2018, ApJ, 856, L34

Batalha, N. M., Rowe, J. F., Bryson, S. T., et al. 2013, ApJS, 204, 24

Beichman, C., Benneke, B., Knutson, H., et al. 2014, PASP, 126, 1134

Belu, A. R., Selsis, F., Morales, J. C., et al. 2011, A&A, 525, A83

Berta, Z. K., Charbonneau, D., Bean, J., et al. 2011, ApJ, 736, 12

Bétrémieux, Y., & Kaltenegger, L. 2014, ApJ, 791, 7

Birkby, J. L., de Kok, R. J., Brogi, M., et al. 2013, MNRAS, 436, L35

Bluhm, P., Luque, R., Espinoza, N., et al. 2020, A&A, 639, A132

Borucki, W. J., Koch, D., Basri, G., et al. 2010, Science, 327, 977

Bourrier, V., Lecavelier des Etangs, A., Dupuy, H., et al. 2013, A&A, 551, A63

Bourrier, V., Ehrenreich, D., Wheatley, P. J., et al. 2017, A&A, 599, L3

Bourrier, V., Lecavelier des Etangs, A., Ehrenreich, D., et al. 2018, A&A, 620, A147

Breckinridge, J. B., & Hall, D. N. B. 1973, Sol. Phys., 28, 15

Brogi, M., Line, M., Bean, J., Désert, J. M., & Schwarz, H. 2017, ApJ, 839, L2

Burgasser, A. J., & Mamajek, E. E. 2017, ApJ, 845, 110

Burke, C. J., Bryson, S. T., Mullally, F., et al. 2014, ApJS, 210, 19

Campbell, B., Walker, G. A. H., & Yang, S. 1988, ApJ, 331, 902

Carleo, I., Youngblood, A., Redfield, S., et al. 2021, AJ, 161, 136

Catling, D., & Kasting, J. F. 2007, Planets and life: the emerging science of astrobiology, 91

Charbonneau, D., Brown, T. M., Noyes, R. W., & Gilliland, R. L. 2002, ApJ, 568, 377

Chen, H., & Rogers, L. A. 2016, ApJ, 831, 180

Ciardi, D. R., Fabrycky, D. C., Ford, E. B., et al. 2013, ApJ, 763, 41

Cloutier, R., & Menou, K. 2020, AJ, 159, 211

Cloutier, R., Rodriguez, J. E., Irwin, J., et al. 2020, AJ, 160, 22

Crossfield, I. J. M., Barman, T., Hansen, B., & Frewen, S. 2019, Research Notes of the American Astronomical Society, 3, 24

Cuzzi, J. N., Hogan, R. C., Paque, J. M., & Dobrovolskis, A. R. 2001, ApJ, 546, 496

de Wit, J., Wakeford, H. R., Gillon, M., et al. 2016, Nature, 537, 69

de Wit, J., Wakeford, H. R., Lewis, N. K., et al. 2018, Nature Astronomy, 2, 214

de Zeeuw, P. T., Hoogerwerf, R., de Bruijne, J. H. J., Brown, A. G. A., & Blaauw, A. 1999, AJ, 117, 354

Delrez, L., Gillon, M., Triaud, A. H. M. J., et al. 2018, MNRAS, 475, 3577

Désert, J. M., Vidal-Madjar, A., Lecavelier Des Etangs, A., et al. 2008, A&A, 492, 585

dos Santos, L. A., Ehrenreich, D., Bourrier, V., et al. 2019, A&A, 629, A47

—. 2020, A&A, 640, A29

Drake, G. W. 1971, Phys. Rev. A, 3, 908

Dressing, C. D., & Charbonneau, D. 2013, ApJ, 767, 95

—. 2015, ApJ, 807, 45

Ducrot, E., Gillon, M., Delrez, L., et al. 2020, A&A, 640, A112

Ehrenreich, D., Bourrier, V., Wheatley, P. J., et al. 2015, Nature, 522, 459

Erkaev, N. V., Kulikov, Y. N., Lammer, H., et al. 2007, A&A, 472, 329

Erkaev, N. V., Lammer, H., Odert, P., et al. 2016, MNRAS, 460, 1300

Evans, T. M., Sing, D. K., Wakeford, H. R., et al. 2016, ApJ, 822, L4

Fauchez, T. J., Villanueva, G. L., Schwieterman, E. W., et al. 2020, Nature Astronomy, 4, 372

Fuhrmeister, B., Czesla, S., Hildebrandt, L., et al. 2019, A&A, 632, A24

Fujii, Y., & Matsuo, T. 2021, AJ, 161, 180

Fulton, B. J., & Petigura, E. A. 2018, AJ, 156, 264

Fulton, B. J., Petigura, E. A., Howard, A. W., et al. 2017, AJ, 154, 109

Gaia Collaboration. 2018, VizieR Online Data Catalog, I/345

Gaia Collaboration, Prusti, T., de Bruijne, J. H. J., et al. 2016, A&A, 595, A1

Gaidos, E., Hirano, T., Mann, A. W., et al. 2020a, MNRAS, 495, 650

Gaidos, E., Hirano, T., Wilson, D. J., et al. 2020b, MNRAS, 498, L119

Gillon, M. 2018, Nature Astronomy, 2, 344

Gillon, M., Jehin, E., Lederer, S. M., et al. 2016, Nature, 533, 221

Gillon, M., Triaud, A. H. M. J., Demory, B.-O., et al. 2017, Nature, 542, 456

Gilmozzi, R., & Spyromilio, J. 2007, The Messenger, 127, 11

Ginzburg, S., Schlichting, H. E., & Sari, R. 2016, ApJ, 825, 29

—. 2018, MNRAS, 476, 759

Gordon, I. E., Rothman, L. S., Hill, C., et al. 2017, J. Quant. Spec. Radiat. Transf., 203, 3

Grady, C. A., Wisniewski, J. P., Schneider, G., et al. 2020, ApJ, 889, L21

Greenblatt, G. D., Orlando, J. J., Burkholder, J. B., & Ravishankara, A. R. 1990, J. Geophys. Res., 95, 18,577

Grimm, S. L., Demory, B.-O., Gillon, M., et al. 2018, A&A, 613, A68

Guilluy, G., Andretta, V., Borsa, F., et al. 2020, A&A, 639, A49

Gupta, A., & Schlichting, H. E. 2019, MNRAS, 487, 24

—. 2020, MNRAS, 493, 792

Hadden, S., & Lithwick, Y. 2014, ApJ, 787, 80

Hadden, S., & Lithwick, Y. 2017, in American Astronomical Society Meeting Abstracts, Vol. 229, American Astronomical Society Meeting Abstracts #229, 401.03

Hermans, C., Vandaele, A. C., Carleer, M., et al. 1999, Environmental Science and Pollution Research, 6, 151

Herzberg, G. 1958, Proceedings of the Royal Society of London Series A, 248, 309

Hirano, T., Dai, F., Gandolfi, D., et al. 2018, AJ, 155, 127

Hirano, T., Gaidos, E., Winn, J. N., et al. 2020a, ApJ, 890, L27

Hirano, T., Krishnamurthy, V., Gaidos, E., et al. 2020b, ApJ, 899, L13

Hirano, T., Kuzuhara, M., Kotani, T., et al. 2020c, PASJ, 72, 93

Hojjatpanah, S., Figueira, P., Santos, N. C., et al. 2019, A&A, 629, A80

Hori, Y., & Ogihara, M. 2020, ApJ, 889, 77

Howard, A. W., Marcy, G. W., Bryson, S. T., et al. 2012, ApJS, 201, 15

Ida, S., & Lin, D. N. C. 2004a, ApJ, 604, 388

—. 2004b, ApJ, 616, 567

Jackson, A. P., Davis, T. A., & Wheatley, P. J. 2012, MNRAS, 422, 2024

Jacob, W. S. 1855, MNRAS, 15, 228

Jensen, A. G., Redfield, S., Endl, M., et al. 2012, ApJ, 751, 86

Jin, S., & Mordasini, C. 2018, ApJ, 853, 163

Jin, S., Mordasini, C., Parmentier, V., et al. 2014, ApJ, 795, 65

Johnstone, C. P., Bartel, M., & Güdel, M. 2021, A&A, 649, A96

Jones, A., Noll, S., Kausch, W., Szyszka, C., & Kimeswenger, S. 2013, A&A, 560, A91

Kasper, M., Beuzit, J.-L., Verinaud, C., et al. 2010, in Society of Photo-Optical Instrumentation Engineers (SPIE) Conference Series, Vol. 7735, Ground-based and Airborne Instrumentation for Astronomy III, ed. I. S. McLean, S. K. Ramsay, & H. Takami, 77352E

Kawahara, H., Matsuo, T., Takami, M., et al. 2012, ApJ, 758, 13

Kawauchi, K., Narita, N., Sato, B., et al. 2018, PASJ, 70, 84

Kharchenko, N. V., Scholz, R. D., Piskunov, A. E., Röser, S., & Schilbach, E. 2007, Astronomische Nachrichten, 328, 889

Kirk, J., Alam, M. K., López-Morales, M., & Zeng, L. 2020, AJ, 159, 115

Kite, E. S., & Barnett, M. N. 2020, Proceedings of the National Academy of Science, 117, 18264

Kite, E. S., Fegley, Bruce, J., Schaefer, L., & Ford, E. B. 2019, ApJ, 887, L33

Kofman, V., & Villanueva, G. L. 2021, Journal of Quantitative Spectroscopy and Radiative Transfer, 107708

Kopparapu, R. K., Ramirez, R. M., SchottelKotte, J., et al. 2014, ApJ, 787, L29

Kopparapu, R. k., Wolf, E. T., Arney, G., et al. 2017, ApJ, 845, 5

Kopparapu, R. K., Ramirez, R., Kasting, J. F., et al. 2013, ApJ, 765, 131

Kosiarek, M. R., Berardo, D. A., Crossfield, I. J. M., et al. 2021, AJ, 161, 47

Kotani, T., Tamura, M., Suto, H., et al. 2014, in Society of Photo-Optical Instrumentation Engineers (SPIE) Conference Series, Vol. 9147, Ground-based and Airborne Instrumentation for Astronomy V, ed. S. K. Ramsay, I. S. McLean, & H. Takami, 914714

Kral, Q., Davoult, J., & Charnay, B. 2020, Nature Astronomy, 4, 769

Kreidberg, L., & Oklopčić, A. 2018, Research Notes of the American Astronomical Society, 2, 44

Kulow, J. R., France, K., Linsky, J., & Loyd, R. O. P. 2014, ApJ, 786, 132

Kurokawa, H., & Nakamoto, T. 2014, ApJ, 783, 54

Kwon, S., Hong, S., & Weinberg, J. 2004, New Astronomy, 10, 91

Lavie, B., Ehrenreich, D., Bourrier, V., et al. 2017a, A&A, 605, L7

—. 2017b, A&A, 605, L7

Lecavelier Des Etangs, A., Ehrenreich, D., Vidal-Madjar, A., et al. 2010, A&A, 514, A72

Lee, E. J., & Chiang, E. 2016, ApJ, 817, 90

Lee, E. J., Chiang, E., & Ormel, C. W. 2014, ApJ, 797, 95

Leinert, C., Bowyer, S., Haikala, L. K., et al. 1998, A&AS, 127, 1

Lépine, S., Hilton, E. J., Mann, A. W., et al. 2013, AJ, 145, 102

Lin, D. N. C., & Papaloizou, J. 1986, ApJ, 309, 846

Lockwood, A. C., Johnson, J. A., Bender, C. F., et al. 2014, ApJ, 783, L29

Loose, M., Farris, M. C., Garnett, J. D., Hall, D. N. B., & Kozlowski, L. J. 2003, in Society of Photo-Optical Instrumentation Engineers (SPIE) Conference Series, Vol. 4850, IR Space Telescopes and Instruments, ed. J. C. Mather, 867–879

Lopez, E. D., & Fortney, J. J. 2013, ApJ, 776, 2

Lopez, E. D., Fortney, J. J., & Miller, N. 2012, ApJ, 761, 59

Lopez, E. D., & Rice, K. 2018, MNRAS, 479, 5303

Lopez-Morales, M., Currie, T., Teske, J., et al. 2019, BAAS, 51, 162

Luger, R., & Barnes, R. 2015, Astrobiology, 15, 119

Luger, R., Sestovic, M., Kruse, E., et al. 2017, Nature Astronomy, 1, 0129

Lustig-Yaeger, J., Meadows, V. S., & Lincowski, A. P. 2019, AJ, 158, 27

Mahadevan, S., Ramsey, L., Bender, C., et al. 2012, in Society of Photo-Optical Instrumentation Engineers (SPIE) Conference Series, Vol. 8446, Ground-based and Airborne Instrumentation for Astronomy IV, ed. I. S. McLean, S. K. Ramsay, & H. Takami, 84461S

Mahadevan, S., Ramsey, L. W., Terrien, R., et al. 2014, in Society of Photo-Optical Instrumentation Engineers (SPIE) Conference Series, Vol. 9147, Ground-based and Airborne Instrumentation for Astronomy V, ed. S. K. Ramsay, I. S. McLean, & H. Takami, 91471G

Mamajek, E. E., & Bell, C. P. M. 2014, MNRAS, 445, 2169

Mann, A. W., Gaidos, E., Mace, G. N., et al. 2016, ApJ, 818, 46

Mann, A. W., Dupuy, T., Kraus, A. L., et al. 2019, ApJ, 871, 63

Mansfield, M., Bean, J. L., Oklopčić, A., et al. 2018, ApJ, 868, L34

Marcy, G. W., Isaacson, H., Howard, A. W., et al. 2014, ApJS, 210, 20

Maté, B., Lugez, C. L., Solodov, A. M., Fraser, G. T., & Lafferty, W. J. 2000, J. Geophys. Res., 105, 22,225

Matsakos, T., & Königl, A. 2016, ApJ, 820, L8

Mauas, P. J. D., Andretta, V., Falchi, A., et al. 2005, ApJ, 619, 604

Mawet, D., Fitzgerald, M., Konopacky, Q., et al. 2019, in Bulletin of the American Astronomical Society, Vol. 51, 134

Mayor, M., & Queloz, D. 1995, Nature, 378, 355

McLean, I. S., Becklin, E. E., Bendiksen, O., et al. 1998, in Society of Photo-Optical Instrumentation Engineers (SPIE) Conference Series, Vol. 3354, Infrared Astronomical Instrumentation, ed. A. M. Fowler, 566–578

Meadows, V. S., Reinhard, C. T., Arney, G. N., et al. 2018a, Astrobiology, 18, 630

Meadows, V. S., Arney, G. N., Schwieterman, E. W., et al. 2018b, Astrobiology, 18, 133

Misra, A., Meadows, V., & Crisp, D. 2014, ApJ, 792, 61

Morton, T. D., Bryson, S. T., Coughlin, J. L., et al. 2016, ApJ, 822, 86

Moulton, F. R. 1899, AJ, 20, 33

Moutou, C., Coustenis, A., Schneider, J., Queloz, D., & Mayor, M. 2003, A&A, 405, 341

Nikolov, N., Sing, D. K., Pont, F., et al. 2014, MNRAS, 437, 46

Ninan, J. P., Stefansson, G., Mahadevan, S., et al. 2020, ApJ, 894, 97

Niraula, P., Redfield, S., Dai, F., et al. 2017, AJ, 154, 266

Noll, S., Kausch, W., Barden, M., et al. 2012, A&A, 543, A92

Nortmann, L., Pallé, E., Salz, M., et al. 2018, Science, 362, 1388

Nugroho, S. K., Kawahara, H., Gibson, N. P., et al. 2021, ApJ, 910, L9

Oklopčić, A. 2019, ApJ, 881, 133

Oklopčić, A., & Hirata, C. M. 2018, ApJ, 855, L11

Okuzumi, S., Tanaka, H., Kobayashi, H., & Wada, K. 2012, ApJ, 752, 106

Oliva, E., & Origlia, L. 2008, in Society of Photo-Optical Instrumentation Engineers (SPIE) Conference Series, Vol. 7014, Ground-based and Airborne Instrumentation for Astronomy II, ed. I. S. McLean & M. M. Casali, 70141O

Owen, J. E., & Jackson, A. P. 2012, MNRAS, 425, 2931

Owen, J. E., & Lai, D. 2018, MNRAS, 479, 5012

Owen, J. E., & Wu, Y. 2013, ApJ, 775, 105

—. 2016, ApJ, 817, 107

—. 2017, ApJ, 847, 29

Palle, E., Nortmann, L., Casasayas-Barris, N., et al. 2020, A&A, 638, A61

Paragas, K., Vissapragada, S., Knutson, H. A., et al. 2021, ApJ, 909, L10

Plavchan, P., Werner, M. W., Chen, C. H., et al. 2009, ApJ, 698, 1068

Plavchan, P., Barclay, T., Gagné, J., et al. 2020, Nature, 582, 497

Quanz, S. P., Kammerer, J., Defrère, D., et al. 2018, in Society of Photo-Optical Instrumentation Engineers (SPIE) Conference Series, Vol. 10701, Optical and Infrared Interferometry and Imaging VI, ed. M. J. Creech-Eakman, P. G. Tuthill, & A. Mérand, 107011I

Quanz, S. P., Absil, O., Angerhausen, D., et al. 2019, arXiv e-prints, arXiv:1908.01316

Ralchenko, Y. 2005, Memorie della Societa Astronomica Italiana Supplementi, 8, 96

Rice, K., Malavolta, L., Mayo, A., et al. 2019, MNRAS, 484, 3731

Ricker, G. R., Winn, J. N., Vanderspek, R., et al. 2014, in Society of Photo-Optical Instrumentation Engineers (SPIE) Conference Series, Vol. 9143, Space Telescopes and Instrumentation 2014: Optical, Infrared, and Millimeter Wave, ed. J. Oschmann, Jacobus M., M. Clampin, G. G. Fazio, & H. A. MacEwen, 914320

Rizzuto, A. C., Newton, E. R., Mann, A. W., et al. 2020, AJ, 160, 33

Roberge, A., Weinberger, A. J., Redfield, S., & Feldman, P. D. 2005, ApJ, 626, L105

Robinson, T. D., & Catling, D. C. 2014, Nature Geoscience, 7, 12

Rockcliffe, K., & Newton, E. 2019, in AAS/Division for Extreme Solar Systems Abstracts, Vol. 51, AAS/Division for Extreme Solar Systems Abstracts, 327.16

Rodler, F., & López-Morales, M. 2014, ApJ, 781, 54

Rodriguez, J. E., Vanderburg, A., Eastman, J. D., et al. 2018, AJ, 155, 72

Rogers, L. A., & Seager, S. 2010, ApJ, 712, 974

Rothman, L. S., Gordon, I. E., Babikov, Y., et al. 2013, J. Quant. Spec. Radiat. Transf., 130, 4

Saffe, C., Gómez, M., & Chavero, C. 2005, A&A, 443, 609

Salz, M., Czesla, S., Schneider, P. C., et al. 2018, A&A, 620, A97

Sanders, G. H. 2013, Journal of Astrophysics and Astronomy, 34, 81

Sato, B., & IRD-SSP Team, . 2019, IRD SSP

Schneider, A. C., Shkolnik, E. L., Allers, K. N., et al. 2019, AJ, 157, 234

Seager, S., & Sasselov, D. D. 2000, ApJ, 537, 916

Shematovich, V. I., Ionov, D. E., & Lammer, H. 2014, A&A, 571, A94

Sing, D. K., Fortney, J. J., Nikolov, N., et al. 2016, Nature, 529, 59

Skidmore, W., TMT International Science Development Teams, & Science Advisory Committee, T. 2015, Research in Astronomy and Astrophysics, 15, 1945

Smith, G. H. 2016, Publications of the Astronomical Society of Australia, 33

Snellen, I. A. G., de Kok, R. J., de Mooij, E. J. W., & Albrecht, S. 2010, Nature, 465, 1049

Snellen, I. A. G., de Kok, R. J., le Poole, R., Brogi, M., & Birkby, J. 2013, ApJ, 764, 182

Spake, J. J., Sing, D. K., Evans, T. M., et al. 2018, Nature, 557, 68

Sperauskas, J., Bartašiūtė, S., Boyle, R. P., et al. 2016, A&A, 596, A116

Stefansson, G. K. 2019, in AAS/Division for Extreme Solar Systems Abstracts, Vol. 51, AAS/Division for Extreme Solar Systems Abstracts, 202.05

Strubbe, L. E., & Chiang, E. I. 2006, ApJ, 648, 652

Sullivan, P. W., Winn, J. N., Berta-Thompson, Z. K., et al. 2015, ApJ, 809, 77

Tamai, R., & Spyromilio, J. 2014, in Society of Photo-Optical Instrumentation Engineers (SPIE) Conference Series, Vol. 9145, Ground-based and Airborne Telescopes V, ed. L. M. Stepp, R. Gilmozzi, & H. J. Hall, 91451E

Tamura, M., Suto, H., Nishikawa, J., et al. 2012, in Society of Photo-Optical Instrumentation Engineers (SPIE) Conference Series, Vol. 8446, Ground-based and Airborne Instrumentation for Astronomy IV, ed. I. S. McLean, S. K. Ramsay, & H. Takami, 84461T

Tamuz, O., Mazeh, T., & Zucker, S. 2005, MNRAS, 356, 1466

Thalman, R., & Volkamer, R. 2013, Physical Chemistry Chemical Physics (Incorporating Faraday Transactions), 15, 15371

Thompson, S. E., Coughlin, J. L., Hoffman, K., et al. 2018, ApJS, 235, 38

Tody, D. 1993, in Astronomical Society of the Pacific Conference Series, Vol. 52, Astronomical Data Analysis Software and Systems II, ed. R. J. Hanisch, R. J. V. Brissenden, & J. Barnes, 173

Tofflemire, B., Newton, E., Mann, A., et al. 2020, in American Astronomical Society Meeting Abstracts, Vol. 235, American Astronomical Society Meeting Abstracts #235, 174.18

Tsikoudi, V., & Kellett, B. J. 2000, MNRAS, 319, 1147

Van Grootel, V., Fernandes, C. S., Gillon, M., et al. 2018, ApJ, 853, 30

Vida, K., Kővári, Z., Pál, A., Oláh, K., & Kriskovics, L. 2017, ApJ, 841, 124

Vidal-Madjar, A., Lecavelier des Etangs, A., Désert, J. M., et al. 2003, Nature, 422, 143

Villanueva, G. L., Smith, M. D., Protopapa, S., Faggi, S., & Mandell, A. M. 2018, J. Quant. Spec. Radiat. Transf., 217, 86

Villanueva, G. L., Mumma, M. J., Novak, R. E., et al. 2015, Science, 348, 218

Vissapragada, S., Knutson, H. A., Jovanovic, N., et al. 2020, AJ, 159, 278

Wakeford, H. R., Lewis, N. K., Fowler, J., et al. 2019, AJ, 157, 11

Walker, G. A. H., Walker, A. R., Irwin, A. W., et al. 1995, Icarus, 116, 359

Watson, A. J., Donahue, T. M., & Walker, J. C. G. 1981, Icarus, 48, 150

Weidenschilling, S. J. 1977a, MNRAS, 180, 57

—. 1977b, Ap&SS, 51, 153

Weidenschilling, S. J., & Cuzzi, J. N. 1993, in Protostars and Planets III, ed. E. H. Levy & J. I. Lunine, 1031

Weiss, L. M., & Marcy, G. W. 2014, ApJ, 783, L6

Wheatley, P. J., Louden, T., Bourrier, V., Ehrenreich, D., & Gillon, M. 2017, MNRAS, 465, L74

Whelan, E. T., Ray, T. P., & Davis, C. J. 2004, A&A, 417, 247

White, R. J., Schaefer, G., Ten Brummelaar, T., et al. 2015, in American Astronomical Society Meeting Abstracts, Vol. 225, American Astronomical Society Meeting Abstracts #225, 348.12

Wiese, W. L., & Fuhr, J. R. 2009, Journal of Physical and Chemical Reference Data, 38, 565

Winn, J. N., Suto, Y., Turner, E. L., et al. 2004, PASJ, 56, 655

Wolszczan, A., & Frail, D. A. 1992, Nature, 355, 145

Wright, G. S., Rieke, G. H., Colina, L., et al. 2004, in Society of Photo-Optical Instrumentation Engineers (SPIE) Conference Series, Vol. 5487, Optical, Infrared, and Millimeter Space Telescopes, ed. J. C. Mather, 653–663

Wu, Y., & Lithwick, Y. 2013, ApJ, 772, 74

Yan, F., Casasayas-Barris, N., Molaverdikhani, K., et al. 2019, A&A, 632, A69

Yan, F., Pallé, E., Reiners, A., et al. 2020, A&A, 640, L5

Yan, F., Wyttenbach, A., Casasayas-Barris, N., et al. 2021, A&A, 645, A22

Zhang, M., Knutson, H. A., Wang, L., et al. 2021, arXiv e-prints, arXiv:2106.05273

Zhang, Y., Snellen, I. A. G., Mollière, P., et al. 2020, A&A, 641, A161